Development of Biodegradable Microfluidic Networks for Tissue Engineering

by

Kevin R. King

B.S. Electrical Engineering
University of Illinois Urbana Champaign, 1999

Submitted to the Department of Electrical Engineering and Computer Science in partial fulfillment of the requirements for the degree of

Master of Science in Electrical Engineering

MASSACHUSETTS INSTITUTE OF TECHNOLOGY

September 2002

Author_____
Department of Electrical Engineering and Computer Science
September 1, 2002

Certified by_____
Joel Voldman
Assistant Professor, Electrical Engineering

Certified by_____
Jeffrey T. Borenstein
Principal Member of Technical Staff, Draper Laboratory

Certified by_____
Joseph P. Vacanti
John Homans Professor of Surgery, Harvard Medical School

Accepted by_____
Arthur Smith
Chairman, Department Committee on Graduate Students

[This page intentionally left blank]

Development of Biodegradable Microfluidic Networks for Tissue Engineering

by

Kevin Robert King

Submitted to the Department of Electrical Engineering and Computer Science on September 1, 2002 in partial fulfillment of the requirements for the degree of Master of Science in Electrical Engineering

ABSTRACT

Biodegradable tissue engineering scaffolds currently suffer from poorly controlled geometries, lack of reproducibility, and severe mass transport limitations. Microfabrication is an ideal tool for attacking problems in tissue engineering due to its control of diverse size scales, from microns to centimeters, all with micron resolution and submicron precision. By enabling precision geometries and flexible designs, microfabrication has the potential to offer creative solutions to some of the major problems facing the field of tissue engineering; those of achieving rapid vascularization and recapitulating normal complex tissue microarchitecture.

In this thesis, silicon micromachining, soft lithography, and traditional polymer processing are combined to develop a fully biodegradable microfabrication platform using poly(DL-lactic-co-glycolic) acid (PLGA 85:15). First, micron scale structures fabricated on silicon substrates are transferred into the surface of biodegradable films using polymer melt replica molding. Next, microchannel networks are sealed and made three-dimensional by stacking and irreversibly bonding the biodegradable films using a newly developed thermal fusion bonding process. The process is modeled and optimized to guide bonding of a wide range of microchannels while avoiding parasitic microstructure deformation. An extruded inlet/outlet scheme is implemented and combined with micromolding and fusion bonding to build fully patent, leak-free biodegradable microfluidic networks with predictable fluidic resistances. Finally, this thesis concludes with the first demonstration of long-term continuous-flow cell culture in prototype microfluidic networks, demonstrating the feasibility of using the newly developed biodegradable microdevices as cell-seeded tissue engineering scaffolds.

In comparison to conventional scaffold fabrication techniques, these processes offer two orders of magnitude improvement in fabrication time and spatial resolution while offering flexible designs and unmatched reproducibility. Through these features, they have enabled construction of the first fully biodegradable microfluidic networks.

Thesis Supervisor: Joel Voldman Ph.D.
Title: Assistant Professor of Electrical Engineering

Thesis Supervisor: Jeffery T. Borenstein Ph.D.
Title: Principle Member of Technical Staff, Draper Laboratory

Thesis Supervisor: Joseph P. Vacanti M.D.
Title: John Homans Professor of Surgery, Harvard Medical School

[This page intentionally left blank]

Acknowledgements

This thesis was performed as part of a long collaboration between Dr. Vacanti at MGH and Dr. Jeff Borenstein at Draper Laboratory in the general area of "microfabrication approaches to tissue engineering". Because the work was performed at both locations, I have had the benefit of interacting with many people with diverse backgrounds, experiences, and perspectives.

As I sat in the first Vacanti Lab group meeting two years ago, I vividly recall his referring to the microfabrication tissue engineering effort and saying, "As a surgeon whose focus is the patient, *my goal is clear.*" Referring to the therapeutic objective of the research, these four words will remain with me as a constant reminder of why biomedical engineering research is important. I would like to thank Dr. Vacanti for initially taking me into his lab despite my lack of prior cell culture experience and for seeing to it that I was surrounded by helpful and enthusiastic investigators in a dynamic research environment. His vision and commitment to the end goal of helping patients is not only inspiring, but also provided constant motivation for this work.

I initially joined Jeff and the MEMS group at Draper Laboratory to contribute to the microfabrication and device development side of the project, however it quickly became my research "home." Jeff has provided endless support – technical, administrative, and personal – throughout the course of my research. Quick to help in any way possible, he made sure there were no obstacles to this exploration. I appreciate his confidence and trust as well as the flexibility he gave me to shape and define the direction of this work. I have had the chance to explore a wide range of topics from the theoretical to the experimental and from the basic science to the applied. By giving me the space to mold the project and make my own mistakes, he made the successes that much more rewarding.

This thesis would not have been possible without the help of Joanne Wang, an outstanding MIT undergraduate who helped with nearly every aspect of the project. Joanne's curiosity was infectious and I'm extremely grateful for her endless commitment to the project. She offered a critical sounding board for ideas and provided a companionship that made the journey an enjoyable one.

Thank you to Joel for reviewing this thesis and helping me put together the written document. In just a few helpful discussions he was able to give me the necessary guidance to assemble my work into an organized and coherent thesis. I wish him the best of luck in his new position as a professor at MIT.

I'd like to thank the Whitaker Foundation and Draper Laboratory for their financial support through graduate fellowships; the many people at Draper Laboratory, MGH and MIT who provided helpful discussions, technical assistance, and/or friendship over the course of the past two years; and finally my family and friends for all of their support.

This thesis was prepared at The Charles Stark Draper Laboratory, Inc. under No. DAMDIT-99-2-9001. Publication of this thesis does not constitute approval by Draper or the sponsoring agency of the findings or conclusions contained herein. It is published for the exchange and stimulation of ideas. This project was sponsored by the Department of the Army, Cooperative Agreement DAMD-99-2-9001. The content of this thesis does not necessarily reflect the position or the policy of the government and no official endorsement should be inferred.

Contents

List of Figures

List of Tables

[This page intentionally left blank]

Chapter 1

Introduction

This thesis describes the development of a biodegradable polymer microfabrication platform for large-scale tissue engineering. In contrast to conventional biodegradable scaffold fabrication techniques, microtechnology is used to improve spatial resolution by two orders of magnitude while offering exceptional design flexibility and unmatched reproducibility. A new biodegradable polymer bonding technique is introduced, and a predictive model is developed and tested to enable rapid optimization of the bonding process. This powerful platform is then used to build the first ever fully biodegradable microfluidic devices. The dimensional control and design flexibility afforded by microfabrication are leveraged to construct microfluidic networks fashioned after the massively parallel highly branched microvasculature of a large organ. Then the same design is used to demonstrate the first long-term sterile cell culture in microfluidic devices of any kind, an achievement that has broad applications in the areas of tissue engineering, lab-on-a-chip devices, and biomedical microdevices in general.

Chapter 1 begins with a brief introduction to the field of tissue engineering and biodegradable polymers followed by a description of the high level goal of this thesis – to develop a biodegradable scaffold fabrication platform that will enable engineering of large vital organs. This is followed by background on conventional biodegradable polymer scaffold fabrication and it's shortcomings, as well as an introduction to the relevant areas of microtechnology. Finally, the chapter concludes with a detailed overview of this thesis.

1.1 Biodegradable Polymer Tissue Engineering

1.1.1 Tissue Engineering Scaffolds

Organ transplantation is the only permanent therapy for patients with end-stage organ failure [1]. The most significant challenge facing organ transplantation is the need for available tissue. There are more than 80,000 patients currently on the organ donor waiting list, with more than 70,000 awaiting livers and kidneys alone [2]. These are complex tissues with intricate arrangements of multiple cell types. It is this well-preserved microarchitecture that determines the physiologic organ-specific function. The shortage of available organs as well as the need for other replacement tissues has inspired rapid growth in the field of "tissue engineering".

Tissue engineering is an emerging field aimed at addressing the growing disparity between needed and available tissues by developing alternative therapies to tissue and organ transplantation based on implantation of living cells. Several excellent reviews of the field can be found in the literature [1, 3-6]. In these approaches, cells are not simply implanted alone, but rather in association with a support matrix. The nature and complexity of the supports is highly variable and has increased considerably over the past several decades owing to new understandings of the relationships between cell growth and cell support.

As early as 1933, investigators were implanting living cells. At that time, the living elements were encased in a simple polymer membrane [7]. Today, methods for implanting live cells are diverse, ranging from encasement in chemically specific hydrogels [8], to seeded on porous polymer surfaces [9], to containment in silicon microwells [10].

1.1.2 Biodegradable Scaffold Approach

In 1993, the success of support matrices inspired a novel approach involving the implantation of cells on synthetic bioresorbable scaffolding [11]. This now common tissue engineering paradigm (Figure 1.1) consists of three

principle steps: 1) Cell Acquisition – cells can be obtained by tissue biopsy or differentiated from progenitors or stem cells and expanded in culture. 2) Cell Seeding – cells are expanded in culture, seeded on an engineered polymer scaffold, and cultured *in vitro* to increase cell number and tissue integrity. 3) Implantation – the cell/polymer construct is implanted *in vivo* to integrate and serve its organ-specific function while the polymer is resorbed in a biologically compatible fashion. This approach has been extensively explored for a wide range of tissues over the past decade [12-15], and its feasibility has been thoroughly demonstrated. The focus is now shifting toward one of understanding mechanisms, optimizing scaffolds, selecting appropriate cells, and perfecting implantation methods in order to make the approach therapeutically viable. This thesis focuses on development of a fabrication platform for building high performance scaffolding that can be used to address many of the major challenges currently facing tissue engineering.

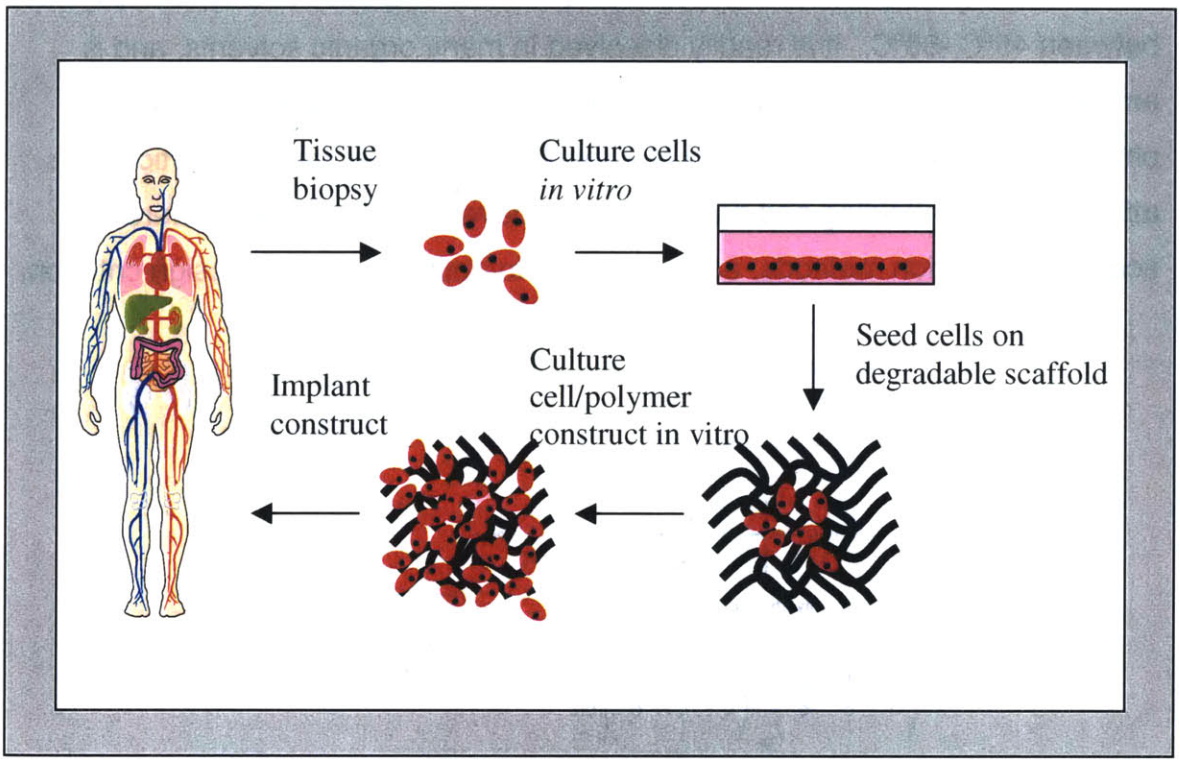

Figure 1.1 Tissue engineering paradigm using biodegradable polymers .

1.1.3 Polylactic Glycolides

The most commonly used synthetic bioresorbable polymers are the (α-hydroxy) aliphatic polyesters, polyglycolic acid (PGA), polylactic acid (PLA), and their copolymers (PLGA) (Figure 1.2) [16]. These materials have a long history of Food and Drug Administration (FDA) approval for use as surgical sutures, pins, and microsphere drug delivery vehicles [17, 18]. The linear chain polymers are degraded by hydrolysis to yield lactic acid and glycolic acid, natural biomolecules that are readily metabolized *in vivo* (Figure 1.2) [19]. Due to the presence of an additional methyl moiety, the polylactic acids are sterically hindered from hydrolytic attack and therefore degrade slower than the glycolic acids. By varying the monomer ratio in PLGA copolymers, the degradation kinetics can be systematically varied from days to months. In this thesis, the slowly degrading 85L:15G copolymer is used (details in Appendix B).

There is a long history of growing cells on PLGA scaffolds. PLGA is an amorphous thermoplastic linear chain polymer with a glass transition temperature between 45°C -55°C. It is readily dissolved in many organic solvents, and is amenable to a wide range of processing techniques. The ability to control physicochemical properties of the resorbable material has made it particularly attractive for scaffolding and has lead to the development of many different scaffold fabrication methods, each designed to optimize specific design criterion.

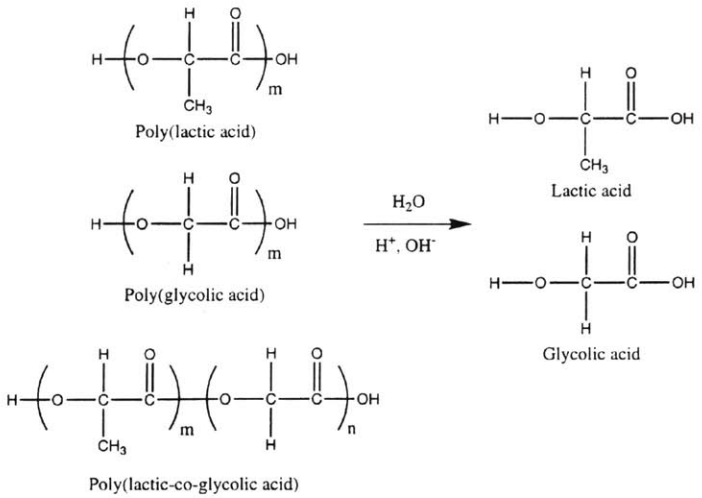

Figure 1.2 Chemical structure of the (α-hydroxy) aliphatic polyesters polyglycolic acid (PGA), polylactic acid (PLA), and polylactic-co-glycolic acid (PLGA). [19]

1.2 Organ Fabrication Concept

It is clear that physiologically, functional units of tissue microarchitecture are organized on the size scale of microns to millimeters [3]. If vital organ fabrication is to be possible, these functional units must be recapitulated in a grossly parallel fashion [20]. In addition, the scaffold must be fashioned with a microvascular equivalent to oxygenate and nourish cells in all areas of the construct [21]. At this stage, it is not yet clear to what extent the scaffold should explicitly depict microarchitecture or microvasculature. However, the processes developed in this thesis fortunately allow design of engineered tissue architecture at any level that it might be required, from small 5-10μm capillaries and hepatic sinusoids to larger millimeter-scale organized branchings of vascular-like conduits. Such a capability enables a wide range of configurations of varied complexity. Organ-specific parenchymal cells could be placed in generic pore-like wells, patterned in stacked planar cellular sheets, or even encouraged to develop into self-organized spheroids. Alternatively, more explicit topologies can be imagined, such as vascular networks designed to mimic physiologic parameters; either function-determining flow rates and shear stresses or morphological metrics describing vessel branching patterns and distributions.

As an example of a non-explicit design at the microscale, consider the engineering of a generic bulk organ such as the liver. In the case of the liver, the desired organ-specific function is metabolic modification and detoxification of the blood. By building a large microfluidic scaffold that could be placed in-line with the vascular circulation, blood would have access to the cell-seeded interior of the device. Stacking alternating layers of microfabricated wells (~200μm cubes) and overlaying microfluidic networks allows one to design microwell interconnectivity, enabling efficient and systematic seeding as well as continuous flow culturing of small units of tissue *in vitro* and even perfusion with whole blood *in vivo*. Eventually, more complexity could be built in by incorporating nanoporous membranes or creating other selective barriers to cells while remaining permeable to gas and macromolecules. The generic organ fabrication concept is shown schematically in Figure 1.3.

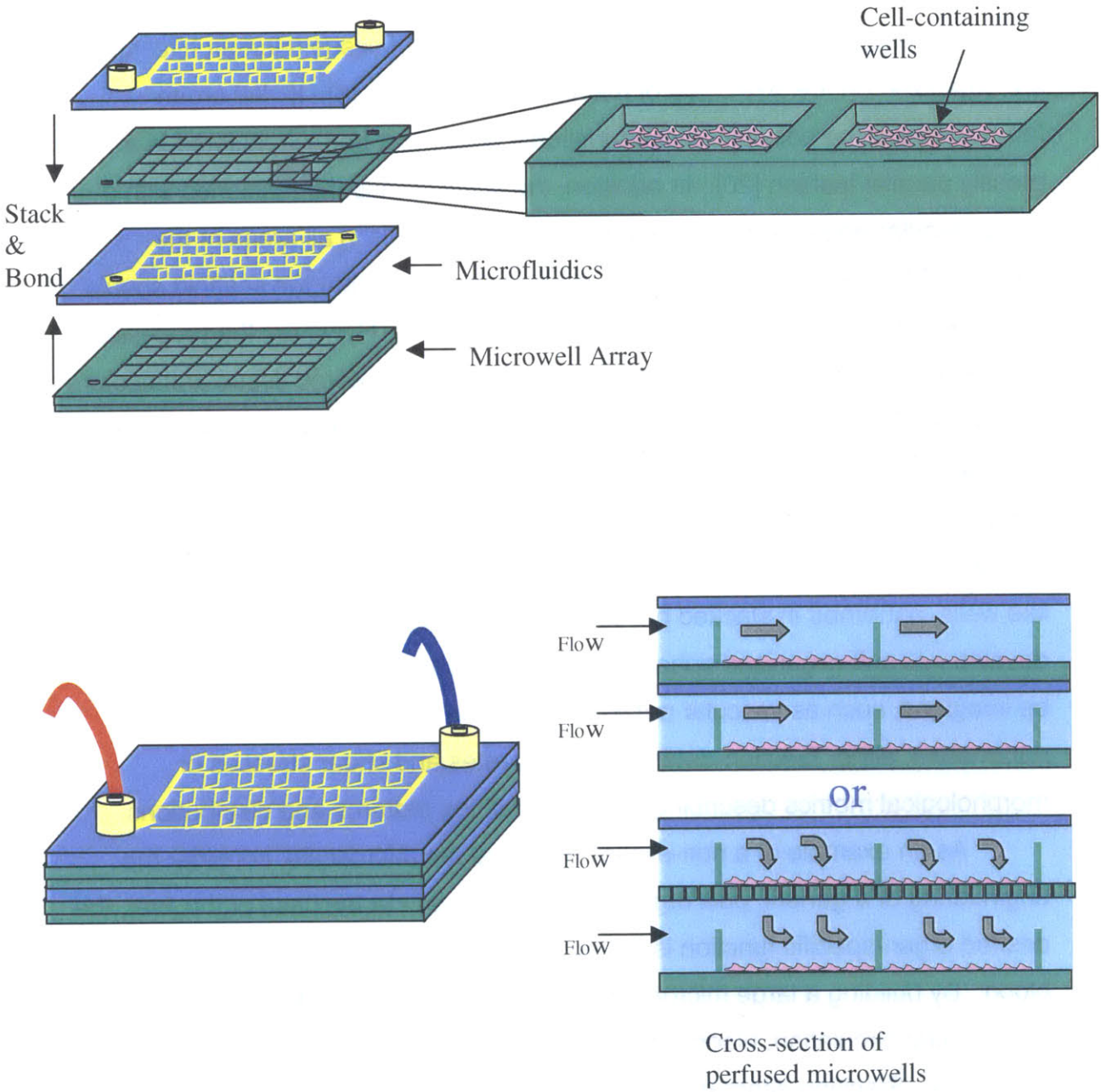

Figure 1.3 Example of a generic organ fabrication design using three-dimensional microfabricated biodegradable scaffolding. Combinations of cell-containing microwells and microfluidic interconnections allow scaffolds to be seeded and perfused efficiently and methodically.

1.3 Existing Scaffold Fabrication Technologies

1.3.1 Scaffold Design Criteria

Several design criteria have been identified to guide scaffold fabrication, each motivated by a functional requirement. Initial emphasis was placed on the need for large surface-area-to-volume ratios to seed attachment-dependent cells, and large void volumes to allow three-dimensional growth of tissue within the matrix. These criteria inspired the development of three-dimensional porous scaffolds with pore sizes ranging from 50-500μm, and porosities ranging from 50-99% [9, 22, 23]. Pore interconnectivity was emphasized as a critical determinant of mass transport, host tissue in-growth, and tissue engineered cellular outgrowth. It was specified that diffusive transport of oxygen and metabolites be sufficient to maintain cell viability until the in-growth of vascularized tissue or the development of *de novo* blood vessels could be achieved. The scaffold was also required to provide sufficient mechanical support to prevent collapse under the stress of a fibrous capsule [24]. At the same time, it was desired that the scaffold not significantly restrain growth of new tissue from inside. These final criteria are typically met been by selecting resorbable polymers that degrade on the same time scale as tissue growth.

A wide variety of porous and fibrous scaffolds have been developed over the last decade and today their fabrication is fairly routine. Investigators are still in search however, of the optimal scaffold that is sufficiently flexible to simultaneously meet diverse design criteria. At these early stages, the criteria are still somewhat speculative and dynamic. Therefore, a versatile approach is needed to both aid in systematic identification of important scaffold features, and adapt to new design criteria as relationships between tissue development and scaffold design are revealed. The microfabricated scaffolding platform described in this thesis addresses these issues by providing 1) unmatched geometrical resolution and reproducibility, 2) explicit control of mass transport and pore interconnectivity, 3) dramatic improvements in design flexibility to allow organization and recapitulation of tissue microarchitecture, and 4) scalability and

manufacturability by making the fabrication process rapid, efficient, and accessible to investigators without specialized equipment.

Geometrical Precision and Reproducibility

Scaffold pore size has been demonstrated to influence implanted cell growth and vascularization [25]. Evidence from examination of scaffolds with pores and conduits of different sizes and interconnectivity suggest that optimum pore sizes are tissue specific. Meeting strict requirements on pore size and interconnectivity will require improved control and precision because current methods only control bulk properties such as *average* pore size, shape, and distribution (Figure 1.4) [23]. The reproducibility inherent in high precision methods such as microfabrication will allow experiments to be more effectively compared by enabling systematic variation of scaffold properties.

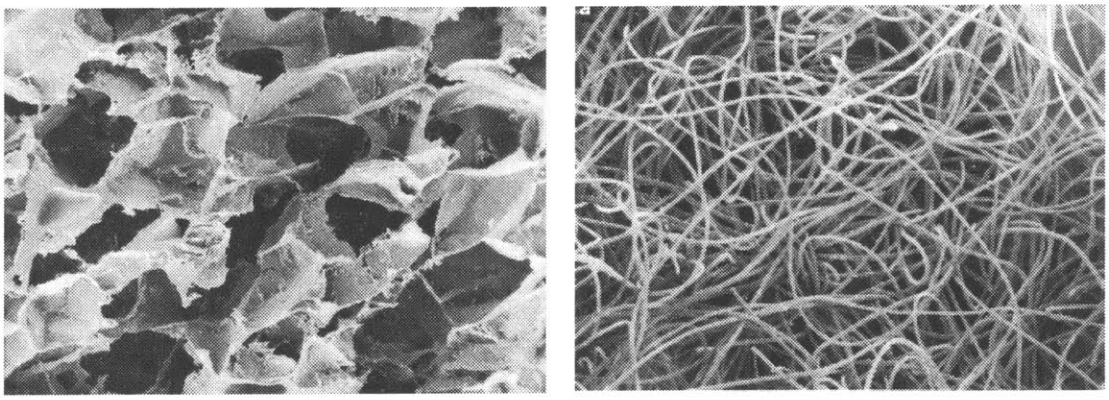

Figure 1.4 Conventional A) porous and B) fibrous scaffolds with control limited to bulk properties of average pore size size, shape, distribution, and interconnectivity. Nominal pore sizes and interfiber distances are several hundred microns.

Mass Transport Limitations

Metabolically active cells require a continuous supply of nutrients and removal of waste. In porous scaffolds, cells rely solely on diffusive transport to deliver oxygen and metabolites. The thickness of cell-seeded scaffolds is therefore limited to millimeters in size, the diffusion distance of oxygen in tissue, before cells at the scaffold center become hypoxic [26]. In order to maintain the

viability of larger cell-seeded scaffolds, methods for rapid vascularization must be developed [27].

The formation of blood vessels follows one of two paths – vasculogenesis or angiogenesis. Vasculogenesis is the development of blood vessels *de novo* from groups of endothelial cells, as occurs during early development. Angiogenesis, in contrast, is branching of preexisting vessels to form new blood vessel networks (often hypoxia induced). This occurs physiologically in pregnancy and wound healing, and pathologically in large vascularized tumors.

Several promising methods have been demonstrated to improve tissue engineering scaffold vascularization, however this work is still in its infancy. Early attempts involved prevascularization [28]. More recently, naked DNA has been delivered via the scaffold to transfect host cells [29] and cause host synthesis of Vascular Endothelial Growth Factor (VEGF), a potent angiogenic factor. Angiogenic factors implanted directly into scaffolds have also been shown to accelerate vascularization, but the resulting vessels remained immature, unstable, and eventually regressed [30]. However, when more complex scaffolds were designed to deliver two factors VEGF, and Platelet Derived Growth Factor (PDGF) with different release kinetics, more mature and sustainable vessels developed [31]. Another promising approach involves preseeding scaffolds with endothelial cells. This avoids the requirement that host cells migrate and invade the scaffold, as such a process can require days or weeks depending on scaffold size [32]. Despite these encouraging results, there is still no clear solution to the problem of rapidly vascularizing large cell-seeded scaffolds.

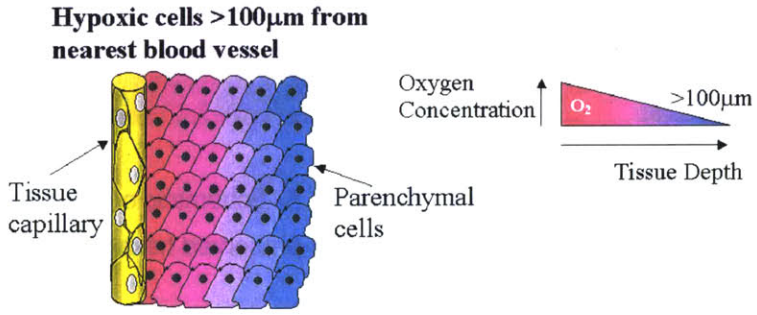

Figure 1.5 Cells more than hundreds of microns from blood vessels become hypoxic and recruit the branching of existing vessels through a process known as angiongenesis [33].

Tissue Microarchitecture

Structure-function relationships have long been emphasized in physiology, even at the microscale, the level of cells and molecules. The microscopic arrangement of multiple cell types and the patterns of molecular ligands present on extracellular matrix components are critical for the development of a natural tissue microarchitecture, and this microarchitecture is a key determinant of organ-specific function. For example, the zonation of liver lobules and the tortuous renal tubule system are evidence for the importance of microarchitecture in physiology [34]. Another microstructural component, the distributed capillary system and hierarchical branching blood vessel networks are fundamental to the maintenance of the tissues they perfuse. If the field of tissue engineering is to attempt growth of complex bulk organs such as desperately needed livers and kidneys, guidance and recapitulation of the complex microarchitecture will be important [20, 21]. Many of the complex organized arrangements, such as liver sinusoids, renal tubules, and capillary beds are actually massively parallel systems of conduits only tens of microns in diameter, and can be viewed as examples of biological microfluidic networks. Therefore, the primary goal of this thesis is to develop a microfluidics-enabled biodegradable scaffold.

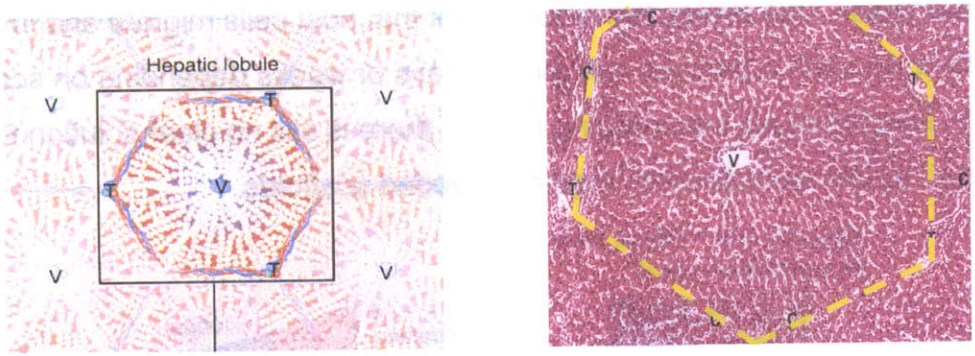

Figure 1.6 Example of biological microfluidics (10-20um): A) Schematic of interconnected sinusoids making up a hepatic lobule, B) Histology of well-preserved hexagonal hepatic lobule with interconnected sinusoids. [34]

Manufacturability and Scalability

In addition to mass transport limitations, there are additional challenges related to scalability. Scaffold size is currently limited by transport-dependent fabrication processes such as leaching of pore-forming particulates or porogens, solvent evaporation, and scaffold drying. In addition, as more cells are implanted and scaffold sizes increase, inadequate pore interconnectivity is becoming a major barrier to well-distributed cell seeding, and microvascular in-growth [23].

Design Variable	Rationale	Design Criteria
Void Volume	Volume for cell growth Volume for mass transfer	50-90% porosity Maximize
Surface Area	Area for cell attachment	Maximize
Interconnectivity	Efficient transport Cell and tissue in- out growth	Designable interconnections ideally fully interconnected
High Resolution and Precision	Design microarchitecture Organize cells and molecules	Requires <10μm resolution and ~1μm precision
Design Flexibility	Mass transport *in vitro* Vascularization approaches	Heterogeneous feature sizes, shapes and distributions
Scalablility	Deliver therapeutic # of cells	~100cm^3 sized scaffolds
Manufacturabiltiy & Accessibility	Rapid and simple fabrication Reproducibility	Minutes rather than days Micron reproducibility

Table 1.1 Summary of commonly used tissue engineering support scaffold design criteria.

1.3.2 Scaffold Fabrication and Polymer Processing

Initial design criteria requiring high porosity and sub-millimeter pore sizes inspired the development of several now conventional synthetic scaffold fabrication techniques. Solvent casting and particulate leaching involves casting a polymer solution around a bed of salt particles and evaporating the organic solvent to solidify the polymer [35]. Once dry, the salt is "leached" or dissolved in an aqueous solution, leaving behind pores. In this approach, pore size is controlled by mechanically filtering the porogen before casting, and pore geometry is simply the arbitrary shape of the porogen. Over the past decade, this method and its many variations [36-38] have been adapted to a wide range of porogens and have become one of the most commonly used techniques for scaffold fabrication. However, while the method has been optimized to yield good control over bulk scaffold properties such as total porosity and average

pore size, individual pore properties are not well controlled. This method has additional drawbacks related to its reliance on transport-dependent processes such as leaching and vacuum drying, causing fabrication time to scale poorly with scaffold size.

Textile materials, such as woven and non-woven fiber meshes have also been used to create porous structures with controllable average interfiber distances and density, but once again, micron scale control of fiber arrangement is not possible [39]. Several methods have been developed to incorporate drugs in the scaffold. Phase inversion, in which two phases – a polymer rich phase and a polymer lean phase are formed by inducing phase separation with subsequent sublimation of the solidified solvent [9]. Alternatively, high pressure processing can build scaffolds without using harmful chemicals or high temperatures [40]. The method involves the low temperature pressurization of a polymer solution using CO_2 and the creation of a thermodynamic instability to nucleate pores. Other methods include melt molding [41], hydrocarbon templating for rapid porogen removal [42], and membrane lamination in which thin films of degradable polymer are cast and laminated by locally dissolving the surfaces with applied solvent [1].

Processing Technique	Advantages	Disadvantages
Solvent Casting	Simple process and low viscosity for filling small gaps and interstices	Slow porogen leaching and drying. Potential for cytotoxic residual solvents
Fiber Bonding	Can shape and modulate strength of fibrous scaffolds	Poor control of fiber arrangement & local interfiber distances
Phase Inversion	Can incorporate active agents.	Requires sublimation apparatus. Limited pore sizes and shapes.
High Pressure Processing	Can incorporate active agents such as angiogenic factors	Requires specialized equipment
Melt Molding	Easily shaped in the melt form	High temperatures required for non-amorphous polymers
Hydrocarbon Templating	No thickness limitation because of rapid leaching	Solvent residue still requires long drying times
Membrane Lamination	Can create large composite structures	Residual solvents and slow processing

Table 1.2 Conventional biodegradable scaffold fabrication techniques.

More recently, advanced processing techniques have emerged to address some of the shortcomings of conventional scaffolding methods. In response to new design criteria requesting higher resolution and design flexibility, Solid Free-form Fabrication (SFF) [39, 43], Three-Dimensional Printing (3DP) [44, 45], ink jetting polymer solution, direct write laser etching [46], electrospinning, solvent casting on microstructured surfaces [47], stamping microstructured surfaces into solvent cast films [48], and several other novel processes have been developed. Although each addresses one or many of the criterion discussed here, methods are not available that meet a large number of the stated design criteria. Nearly all approaches suffer resolution limitations that limit their reproducibility to the size scale of several hundred microns. Most techniques still rely on solvents and therefore necessitate long drying steps that leave processing times at days. Finally, while many of the advanced processes allow arbitrary designs to be realized, they require specialized equipment and are therefore not readily adapted by a wide range of investigators.

Techniques	Resolution Demonstrated	Precision & Reproducibility	Design Flexibility	Process Time and Equipment
Solid Free Form Fabrication	200-500μm	Limited by trapped porogens and particle sizes	Very Flexible	Requires specialized equipment Days to dry
3D Printing	200-500μm	Trapped porogens	Very Flexible	Specialized equipment Hours to construct, Days to dry
Laser Etching	50-100μm	Spot size limited	Planar structures	Requires laser source Serial process
Electrospinning	200-500μm	Poor	Arbitrary fiber placement	Specialized equipment required. Limited to fibrous structures
MIMIC Casting	50μm	Shrinkage limited	Planar structures	Microfabricated mold required. Minutes to cast. Days to dry
Stamping	50μm	Shrinkage limited	Planar structures	Microfabricated mold required. Minutes to cast. Days to dry

Table 1.3 Advanced biodegradable scaffold fabrication techniques.

Despite the many fabrication alternatives, the limitations of geometrical precision, manufacturability, rapid vascularization, and recapitulation of tissue microarchitecture remain. In this thesis, high-precision techniques collectively known as microfabrication are employed to process biodegradable PLGA with a wide range of geometries, from microns to centimeters. Microfabrication, an ideal tool for addressing many of the scaffold fabrication limitations, offers improved precision and reproducibility, manufacturability and scalability, and design flexibility. Micromachined devices are also particularly appropriate tools for addressing problems in medicine and biology because of their ability to organize, manipulate, and analyze on the size scale of individual cells and macromolecules. As it is the technology of choice in this thesis, the next section reviews microfabrication and microtechnology, providing background for the PLGA microfabrication platform development, the main topic of this thesis.

1.4 Microtechnology in Medicine and Biology

1.4.1 Microfabrication and Micromachining

Microfabrication, originally developed for the microelectronics industry, leverages photolithography to achieve micron scale resolution. By exposing photosensitive polymer thin films through lithographic masks, high-resolution patterns are faithfully translated onto surfaces of substrates such as silicon or glass. Etching and deposition compliment photolithographic patterning by selectively modifying the substrate in a subtractive or additive fashion. This planar processing technology is straightforward, and has been commonly used to build microelectronic integrated circuits and microelectromechanical systems (MEMS) for several decades [49-52]. In addition to dimensional precision, microfabrication offers advantages of micron resolution, massively parallel processing, exceptional reproducibility, and well-established manufacturability.

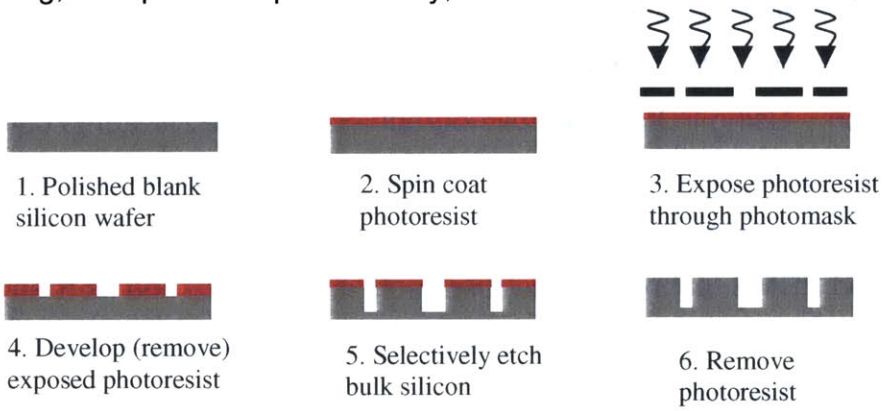

Figure 1.7 Typical silicon microfabrication process: Thin film deposition (Step 2), photolithography (Steps 3-4), and etch (Step 5).

There are several examples of silicon-based tissue engineering devices. Nanoporous silicon microwells have been fabricated for immunoisolation of pancreatic islet cells [53]. A controlled release microchip was developed to release very small doses of drug from an addressable array [54]. In addition, silicon has been used as a microstructured substrate for demonstration of several two-dimensional *in vitro* tissue models by building designable networks of neurons [55], topology-guided growth of cells, and removable cellular sheets [56]. Despite these successful demonstrations, silicon has only had a modest impact

as a biomaterial, due in part to its rigidity and opacity. However, recent reports on porous silicon are renewing interest in the material [57]. Silicon, fundamentally has additional disadvantages of expense, long fabrication times, and the need for cleanroom fabrication facilities. These drawbacks have lead to the development of rapid prototyping polymeric solutions that combine high-resolution photolithography and silicon microfabrication with a wide range of biocompatible polymeric materials.

1.4.2 Soft Lithography

One of the most commonly micropatterned polymers is polydimethylsiloxane (PDMS). This silicone elastomer is a network polymer prepared as a liquid prepolymer, cast on a microfabricated silicon surface, cured, and peeled to yield precise patterns in the flexible material [58]. This high-resolution replica molding process, limited only by the resolution of the microfabricated mold, represents an alternative paradigm to silicon-based microfabrication. Using PDMS, photolithographically defined features can be translated into a wide range of materials without developing new material-specific etchants or compromising already optimized processes [59, 60]. The advent of microstructured PDMS technology, dubbed "soft lithography," and its many closely related processes [61-63] has enabled a host of new applications in the areas of medicine and biology.

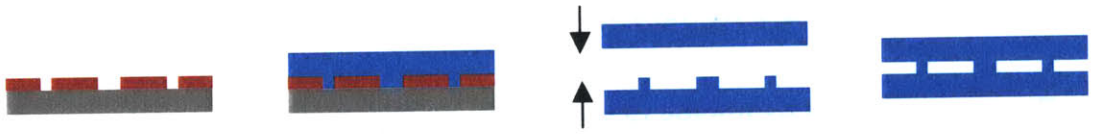

1. Etched silicon master mold

2. Cast, cure and peel PDMS from silicon mold

3. Plasma treat surfaces and bring into contact

4. Resulting bonded PDMS microchannels

Figure 1.8 Replica molding or "soft lithography" process flow used to make microfluidics.

1.4.3 Cell Patterning

Initially, micropatterned PDMS stamps were used to print or "ink" biomolecules on surfaces for the purpose of controlling surface properties and promoting specific attachment of cells – "cell patterning". This approach was exploited by several investigators to demonstrate the importance of microscale phenomena in governing the differentiated function of living cells. Investigators used patterning of cell attachment moieties to limit the area of cell attachment and thereby modulate the shape of individual cells [64]. With the aid of microfabrication, they demonstrated that constraining cell shape can influence cell cycle and tube formation in endothelial cells [65], and they continue to employ these techniques to probe the importance of mechanical signal transduction and its connection with gene expression. In other studies, investigators utilized designable microscale through-holes in PDMS layers to mechanically mask cell seeding [66] and systematically vary the amount of heterotypic interaction between arrangements of parenchymal and nonparenchymal cells [67, 68]. They used this control to demonstrate preservation of hepatocyte-specific functions such as albumin and urea synthesis that are historically difficult to maintain in culture. It is important to note that all of these studies were performed on a single two-dimensional surface because microfabrication is fundamentally a planar processing technology. The demonstrations were not intended to be implanted or used *in vivo*. However, through their work, these and other investigators have demonstrated the power of using micropatterning to exert microscale control and potentially maintain and even augment differentiated function of implantable cells.

1.4.4 Microfluidics

The development of an oxygen plasma surface treatment that enables bonding of patterned PDMS films to silicon, glass, and other layers of PDMS has recently elevated replica molding soft lithography to a three-dimensional technology [69]. After its development, the robust bonding technique was

immediately exploited to inexpensively build microfluidic devices and complex multi-layer networks [70, 71]. PDMS microfluidics ultimately lead to an explosion of new biomedical applications. The fact that precision silicon master molds could be fabricated once and used repeatedly to inexpensively build microfluidic devices made this approach immediately accessible to chemistry and biology labs not equipped with dedicated cleanrooms, and it significantly broadened the utilization of microtechnology. In a short time, soft lithography found applications in analytical chemistry, biochemistry, molecular biology, and medical diagnostics, and today remains a prominent fabrication technique for exploration in medicine and biology, including the study of living cells.

1.4.5 Cells in Microfluidic devices

Initial microfluidic applications focused on biomolecules, developing systems for separation and analysis. However, more recently, living cells have been introduced into microfluidic channels in cell sorting chips [72], microchannel embryo manipulation for *in vitro* fertilization [73], and a variety of approaches to microscale flow cytometry [74, 75]. Adjacent laminar flows have been creatively employed to assemble dynamic chemical gradients for the study of cellular chemotaxis [76-78], to dynamically effect cell attachment [79, 80], and to introduce molecules into cells from solution with subcellular resolution [81]. However, while cells have been introduced into microfluidic systems for analysis and manipulation, they are not typically cultured long term in microfluidic channels. Instead, a common approach involves using a three-sided PDMS microfluidic network on a standard polystyrene culture surface to seed cells in known locations with subsequent removal of the PDMS before medium changes or flow is required to maintain oxygen tension and metabolite balance [70]. In this thesis, long-term continuous-flow cell culture in biodegradable microdevices and microfluidics is proposed. Therefore, the thesis concludes with a description of a viable two-week mammalian cell culture in PDMS prototype microfluidic networks, demonstrating the feasibility of seeding and culturing cells under flow conditions in the confined geometries of biodegradable microfluidic networks.

1.5 Thesis Objectives and Overview

This thesis describes the development of a high resolution, high precision, designable, reproducible, and manufacturable biodegradable microfabrication platform. Microstructured films are fabricated, and a bonding technique is developed to enable scaling into three-dimensions. The power of the processes is demonstrated by building a fully biodegradable microfluidic network with channels on the same size scale as physiologic capillaries. Finally, to demonstrate the feasibility of seeding and culturing cells in the networks, prototype devices are populated with endothelial cells and continuous-flow cultured to near confluence. It is hoped that the techniques developed in this thesis will augment the tissue engineering toolset and enable creative solutions to the challenging problems of vascularizing cell-seeded constructs, and guiding the organization of complex tissue microarchitecture. The specific objectives of this thesis are:

1) To develop methods for reliably creating high resolution, high precision microstructures in PLGA biodegradable polymer films.

2) To develop a low temperature, solventless, adhesiveless bonding process capable of sealing PLGA microchannels without causing significant plastic deformation of microstructures.

3) To develop an inlet and outlet scheme that, combined with the microstructuring and bonding processes, can enable fabrication and characterization of fully biodegradable microfluidic networks.

4) To characterize and test the microfluidic networks for occlusions, leaks, and fluidic resistance, and explore the feasibility of using the networks to support cell culture.

The primary accomplishment described in this thesis is the reproducible fabrication of a three-dimensional biodegradable microfluidic network. An overview of the fabrication process is shown pictorially in Figure 1.9.

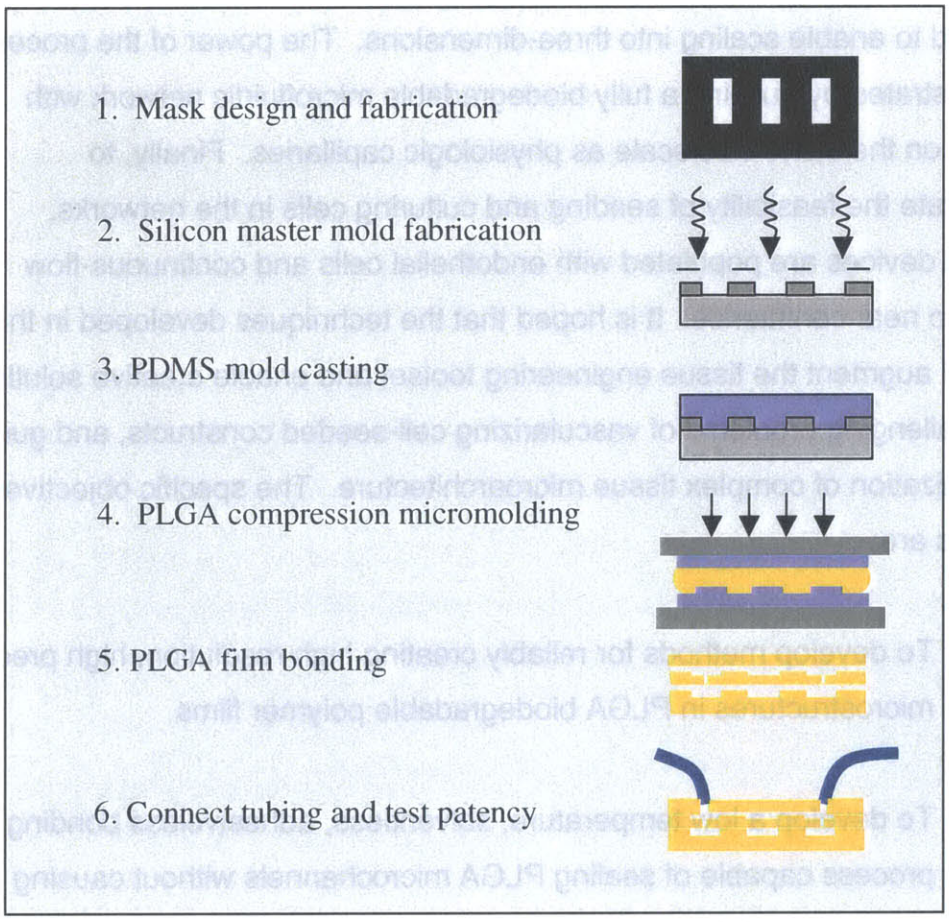

Figure 1.9 Biodegradable microfluidics fabrication process overview. 1) Photomasks are designed, fabricated, and 2) used to define microstructures in silicon. 3) This pattern is transferred to a secondary PDMS mold and 4) used to compression micromold the biodegradable polymer, polylactic-co-glycolic acid (PLGA 85:15) by controlling time, temperature, and applied force. 5) The resulting films are bonded using an optimized thermal fusion process, and 6) fitted with connectors and tubing for perfusion and seeding with cells.

Chapter 1 provided background for the work, an overview of the thesis, and a forward-looking proposal for a generic biodegradable microfabricated scaffold to aid organ fabrication.

Chapter 2 describes the creation of micron scale features in silicon and the high fidelity transfer of the surface microstructures from silicon masters to flexible elastomeric PDMS films and then to PLGA biodegradable polymer films. Specific attention is focused on comparing solvent polymer processing with melt polymer processing. Melt processing is ultimately chosen as the preferable process, and the remainder of the chapter describes process parameter selection and explores the range of structures that can be fabricated using the approach.

Chapter 3 describes the development of a thermal fusion bonding process that enables stacking of PLGA microstructured films to form three-dimensional biodegradable constructs. A theoretical model is developed to guide the selection of process times and temperatures in order to avoid temperature-induced plastic deformation and microchannel collapse, the dominant mode of failure during bonding. Using the model, a wide range of geometries are bonded in a robust and reproducible fashion.

Chapter 4 describes the development of extruded biodegradable fluidic connector ports that are integrated with the patterned PLGA surfaces to create monolithic microfluidic networks. The chapter describes fabrication of two complex branching network designs, demonstrates their patency, and characterizes their resistance to pressure-driven flow.

Chapter 5 describes a feasibility study in which endothelial cells are seeded and cultured in prototype PDMS microfluidic networks similar to the designs fabricated in PLGA throughout Chapter 4. Continuous flow of medium is used to support the cultures, and they are maintained sterile and unoccluded for two weeks, achieving 80-90% confluency.

Chapter 6 provides a summary of the major accomplishments in the work, and discusses future work and conclusions.

1.6 References

[1] Lanza, R.P., R. Langer, and W.L. Chick, eds. *Principles of Tissue Engineering.* Academic Press: Austin, 1997.

[2] UNOS, U.N.f.O.S., *Report of the U.S. Organ Transplant Waiting List.* UNOS: Richmond, VA, 2002.

[3] Griffith, L.G. and G. Naughton, "Tissue Engineering - Current Challenges and Expanding Opportunities". Science. 295: p. 1009-1014, 2002.

[4] Vacanti, J.P. and R. Langer, "Tissue Engineering: the Design and Fabrication of Living Replacement Devices for Surgical Reconstruction and Transplantation". The Lancet. 354(Suppl I): p. 32SI-34SI, 1999.

[5] Marler, J.J., J. Upton, R. Langer, and J.P. Vacanti, "Transplantation of Cells in Matrices for Tissue Engineering". Advanced Drug Delivery Reviews. 33: p. 165-182, 1998.

[6] Niklason, L.E. and R. Langer, "Prospects for Organ and Tissue Replacement". Journal of American Medical Association. 285(5): p. 573-576, 2001.

[7] Fuchs, J.R., B.A. Nasseri, and J.P. Vacanti, "Tissue Engineering: A 21st Century Solution to Surgical Reconstruction". Annals of Thoracic Surgery. 72: p. 577-591, 2001.

[8] Lee, K.Y. and D.J. Mooney, "Hydrogels for Tissue Engineering". Journal of Chemical Reviews, 2001.

[9] Mikos, A.G. and J.S. Temenoff, "Formation of Highly Porous Biodegradable Scaffolds for Tissue Engineering". Electronic Journal of Biotechnology. 3(2), 2000.

[10] Desai, T.A. and M. Ferrari, *Microfabricated Biocapsules for the Immunoisolation of Pancreatic Islets of Langerhans*, in *Bioengineering*. University of California San Francisco and University of California Berkeley: Berkley, CA, 1998.

[11] Langer, R. and J.P. Vacanti, "Tissue Engineering". Science. 260(5110): p. 920-926, 1993.

[12] Shinoka, T., D. Shumtin, and P.X. Ma, "Creation of Viable Pulmonary Artery Autografts Through Tissue Engineering". Plastic Reconstructive Surgery. 88: p. 733-759, 1998.

[13] Niklason, L.E., J. Gao, and W.M. Abbott, "Functional Arteries Grown In Vivo". Science. 284: p. 489-493, 1999.

[14] Organ, G.M., D.J. Mooney, L.K. Hansen, B. Schloo, and J.P. Vacanti, "Transplantation of Enterocytes Ultilizing Polymer-Cell Constructs to Produce Neointestine". Transplant Proc. 24: p. 3009-3011, 1992.

[15] Shinoka, T., P.X. Ma, and D. Shumtin, "Tissue engineered Hear Valves". Circulation. 94(Suppl II): p. 164-168, 1996.

[16] Peter, S.J., M.J. Miller, A.W. Yasko, M.J. Yaszemski, and A.G. Mikos, "Polymer Concepts in Tissue Engineering". Journal of Biomedical Materials Research (Applied Biomaterials). 43: p. 422-427, 1998.

[17] Wang, N., X.S. Wu, C. Li, and M.F. Feng, "Synthesis, Characterization, Biodegradation, and Drug Delivery Application of Biodegradable Lactic/Glycolic Acid Polymers. Part I: Synthesis and Characterization". Journal of Biomaterial Science Polymer Edn. 11(3): p. 301-318, 2000.

[18] Wu, X.S. and N. Wang, "Synthesis, Characterization, Biodegradation, and Drug Delivery Application of Biodegradable Lactic/Glycolic Acid Polymers. Part II: Biodegradation". Journal of Biomaterial Science Polymer Edn. 12(1): p. 21-34, 2001.

[19] Baldwin, S.P. and M.W. Saltzman, "Materials for Protein Delivery in Tissue Engineering". Advanced Drug Delivery Reviews. 33: p. 71-86, 1998.

[20] Desai, T.A., "Micro and nanoscale structures for tissue engineering constructs". Medical Engineering & Physics. 22: p. 595-606, 2000.

[21] Bhatia, S.N. and C.S. Chen, "Tissue Engineering at the Micro-Scale". Biomedical Microdevices. 2(2): p. 131-144, 1999.

[22] Chen, G., T. Ushida, and T. Tateishi, "Scaffold Design for Tissue Engineering". Macromol. Biosci. 2: p. 67-77, 2002.

[23] Yang, S., K.-f. Leong, Z. Du, and C.-k. Chua, "The Design of Scaffolds for Use in Tissue Engineering. Part I. Traditional Factors". Tissue Engineering. 7(6): p. 679-689, 2001.

[24] Babensee, J.E., J.M. Anderson, L.V. McIntire, and A.G. Mikos, "Host Response to Tissue Engineered Devices". Advanced Drug Delivery Reviews. 33: p. 111-139, 1998.

[25] Zeltinger, J., J.K. Sherwood, D.A. Graham, R. Mueller, and L.G. Griffith, "Effect of Pore Size and Void Fraction on Cellular Adhesion, Proliferation, and Matrix Deposition". Tissue Engineering. 7(5): p. 557-572, 2001.

[26] Mooney, D.J. and A.G. Mikos, "Growing New Organs". Scientific American. 280: p. 60-65, 1999.

[27] Soker, S., M. Machado, and A. Atala, "System for Therapeutic Angiogenesis in Tissue Engineering". World Journal Urology. 18: p. 10-18, 2000.

[28] Mikos, A.G., S.M. Leite, J.P. Vacanti, and R. Langer, "Prevascularization of Porous Biodegradable Polymers". Biotechnology and Bioengineering. 42: p. 716-723, 1993.

[29] Shea, L.D., E. Smiley, J. Bonadio, and D.J. Mooney, "DNA Delivery from Polymer Matrices for Tissue Engineering". Nature Biotechnology. 17: p. 551-554, 1999.

[30] Murphy, W.L., M.C. Peters, D.H. Kohn, and D.J. Mooney, "Sustained Release of Vascular Endothelial Growth Factor from Mineralizaed Poly(lactic-co-glycolide) Scaffolds for Tissue Engineering". Biomaterials. 21: p. 2521-2527, 2000.

[31] Richardson, T.P., M.C. Peters, A.B. Ennett, and D.J. Mooney, "Polymeric System for Dual Growth Factor Delivery". Nature Biotechnology. 19: p. 1029-1034, 2001.

[32] Nomi, M., A. Atala, P. De Coppi, and S. Soker, "Principals of Neovascularization for Tissue Engineering". Molecular Aspects of Medicine, 2002.

[33] World Technology Evaluation Center, I., *WTEC Panel Report on Tissue Engineering Research.* National Institute of Standards and Technology: Gaithersburg, MD, 2002.

[34] Young, B. and J.W. Heath, *Wheater's Functional Histology.* New York: Churchill Livingstone, 2000.

[35] Murphy, W.L., R.G. Dennis, J.L. Kilney, and D.J. Mooney, "Salt Fusion: An Approach to Improve Pore Interconnectivity within Tissue Engineering Scaffolds". Tissue Engineering. 8(1): p. 43-52, 2002.
[36] Liao, C.-J., C.-F. Chen, J.-H. Chen, S.-F. Chiang, Y.-J. Lin, and K.-Y. Chang, "Fabrication of Porous Biodegradable Polymer Scaffolds Using a Solvent Merging/Particulate Leaching Method". Journal of Biomedical Materials Research. 59: p. 676-681, 2001.
[37] Chen, G., T. Ushida, and T. Tateishi, "Preparation of poly(L-lactic acid) and poly(DL-lactic-co-glycolic acid) foams by use of ice microparticulates". Biomaterials. 22: p. 2563-2567, 2001.
[38] Zein, I., D.W. Hutmacher, K.C. Tan, and S.H. Teoh, "Fused Deposition Modeling of Novel Scaffold Architectures for Tissue Engineering Applications". Biomaterials. 23: p. 1169-1185, 2002.
[39] Yang, S., K.-f. Leong, Z. Du, and C.-k. Chua, "The Design of Scaffolds for Use in Tissue Engineering. Part II. Rapid Prototyping Techniques". Tissue Engineering. 8(1): p. 1-11, 2002.
[40] Harris, L.D., B.-S. Kim, and D.J. Mooney, "Open Pore Biodegradable Matrices Formed with Gas Foaming". Journal of Biomedical Materials Research. 42: p. 396-402, 1998.
[41] Widmer, M.S., P.K. Gupta, L. Lu, R.K. Meszlenyi, G.R.D. Evans, K. Brandt, T. Savel, A. Gurlek, C.W.J. Patrick, and A.G. Mikos, "Manufacture of Porous Biodegradable Polymer Conduits by an Extrusion Process for Guided Tissue Regeneration". Biomaterials. 19: p. 1945-1955, 1998.
[42] Shastri, V.P., I. Martin, and R. Langer, "Macroporous Polymer Foams by Hydrocarbon Templating". Proceedings of the National Academy of Sciences. 97(5): p. 1970-1975, 2000.
[43] Wu, B.M., S.W. Borland, R.A. Giordano, L.G. Cima, E.M. Sachs, and M.J. Cima, "Solid Free-form Fabrication of Drug Delivery Devices". Journal of Controlled Release. 40: p. 77-87, 1996.
[44] Griffith, L.G., B.M. Wu, M.J. Cima, M.J. Powers, B. Chiagnaud, and J.P. Vacanti, "In Vitro Organogenesis of Liver Tissue". Annals of New York Academy of Sciences: p. 382-397, 1997.
[45] Kim, S.S., H. Utsunomiya, J.A. Koski, B.M. Wu, M.J. Cima, J. Sohn, K. Mukai, L.G. Griffith, and J.P. Vacanti, "Survival and Function of Hepatocytes on a Novel Three-Dimensional Synthetic Biodegradable Polymer Scaffold with an Intrinsic Network of Channels". Annals of Surgery. 228(1): p. 8-13, 1998.
[46] Kancharla, V.V. and S. Chen, "Fabrication of Biodegradable Polymeric Microdevices Using Laser Micromachining". Biomedical Microdevices. 4(2): p. 105-109, 2002.
[47] Vozzi, G., C.J. Flaim, F. Bianchi, A. Ahluwalia, and S.N. Bhatia, "Microfabricated PLGA Scaffolds: a comparative study for application to tissue engineering". Materials Science and Engineering C. 20: p. 43-47, 2002.
[48] Lu, L. and A.G. Mikos, *Modulation of Cell Morphology and Function Using Synthetic Biodegradable Polymers*, in *Bioengineering*. Rice University: Houston, TX, 1999.

[49] Voldman, J., M.L. Gray, and M.A. Schmidt, "Microfabrication in Biology and Medicine". Annual Reviews in Biomedical Engineering. 1: p. 401-425, 1999.
[50] Trimmer, W.S., *Micromechanics and MEMS Classic and Seminal Papers to 1990*. New York: IEEE Press, 1996.
[51] Madou, M., *Fundamentals of Microfabrication*. New York: CRC Press, 1997.
[52] Wolf, S. and R.N. Tauber, *Silicon Processing for the VLSI Era Volume 1: Process Technology*. Sunset Beach, CA: Lattice Press, 1986.
[53] Desai, T.A., D.J. Hansford, L. Kulinsky, A.H. Nashat, G. Rasi, J. Tu, Y. Wang, M. Zhang, and M. Ferrari, "Nanopore Technology for Biomedical Applications". Biomedical Microdevices. 2(1): p. 11-40, 1999.
[54] Santini, J.T.J., M. Cima, and R. Langer, "A Controlled-Release Microchip". Nature. 397(6717): p. 335-338, 1999.
[55] Curtis, A. and C. Wilkinson, "Review: Topographical Control of Cells". Biomaterials. 18: p. 1573-1583, 1997.
[56] Kaihara, S., J.T. Borenstein, R. Koka, and J.P. Vacanti, "Silicon Micromachining to Tissue Engineer Branched Vascular Channels for Liver Fabrication". Tissue Engineering. 6: p. 105-117, 2000.
[57] Chin, V., B.E. Collins, M.J. Sailor, and S.N. Bhatia, "Compatibility of Primary Hepatocytes with Oxidized Nanoporous Silicon". Advanced Materials. 13(24): p. 1877-1880, 2001.
[58] Jackman, R.J., J.L. Wilbur, and G.M. Whitesides, "Fabrication of Submicrometer Features on Curved Substrates by microcontact Printing". Science. 269: p. 664-666, 1995.
[59] Yang, H., P. Deschatelets, S.T. Brittain, and G.M. Whitesides, "Fabrication of High Performance Ceramic Microstructures from a Polymeric Precursor Using Soft Lithography". Advanced Materials. 13(1): p. 54-58, 2001.
[60] Xu, B., F. Arias, and G.M. Whitesides, "Making Honeycomb Microcomposites by Soft Lithography". Advanced Materials. 11(6): p. 492-495, 1999.
[61] Whitesides, G.M., E. Ostuni, S. Takayama, X. Jiang, and D.E. Ingber, "Soft Lithography in Biology and Biochemistry". Annual Reviews in Biomedical Engineering. 3: p. 335-373, 2001.
[62] Xia, Y. and G.M. Whitesides, "Soft Lithography". Angew. Chem. Int. Ed. 37: p. 550-575, 1998.
[63] Xia, Y. and G.M. Whitesides, "Soft Lithography". Annual Reviews in Material Science. 28: p. 153-184, 1998.
[64] Singhvi, R., A. Kumar, G.P. Lopez, G.N. Stephanopoulos, D.I.C. Wang, G.M. Whitesides, and D.E. Ingber, "Engineering Cell Shape and Function". Science. 264: p. 696-698, 1994.
[65] Chen, C.S., M. Mrksich, S. Huang, G.M. Whitesides, and D.E. Ingber, "Geometric Control of Cell Life and Death". Science. 276: p. 1425-1428, 1997.
[66] Folch, A., B.-H. Jo, O. Hurtado, D.J. Beebe, and M. Toner, "Microfabricated Elastomeric Stencils for Micropatterning Cell Cultures". Journal of Biomedical Materials Research. 52(2): p. 346-353, 2000.
[67] Bhatia, S.N., U.J. Balis, M.L. Yarmush, and M. Toner, "Probing Heterotypic Cell Interactions: Hepatocyte Function in Microfabricated Co-cultures". Journal of Biomaterial Science Polymer Edn. 9(11): p. 1137-1160, 1998.

[68] Bhatia, S.N., U.J. Balis, M.L. Yarmush, and M. Toner, "Effect of Cell-cell Interactions in preservation of Cellular Phenotype: Cocultivation of Hepatocytes and Nonparenchymal Cells". FASEB Journal. 13: p. 1883-1900, 1999.

[69] Jo, B.-H., L.M. Van Lerberghe, K.M. Motsegood, and D.J. Beebe, "Three-Dimensional Micro-Channel Fabrication in Polydimethylsiloxane (PDMS) Elastomer". Journal of Microelectromechanical Systems. 9(1): p. 76-81, 2000.

[70] Chiu, D.T., N.L. Jeon, S. Huang, R. Kane, C.J. Wargo, I.S. Choi, D.E. Ingber, and G.M. Whitesides, "Patterned Deposition of Cells and Proteins onto Surfaces by Using Three-dimensional Microfluidic Systems". Proceedings of the National Academy of Sciences. 97(6): p. 2408-2413, 2000.

[71] Unger, M.A., H.-P. Chou, T. Thorsen, A. Scherer, and S.R. Quake, "Monolithic Microfabricated Valves and Pumps by Multilayer Soft Lithography". Science. 288: p. 113-116, 2000.

[72] Quake, S.R. and A. Scherer, "From Micro- to Nanofabrication with Soft Materials". Science. 290(5496): p. 1536-1540, 2000.

[73] Zeringue, H.C., D.J. Beebe, and M.B. Wheeler, "Removal of Cumulus from Mammalian Zygotes using Microfluidic Techniques". Biomedical Microdevices. 3(3): p. 219-224, 2001.

[74] Voldman, J., M.A. Schmidt, M.L. Gray, and M. Toner, *A Microfabricated Dielectrophoresis Trapping Array for Cell-Based Biological Assays*, in *Electrical Engineering*. Massachusetts Institute of Technology: Cambridge. p. 152, 2001.

[75] Fu, A.Y., C. Spence, A. Scherer, F.H. Arnold, and S. Quake, "A Microfabricated Fluorescence-activated Cell Sorter". Nature Biotechnology. 17(11): p. 1109-1111, 1999.

[76] Jeon, N.L., S.K.W. Dertinger, D.T. Chiu, I.S. Choi, A.D. Strook, and G.M. Whitesides, "Generation of Solution and Surface Gradients Using Microfluidic Systems". Langmuir. 16: p. 8311-8316, 2000.

[77] Dertinger, S.K.W., D.T. Chiu, N.L. Jeon, and G.M. Whitesides, "Generation of Gradients Having Complex Shapes Using Microfluidic Networks". Analytical Chemistry. 73: p. 1240-1246, 2001.

[78] Jeon, N.L., H. Baskaran, S.K.W. Dertinger, G.M. Whitesides, L. Van de Water, and M. Toner, "Neutrophil Chemotaxis in Linear and Complex Gradients of Interleukin-8 Formed in a Microfabricated Device". Nature Biotechnology. 20(8): p. 826-830, 2002.

[79] Takayama, S., J.C. McDonald, E. Ostuni, M.N. Liang, P.J.A. Kenis, R.F. Ismagilov, and G.M. Whitesides, "Patterning Cells and Their Environments Using Multiple Laminar Fluid Flows in Capillary Networks". Proceedings of the National Academy of Sciences. 96: p. 5545-5548, 1999.

[80] Takayama, S., E. Ostuni, X. Qian, J.C. McDonald, X. Jiang, P. LeDuc, M.-H. Wu, D.E. Ingber, and G.M. Whitesides, "Topographical Micropatterning of Poly(dimethylsiloxane) Using Laminar Flows of Liquids in Capillaries". Advanced Materials. 13(8): p. 570-574, 2001.

[81] Takayama, S., E. Ostuni, P. LeDuc, K. Naruse, D.E. Ingber, and G.M. Whitesides, "Laminar flows - Subcellular positioning of small molecules". Nature. 411(6841): p. 1016, 2001.

Chapter 2

Microstructuring PLGA Surfaces

This chapter describes the fabrication of microscale features in the surfaces of the biodegradable polyester PLGA 85:15. Generally, the approach involves replica molding from a microfabricated master. The process begins with the fabrication of a master mold using standard photolithographic techniques on a silicon substrate. The silicon master mold is then used to create elastomeric tooling, which is subsequently employed in the replica molding of PLGA 85:15 biodegradable polymer. PLGA is typically processed using one of two general methods: 1) solvent casting or 2) melt processing. In this chapter, both methods are explored, and the relative advantages are discussed. Melt processing is ultimately selected for use in the remainder of the thesis because of its many advantages related to processing time, reproducibility, and preservation of microstructure. After detailing both fabrication methods, melt processing is explored in more detail. Process versatility and flexibility are demonstrated by fabricating a range of surface microstructures including complex networks of microchannels and high-resolution microstructures. Results suggest that feature resolution is limited by the silicon master mold microfabrication and not the compression molding process, yielding a high-resolution reproducible method for defining micron to centimeter sized surface features while maintaining micron resolution and submicron precision, all in biodegradable PLGA films.

2.1 Master Mold and Tooling Fabrication

2.1.1 Photomask Fabrication

Photomask designs are generated using a computer-aided design layout tool, Catapult – MEMCAD (Coventor). Design files are converted from CIF file format (exported from Catapult) to Postscript format using the file format conversion tool, LinkCAD (Bay Technology). Files are then printed on mylar transparency film using a 5080dpi Linotronic printer (Pageworks) with a practical minimum feature size of ~25μm. The mylar films are cut and secured to blank quartz plates for use as photolithography masks. Alternatively, when high-resolution features with critical dimensions < 25μm are required, chrome photolithography masks (Alignwrite) are used.

2.1.2 Silicon Master Mold Fabrication

Master molds are fabricated using traditional photolithographic processes and standard silicon etch technologies [1]. First, 4" silicon wafers (500+/-25μm thickness) are cleaned in 3:1 H_2SO_4:H_2O_2 for 20 minutes. Then, standard photolithography is performed using the mylar photomask. Throughout this thesis, four different mold fabrication processes are used, depending on the desired feature resolution, height, and cross-section: 1) novolak photoresist [1], 2) thick SU-8 high aspect ratio negative photoresist [2], 3) isotropic etching of silicon [3], or 4) deep trench reactive ion etching [4] (details in Appendix A).

The first two methods are additive processes in which photoresist structures are built on the surface of the silicon. Novolak photoresist spin coated to thicknesses of 0.1-1μm, and it is capable of resolving the finest features of order 1μm. In contrast, the SU-8 photoresist is a rather versatile photosensitive epoxy that can be used to achieve a wide range of thicknesses. Thicknesses can be varied from 1μm to 1mm by manipulating spin speed, time, and viscosity through the addition of the solvent gammabuterolactone (GBL). The maximum

resolution for SU-8 is ultimately dependent on the desired feature thickness. Features are typically limited to a height to width ratio ranging from 10 to 20.

The subtractive processes are generally based on selective bulk etching of silicon with SF_6 or CF_4 through a thick photoresist mask layer of 4620 photoresist. Depending on the process parameters, the dry silicon etch can be used to achieve a variety of sidewall slopes and curvatures. High aspect ratio microstructures (HARMS) with vertical sidewalls are created using a BOSCH process in an STS Inductively Coupled Plasma (ICP) Deep Reactive Ion Etcher (DRIE). As with the additive SU-8 photosensitive epoxy, the resolution of this process is also dependent on the desired etch depth, and is best specified as a maximum aspect ratio – for DRIE, this ranges from 10-40 depending on the amount of pattern-dependent loading. The four microstructuring methods are compared in Table 2.1 and Figure 2.1, and detailed process descriptions are provided in Appendix A.

Master Mold Fabrication Capabilities

Process		Thickness (μm)	Resolution (μm)	Max Aspect Ratio
Thin Photoresist (Novolak)	Additive	0.1-2	0.1-2.0	--
Thick Photoresist (SU-8 50)	Additive	10-1000	--	10-20
DRIE Silicon Etch (ICP)	Subtractive	0.1-500	--	10-40
Mesa Silicon Etch	Subtractive	0.1-500	--	1

Table 2.1 – Comparison of the silicon master mold fabrication approaches.

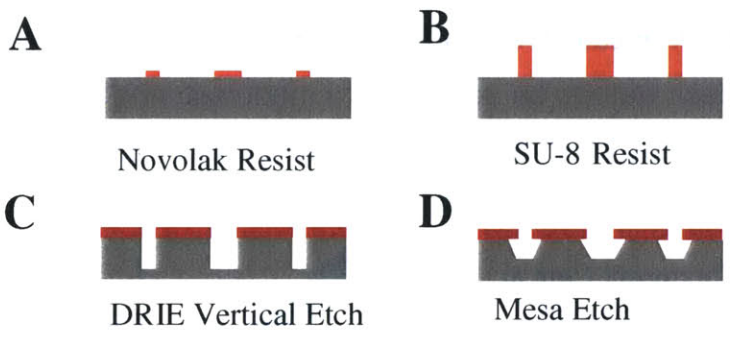

Figure 2.1 – Schematic of the silicon master mold cross-sections. A) Thin Novolak photoresist, B) Thick high-aspect-ratio SU-8 photoresist, C) DRIE silicon etch profile shown with photoresist etchmask, and D) Mesa silicon etch profile shown with photoresist etchmask.

2.1.3 Polymeric Tooling

Replication processes typically involve the formation of robust tooling that can be reused for many molding cycles. The tooling in this thesis was created using rapid prototyping and soft lithographic techniques involving the silicone elastomer Polydimethylsiloxane (PDMS), or Sylgard 184 (Dow Corning) [2]. First, PDMS resin and its corresponding curing agent are combined 10:1, mixed thoroughly, and degassed in a vacuum desiccator to eliminate air bubbles. Next, the silicon master mold is placed in a petri dish, covered with PDMS liquid prepolymer, briefly degassed, and cured in an oven at 80°C for 3 hours. Once cured, the resulting PDMS film can be easily peeled from the silicon with the inverse image of the master mold imprinted in the elastomer surface. There are several advantages to using PDMS as tooling for PLGA compression molding. The PDMS surface is very smooth because it is cast on polished silicon, it is nonadherent to PLGA which aids in release of the molded biodegradable polymer, it is thermally stable (<250°C) [5], and it is not brittle or sensitive to fracture during compression molding. This choice of tooling also has several disadvantages. Although it is virtually incompressible (poisson ratio ~0.49) [6], it is flexible and elastic, making it sensitive to deformation under the applied force of compression molding. In addition, temperature-induced deformation can lead to distortion during compression molding. However, despite these disadvantages, the tooling is ideal for the type of process development described in this thesis. PDMS molds are inexpensive and rapidly produced due to the simple nature of the polymerization, allowing new molds to be created quickly and easily. If this process were to be adapted in a manufacturing setting however, more robust tooling could be fabricated using conventional materials such as electroformed copper or Teflon [7].

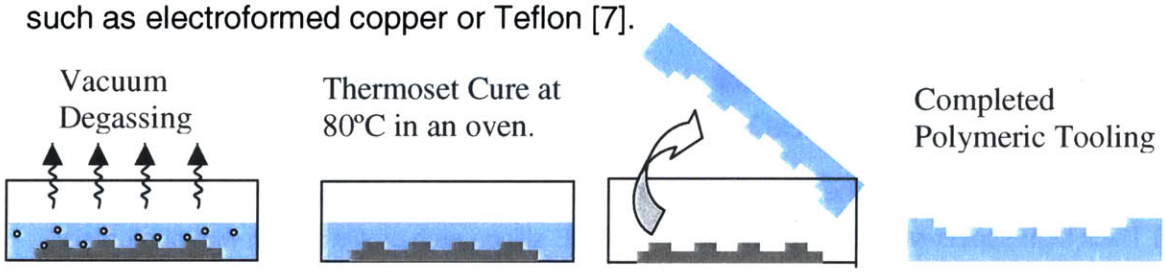

Figure 2.2 – PDMS elastomeric tooling fabrication process

2.2 Biodegradable Polymer Molding

Solvent casting and melt processing are two general approaches to processing the PLGA biodegradable thermoplastic. Solvent casting is the more common scaffold fabrication approach, and the processes are well established. On the other hand, melt processing is relatively less common, and therefore requires some basic characterization. In this section, solvent casting and melt processing are adapted to the microfabricated PDMS tooling and the quality of the resulting films are compared. Then, because melt processing is less common and the PLGA micropatterning method of choice in subsequent chapters, it is explored in greater detail.

2.2.1 Solvent Casting

PLGA is readily dissolved in many organic solvents. Unfortunately, many of these solvents also swell the PDMS elastomeric tooling. In this thesis, acetone is used for solvent casting rather than the more commonly used methylene chloride or chloroform, as it dissolves PLGA without causing dramatic swelling of the PDMS mold. First, Medisorb PLGA 85:15 polymer pellets (see Appendix B for material details) (Alkermes) are dissolved in acetone to form polymer solutions from 5% to 10% (weight/volume). After several hours, the polymer is fully dissolved and ready for casting. The PDMS tooling is then placed in a nonstick weighboat and coated with the polymer solution. Alternatively, the casting is performed at reduced temperatures in a refrigerator or freezer to slow the surface evaporation process relative to the bulk solvent diffusion. When evaporation exceeds the bulk movement of solvent, a skin forms at the polymer solution/air interface, impeding further solvent removal. Pockets of solvent vapor then cause surface blebbing and bubbles, leading to uncontrollable and nonuniform films that adversely effect subsequent bonding processes. At lower temperatures, the solvent evaporation occurs more slowly, allowing vapor that would otherwise be trapped in a bubble to escape, yielding films with no defects. While the method leads to reproducible films with no

surface defects, fabrication requires several days before films achieve sufficient mechanical integrity to be peeled from the mold.

Another solvent casting approach involves casting on the PDMS mold at a temperature high enough to evaporate solvent (>60°C). The polymer solution is poured on the heated mold and gently and continuously stirred to liberate bubbles and prevent skin formation. Once the polymer begins to precipitate, the stirring is stopped. After stirring, a PDMS cover can be placed on the mold to slow further evaporation, planarize the film, and compress the film with applied force if necessary. Several coats can be applied to yield thicker films. These methods result in thin films that can be dried to an arbitrary extent depending on the time and temperature, and the process is considerably faster than passive solvent evaporation in a refrigerator.

Unfortunately, as a general rule, solvent casting methods yield films that continue to shrink after removal from the mold due to solvent evaporation. Because there is a small percentage of polymer weight compared to solvent, the films are very thin and often show evidence of stretching. As the films are dried they tend to curl and fold unless sufficiently thick. Surface microstructures are significantly distorted in many cases, and while small areas can be molded with ease, large surface areas (>3cm diameter) are difficult to pattern without severe distortion from film shrinkage. The methods do have the advantage of yielding very thin (~10μm) flexible films, but the flexibility is due to residual solvent, and there is some concern that residual solvents can adversely effect cell attachment and growth on the biomaterial. Therefore, while solvent casting was demonstrated to be feasible, the more robust and reliable melt processing approach was pursued. The development of melt processing is described next.

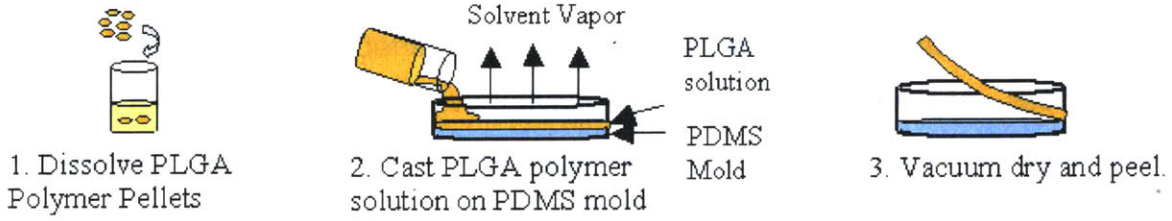

Figure 2.3 Schematic of solvent casting process.

2.2.2 Melt Processing and Compression Molding

Melt processing of PLGA consists of heating the polymer to a viscous melt such that it can be readily formed and molded. In this thesis, the melt processing consists of compression molding the viscous polymer melt between two semi-rigid parallel plates to controllably yield thin films of 50-1000μm. First, the micropatterned PDMS mold is placed flat on a hotplate at 110-160°C and allowed to reach a steady-state temperature. PLGA 85:15 polymer pellets are used to cover the entire PDMS micropattern. A second unpatterned PDMS film is placed on top of the pellets to provide a flat nonadherent surface, and a rigid metal plate is placed on the top PDMS to complete the stack. Reflow of the heated pellets typically requires only a few minutes. Once the viscous melt is formed, force is applied. In this work, quantitative force was applied in a controlled fashion using an Instron mechanical tester in manual mode such that the load could be recorded. Controlled forces ranging from 100-500lbs are applied for 2-10 minutes to achieve complete coverage of the PDMS microstructures. When the process is finished, the load is removed, and the stack is placed on a cooling block until it reaches room temperature. Once the PLGA is below its glass transition temperature (~50°C) and in a brittle state, the stack can be disassembled and the PDMS layer can be peeled from the PLGA film without distorting the surface microstructures. Because the PLGA films are brittle, they cannot be peeled from the mold. Instead the mold must be peeled from the PLGA film. This highlights another advantage of using the PDMS tooling rather than a rigid mold, such as the microfabricated silicon itself. Once fabricated, the microstructured PLGA films are placed in a nonadherent weighboat and covered to prevent electrostatically attracted particulates from contaminating the surface and interfering with subsequent bonding processes.

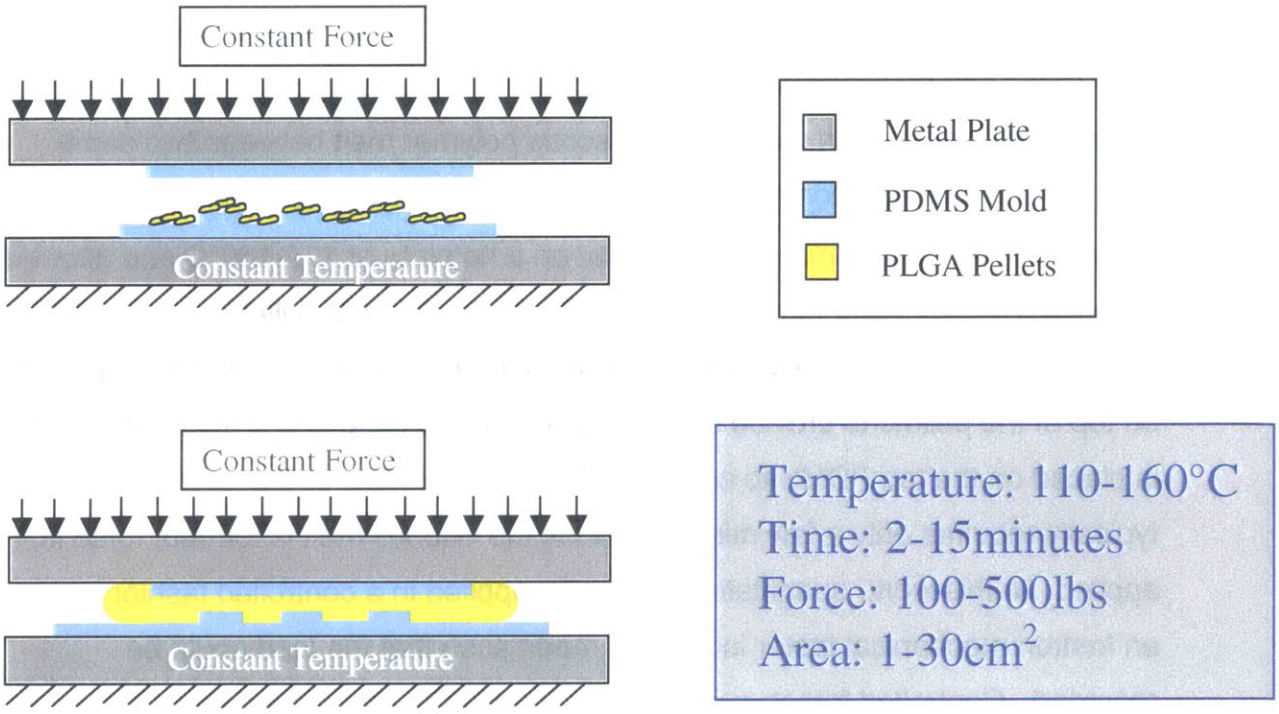

Figure 2.4 Melt processing compression molding schematic.

Figure 2.5 Melt processing apparatus – Hotplate for temperature control, Instron for application of controlled force, polymer pellets-PDMS-rigid plate stack for compression molding.

Compression Molding Theory

If the PLGA microstructures are small compared to the film thickness, the compression micromolding process can be idealized as radial viscous squeeze flow between two flat parallel cylindrical plates. When performed under constant applied force with time-varying plate separation, the squeezing flow can be described by the Stefan Equation [8].

$$H(t) = \left[\frac{1}{H_0^2} + \frac{4Ft}{3\pi\eta(T)R^4} \right]^{-1/2} \tag{2.1}$$

Initial Polymer Melt Height – H_0

One layer of polymer pellets is typically applied to the surface so that the initial polymer melt thickness is fairly constant and approximately 1mm.

Radius – R

The radius is fixed by the mask design. It is therefore not a useful experimental control variable, leaving only temperature, force, and time to control the compression molding process.

Temperature – T and Viscosity – $\eta(T)$

Reasonable processing temperatures were identified using two criteria. The temperature should be low enough to minimize the thermal degradation rate, and it should be high enough for the melt to flow well during compression molding. The degradation rate was determined at several temperatures using Thermal Gravimetric Analysis (TGA), which measures the weight of a polymer sample during a controlled thermal treatment [9]. Any mass loss is interpreted as thermal degradation. First a controlled temperature ramp was performed to identify temperatures at which abrupt changes in degradation rate occur. Then, 30 minute isothermal TGA was performed at three potential compression molding temperatures, 110°C, 140°C, and 170°C. The rate of degradation was

determined from the constant slope of mass loss versus time. Substantial polymer mass loss was not observed for temperatures less than 300°C.

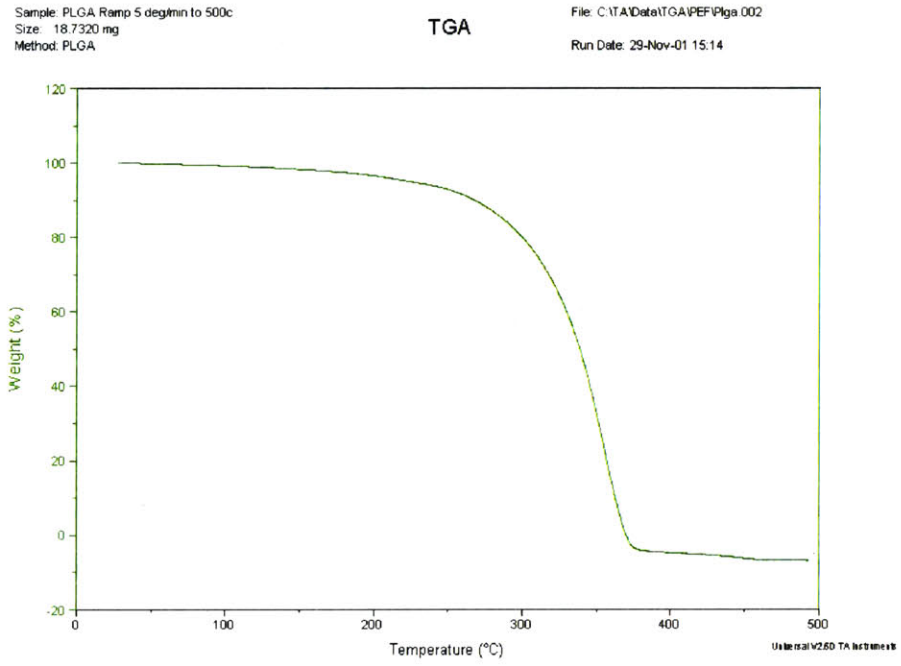

Figure 2.6 Thermal gravimetric analysis (TGA) of PLGA 85:15 using a 5°C/min ramp rate.

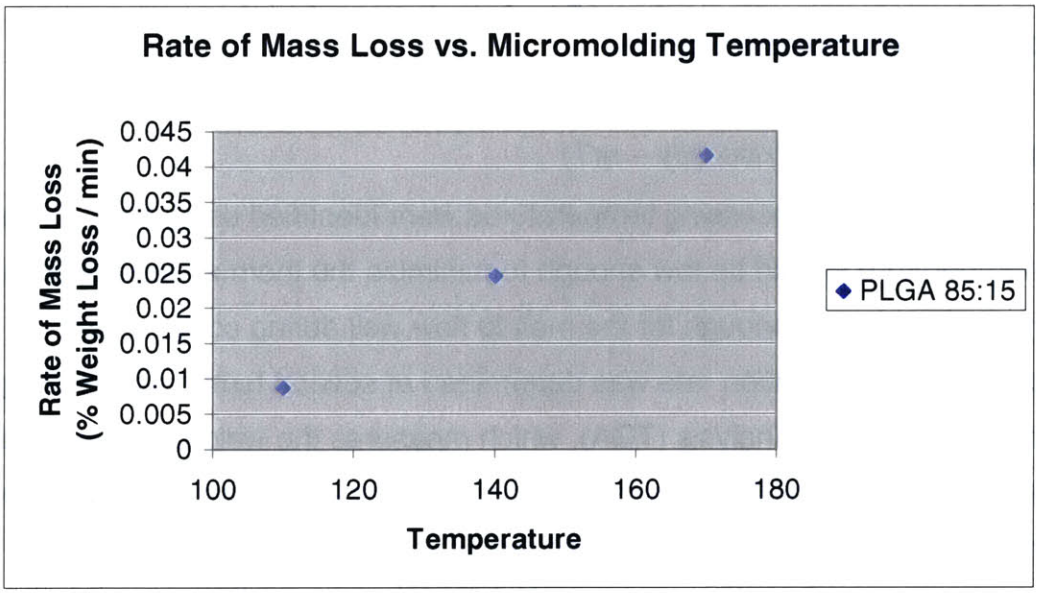

Figure 2.7 Isothermal TGA of PLGA 85:15 simulating isothermal compression molding. The rate of percent weight loss is shown at three potential compression molding temperatures 110°C, 140°C, and 170°C.

Below 110°C, the melt was too viscous to flow appreciably. This was taken as the lower limit of viscosity, as it would limit the ability of the polymer to conform to the micropatterned surface after reasonable processing times. Since the polymer melt viscosity is a key determinant of the time required for compression, the melt viscosity was measured at two temperatures by special request at the polymer vendor, Alkermes. The melt rheology data for two temperatures, 130°C and 150°C, is shown in Figure 2-8.

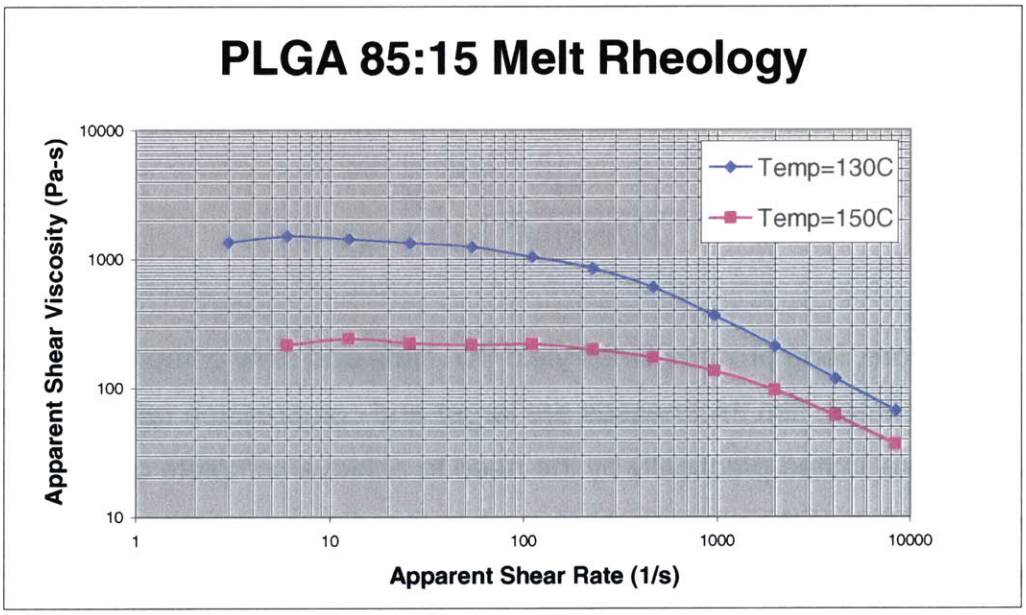

Figure 2.8 PLGA melt viscosity at two compression molding temperatures.

Force

Applied force can be used to reduce the processing time. However, there are limitations. If too little force is applied, the molding requires excessive processing times and the melt might not cover the entire pattern, leading to poor pattern translation. However, if too much force is used, the mold can deform, and in extreme cases, crack. In this work, samples are 1-30cm^2, and the applied force ranges from 100-500lbs using a load cell mounted on an Instron mechanical tester.

Time

Process time is the final variable used to control film thickness. After an initial startup time, the following assumption can be made.

$$\frac{1}{H_0^2} << \frac{4Ft}{3\pi\eta(T)R^4} \tag{2.2}$$

When this is valid, the compression rate is given by

$$\frac{dH(t)}{dt} \cong -\frac{1}{2}\left[\frac{4F}{3\pi\eta(T)R^4}\right]^{-1/2} t^{-3/2} \tag{2.3}$$

Therefore, long process times yield thin films and slow compression rates, while at short times, film thicknesses are larger and compression rates are faster. Short times are limited practically by the need to achieve complete coverage and conformal coating of the microstructures, while long times are limited by the thermal degradation of the polymer. Typical processing conditions (Table 2.2) were used to mold several films and example thicknesses are shown as a function of time for comparison with the corresponding theoretical curve (Figure 2.9). As expected, the agreement between experiment and theory improves as compression time increases and startup effects become negligible.

Several nonidealities are responsible for differences between theory and experiment, with their combined effects generally leading to thicker films than would be predicted from the idealized theory. First, the pellets might not be fully melted or isothermal at time zero, causing actual polymer melt flow to begin later than expected. The melt is not perfectly cylindrical, and the force might not be applied directly at the center of the melt, both leading to non-radial components of flow, which are not considered in the theoretical expression. Finally, because the hydrostatic pressure driving the flow can deform the elastomeric mold and this pressure decreases radially, the plates are not truly rigid or parallel and

radial variation in film thickness is expected. The most significant deformation occurs at the center where the hydrostatic pressure is greatest, and this yields biodegradable films with the greatest thickness at the center.

Molding Processing Parameters	
Force	100 lbs
Temperature	130°C
Viscosity (at 130°C)	15 kPa-s
Radius	3 cm
Initial Height	1 mm

Table 2.2 PLGA 85:15 compression molding process parameters.

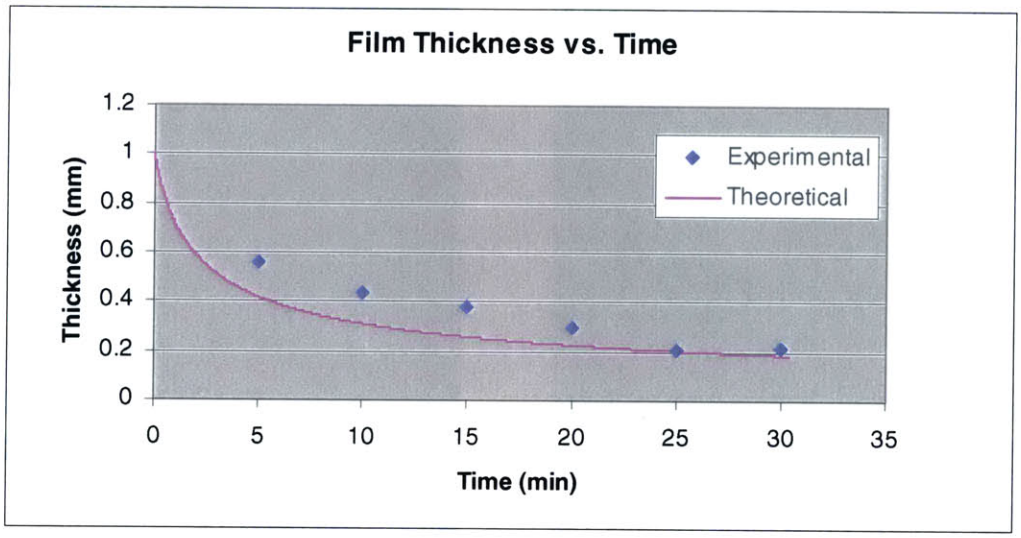

Figure 2.9 Example of constant force compression molding – film thickness versus time – comparison of theory and experiment.

2.3 Microstructure Characterization

2.3.1 Complex Channel Networks

Light Microscopy

Light microscopy is used to dimension features in a top-down manner, assess defects during and after processing, and inspect the patterned surfaces over a wide area. The silicon, PDMS, and PLGA have identical geometries in the case of melt processing, while solvent cast films show some smoothing of local surface topology, such as edges and corners, but preserve the larger features.

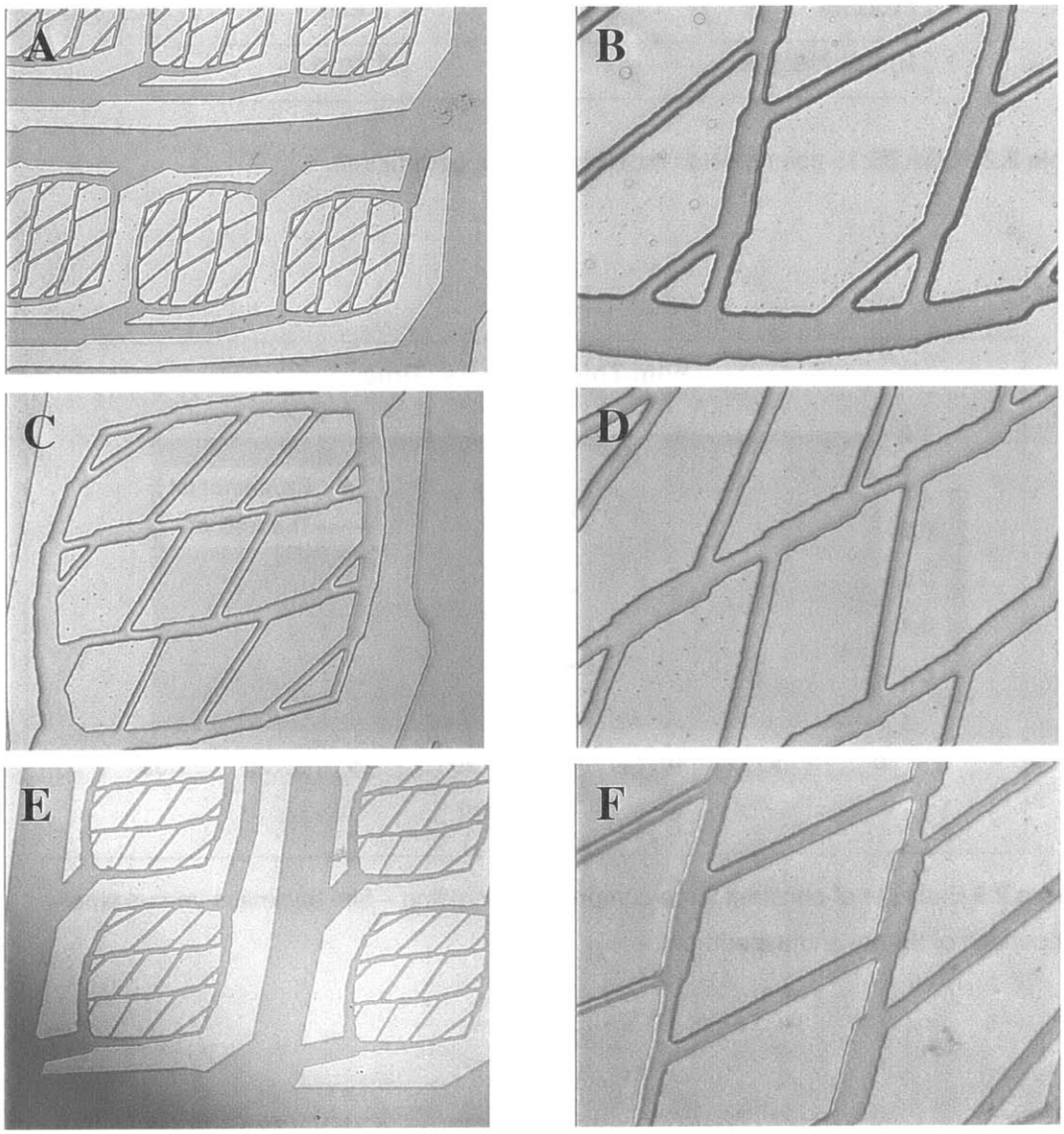

Figure 2.10 Light microscope images of complex channel networks. A-B) Silicon master mold, C-D) PDMS flexible tooling, and E-F) melt molded biodegradable PLGA.

Scanning Electron Microscopy

Scanning electron microscopy (SEM) was performed to inspect the surface of the patterned PLGA surface. Films were sputter coated with 200Å of gold and inspected in an environmental SEM.

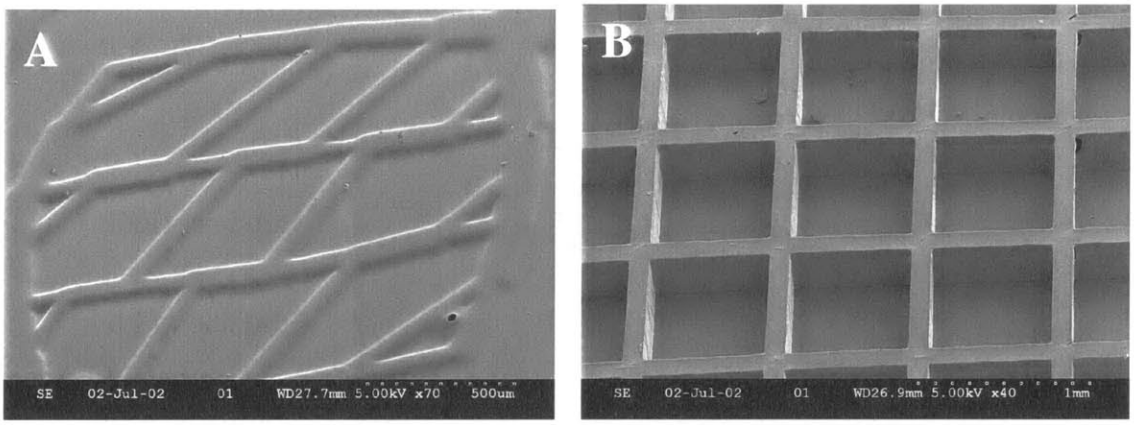

Figure 2.11 A) Solvent cast network of raised lines with slight smoothing of features. Small solvent vapor pockets and a hole (lower right) are evident. B) Solvent cast 200μm deep wells fully dried under vacuum. Edges are sharp due to very slow drying and complete vacuum drying (2 weeks of total processing time), but small holes for vapor release are still noticeable (sidewalls in upper right.).

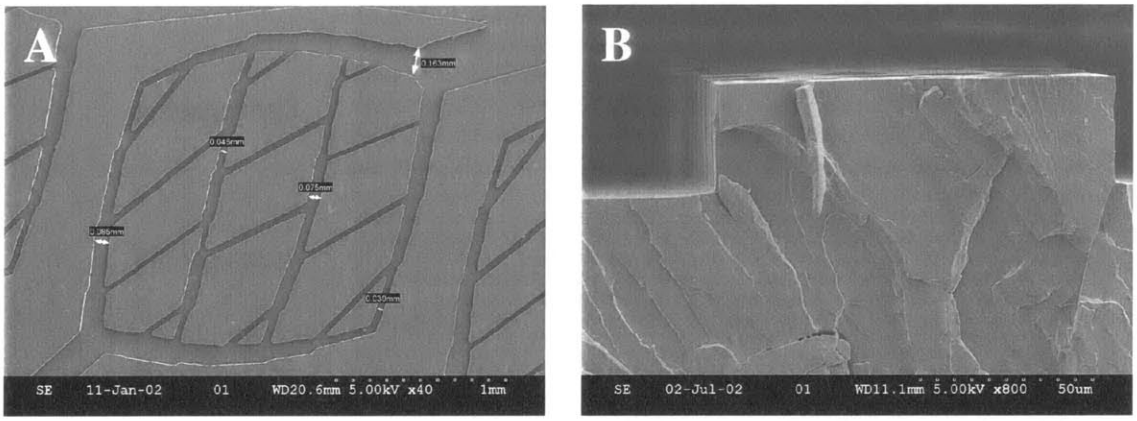

Figure 2.12 A) Melt micromolded complex networks of recessed channels. Films have exceptional reproducibility and any surface defects are found to be the result of particulates and imperfections in the PDMS mold. B) Close-up of melt micromolded structure from a DRIE etched master mold. Notice smooth straight sidewalls and sharp corners at feature edges.

2.3.2 High Resolution Structures

The resolution limits of the micromolding process were explored by fabricating high-resolution features using thin photoresist and casting PDMS directly on the hardbaked photoresist as described in Appendix A. The PDMS mold was used to compression mold features in PLGA using the nominal process of 2 minutes at 140°C with no force to melt the pellets, followed by 5 minutes at 140°C with 300lbs of force.

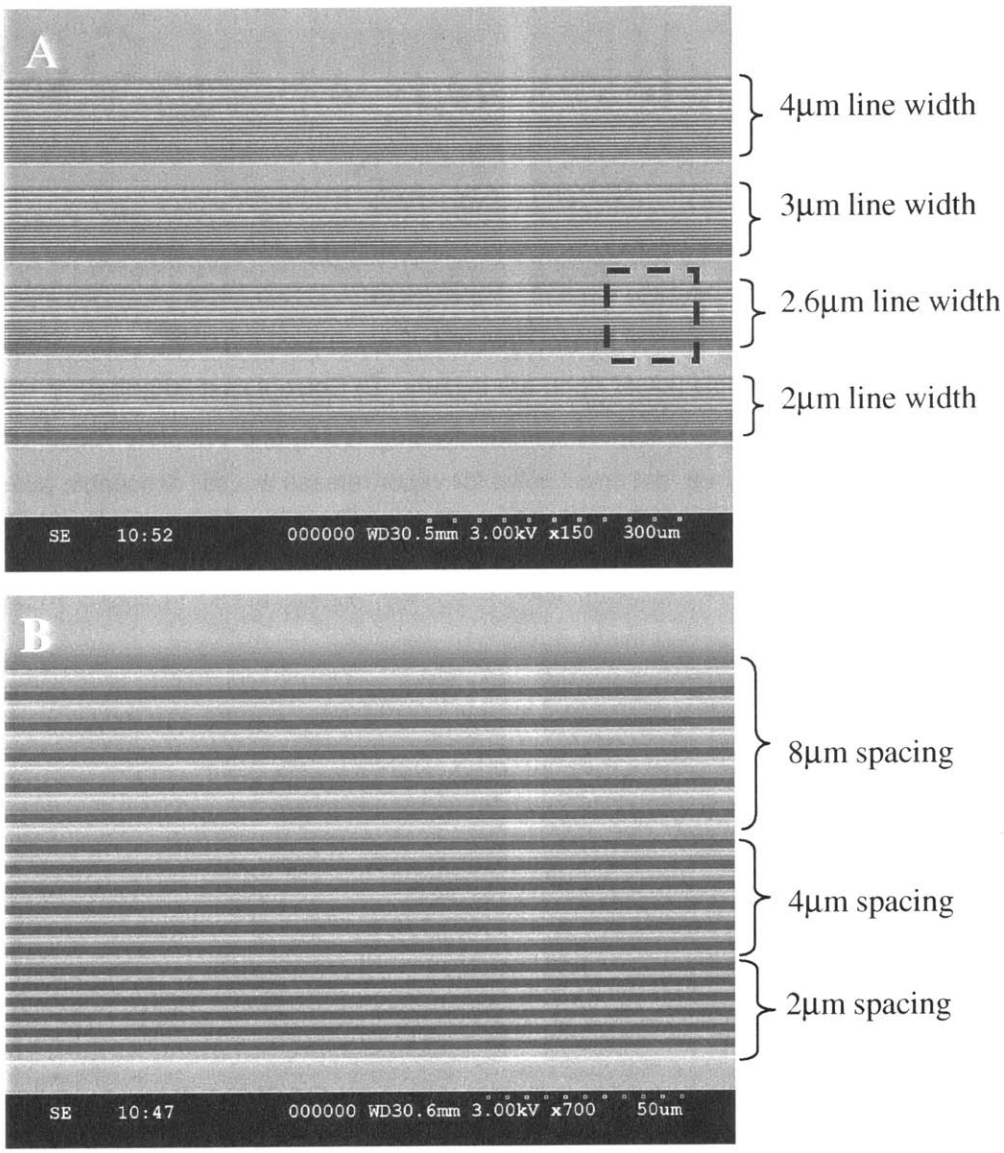

Figure 2.13 SEM of high-resolution features in PLGA. A) Straight lines of varying line widths but same spacing pattern. B) Close-up of 2.6um line width region (outlined in Figure A) showing the spacing pattern.

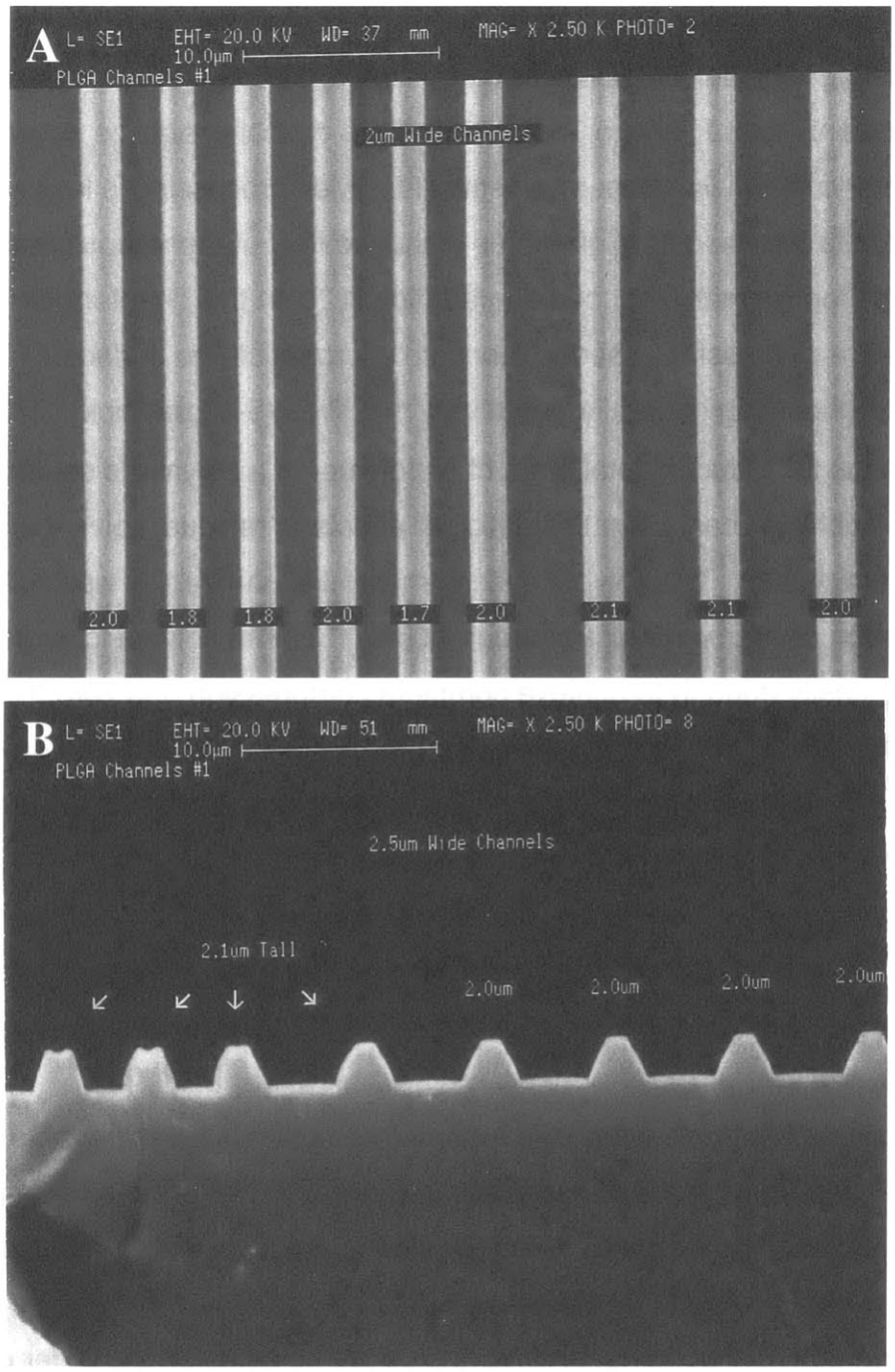

Figure 2.14 SEM of cross-sections of high-resolution features in PLGA. A) 2µm wide lines with 2µm spacing (left) and 4µm spacing (right). Variations are from drawn dimensions are due to photoresist process. B) Raised 2.6µm (drawn) lines with 2µm spacing (left) and 4µm spacing (right).

2.4 Discussion

The most common method for fabricating biodegradable scaffolds is solvent casting [10], but it is consistently criticized for leaving potentially cytotoxic residual solvents in the polymer, and the process typically requires several days of vacuum drying to fully remove solvents [11]. Melt processing is less common, perhaps due to the need for high forces to induce flow of the viscous melt, and the potential for thermally-induced degradation [12]. In this chapter both methods were successfully used to fabricate microstructured surfaces.

Solvent casting generally yields very thin films (5-50μm thick). This is advantageous for reducing total amount of polymer in a polymeric scaffold. The films are flexible, primarily due to plasticizer effects of residual solvent and not simply film thickness. The solvent casting method is particularly well suited for the fabrication of microstructured though-holes [13]. The solvent lowers the polymer viscosity enough to achieve complete compression and zero thickness over the microstructures, without requiring excessive time or applied force. However, solvent casting does have several drawbacks. Large areas are difficult to define without shrinkage-induced distortion of surface microstructures. To pattern larger areas, several coats of polymer are used, and long processing times are required to fully dry samples before mold removal. Recently published attempts to microfabricate PLGA using similar techniques have shown similar results [13, 14].

In contrast to those who have exclusively explored biodegradable micropatterning using solvent casting approaches [13-16], this thesis emphasizes the benefits of melt processing. Melt processing yields excellent microfabricated films over a wide area with well-preserved microstructure, sharp corners that facilitate reproducible bonding, and rapid processing times on the order of minutes. In addition, it can be extended such that both sides of a film can be micropatterned using microstructured PDMS on both plates during molding. The process does not require subsequent drying and is not sensitive to bubbles or shrinkage like solvent casting. It is exceptionally reproducible, and single PDMS molds have been reused indefinitely without breaking. Processing can be

performed in parallel, with several samples being molded at once, making it readily adapted to mass production. In addition, once the silicon master is made, the method requires no expensive equipment, only PDMS silicone elastomer, a hotplate, rigid plates, and weights for applied force.

The drawbacks of compression molding are related to thickness. Thickness control is reasonable, and can be improved by selecting an optimal tooling material. However, at present, there is considerable thickness variation across molded films as a result of the nonidealities in the melt compression process. Using the current process, the thickness variation across the 4cm diameter sample can be as much as 100-200μm at short times between 2-10min, falling to approximately 25-50μm for times of 10 to 30 minutes . Another drawback is that the films fabricated in this work are quite thick (hundreds of microns). This is largely due to the use of PDMS as a mold. It cannot withstand substantially higher temperatures or higher forces without cracking. The more desirable mold would allow higher forces and temperatures enabling faster compression rates and very thin films. Judging from the small weight loss rate at the temperatures up to 170°C, it is reasonable to believe that higher temperatures can be used without causing significant polymer degradation and mass loss. However, it should be noted that the thermal gravimetric method used to assess degradation does not detect chain scission, the reduction in average chain molecular weight without associated mass loss [17]. This would require characterization by gel chromatography. Using a sparse arrangement of pellets dramatically reduces the effective radius of the cylindrical compression molding process and films as thin as 50-80μm (2-3cm diameter) have been fabricated. At these thicknesses, films remain sturdy and it is expected that they could be made substantially thinner without loss of structural integrity.

2.5 Conclusion

In this chapter, silicon micromachining and microfabrication were used to define micron scale features in silicon. The patterns were then translated into

durable flexible films using soft lithographic replica molding and used for compression molding films of the biodegradable polymer PLGA 85:15. The materials and methods are inexpensive and readily adapted because no specialized equipment is required. In addition, films completely retain the resolution and precision of their photolithographically patterned silicon masters over large areas. In summary, the reproducibility, speed, and flexibility of melt processing on microfabricated molds represents a dramatic improvement over previously presented solvent casting techniques, making it ideal for use in the development of more complex high resolution structures such as the biodegradable microfluidics presented in Chapter 4.

2.6 References

[1] Wolf, S. and R.N. Tauber, *Silicon Processing for the VLSI Era Volume 1: Process Technology*. Sunset Beach, CA: Lattice Press, 1986.

[2] Xia, Y. and G.M. Whitesides, "Soft Lithography". Angew. Chem. Int. Ed. 37: p. 550-575, 1998.

[3] Madou, M., *Fundamentals of Microfabrication*. New York: CRC Press, 1997.

[4] Borenstein, J.T., H. Terai, K.R. King, E.J. Weinberg, M.R. Kaazempur-Mofrad, and J.P. Vacanti, "Microfabrication Technology for Vascularized Tissue Engineering". Biomedical Microdevices. 4(3): p. 167-175, 2002.

[5] Xu, B., F. Arias, and G.M. Whitesides, "Making Honeycomb Microcomposites by Soft Lithography". Advanced Materials. 11(6): p. 492-495, 1999.

[6] Armani, D.K. and C. Liu. "Re-configurable Fluid Circuits by PDMS Elastomer Micromachining". in *12th International Conference on MEMS*. 1999. Orlando, FL.

[7] Lee, G.-B., S.-H. Chen, G.-R. Huang, W.-C. Sung, and Y.-H. Lin, "Microfabricated Plastic Chips by Hot Embossing Methods and their Applications for DNA Separation and Detection". Sensors and Actuators B. 75: p. 142-148, 2001.

[8] Denn, M.M., *Process Fluid Mechanics*. Englewood Cliffs, NJ: Prentice-Hall, 1980.

[9] Turi, E.A., *Thermal Characterization of Polymeric Materials*. San Diego: Academic Press, 1997.

[10] Yang, S., K.-f. Leong, Z. Du, and C.-k. Chua, "The Design of Scaffolds for Use in Tissue Engineering. Part I. Traditional Factors". Tissue Engineering. 7(6): p. 679-689, 2001.

[11] Mikos, A.G. and J.S. Temenoff, "Formation of Highly Porous Biodegradable Scaffolds for Tissue Engineering". Electronic Journal of Biotechnology. 3(2), 2000.
[12] Widmer, M.S., P.K. Gupta, L. Lu, R.K. Meszlenyi, G.R.D. Evans, K. Brandt, T. Savel, A. Gurlek, C.W.J. Patrick, and A.G. Mikos, "Manufacture of Porous Biodegradable Polymer Conduits by an Extrusion Process for Guided Tissue Regeneration". Biomaterials. 19: p. 1945-1955, 1998.
[13] Vozzi, G., C.J. Flaim, F. Bianchi, A. Ahluwalia, and S.N. Bhatia, "Microfabricated PLGA Scaffolds: a comparative study for application to tissue engineering". Materials Science and Engineering C. 20: p. 43-47, 2002.
[14] Snyder, J.D. and T.A. Desai, "Microscale Three-dimensional Polymeric Platforms for In Vitro Cell Culture Systems". Journal of Biomaterial Science Polymer Edn. 12(8): p. 921-932, 2001.
[15] Lu, L. and A.G. Mikos, *Modulation of Cell Morphology and Function Using Synthetic Biodegradable Polymers*, in *Bioengineering*. Rice University: Houston, TX, 1999.
[16] Folch, A., S. Mezzour, M. During, O. Hurtado, M. Toner, and R. Muller, "Stacks of Microfabricated Structures as Scaffolds for Cell Culture and Tissue Engineering". Biomedical Microdevices. 2(3): p. 207-214, 2000.
[17] Lu, L., S.J. Peter, M.D. Lyman, H.-L. Lai, S.M. Leite, J.A. Tamada, S. Uyama, J.P. Vacanti, R. Langer, and A.G. Mikos, "In Vitro and In Vivo Degradation of Porous Poly(DL-Lactic-co-Glycolic Acid) Foams". Biomaterials. 21: p. 1837-1845, 2000.

[This page intentionally left blank]

Chapter 3

PLGA FUSION BONDING

The microstructuring techniques presented in the previous chapter employ planar processing, a fundamentally two-dimensional technology. However, biodegradable tissue engineering scaffolds are preferably three-dimensional. Stacking and bonding interconnected films offers a straightforward approach to extending planar techniques to three dimensions. Unfortunately, previously developed PLGA bonding methods involving the use of solvents [1] or intermediate adhesion layers [2] are not compatible with biodegradable microstructures. Commonly used solvent-assist methods that achieve bonding by local dissolution of polymer surfaces cause microstructure distortion, and available adhesion layers are not biodegradable. Therefore, to enable three-dimensional microfabricated devices that are fully biodegradable, a thermal fusion bonding process is developed. This process enables direct bonding of micromolded PLGA 85:15 films in an irreversible fashion using only temperature-induced polymer chain interdiffusion. The result is a monolithic three-dimensional microstructured biodegradable polymer. This chapter presents the newly developed thermal fusion process by first describing the mechanism of fusion bonding, and then characterizing the process parameter space in order to build a simple model for bonding. The goal of the model is to define, in terms of material properties, process control variables, and microstructure and film dimensions, ranges of acceptable times and temperatures for bonding microstructures while avoiding plastic deformation and microchannel collapse. Finally, the process is optimized, and a wide range of channel geometries are bonded and inspected using electron microscopy to evaluate success.

3.1 Thermal Fusion Bonding of Microstructures

Fusion bonding consists of joining thermoplastic components by the application of heat and optionally pressure [3]. This process offers several performance advantages, as the properties of the resulting bond are often indistinguishable from the bulk material, thus raising the theoretical strength of the bond to the level of the bulk. In addition, stress resulting from dissimilar material properties is avoided [4]. For these reasons, the fusion bonding can achieve much higher bond strengths than methods such as adhesive bonding. In addition, it has superior toughness, durability, and repairability. Therefore, thermal fusion bonding is an ideal method for joining the PLGA biodegradable microstructured films.

Fusion bonding of thermoplastics has been extensively studied for the lamination of thermoplastics in the composites industry [5-9]. However, in contrast to the precision structures of microdevices, composite laminations have not focused on preservation of small surface features. Instead, thermoplastic lamination processes are optimized to achieve high throughput in a manufacturing setting by processing at significantly elevated temperatures. Thermal fusion of thermoplastics has successfully been used to bond small features in microfluidic devices for analytical chemistry and "lab-on-a-chip" applications [10-12], however to the author's knowledge, detailed descriptions of the processes such as times, temperatures, and device geometry constraints have not been published.

This chapter describes the development and characterization of a low temperature fusion bonding process intended for stacking and sealing microstructured films of biodegradable PLGA 85:15. Two principle challenges are faced during process design. First, good bond strength must be achieved across the entire area of the device. Second, microstructure distortion resulting from thermally-induced plastic deformation must be avoided. These goals are particularly challenging in light of the small thermal budget set by the low glass transition temperature of PLGA 85:15 (T_g ~ 50°C).

3.2 Thermoplastic Material Properties

3.2.1 The Glass Transition Temperature

PLGA 85:15 is an uncrosslinked amorphous thermoplastic with mechanical properties that are exceptionally sensitive to temperature. Amorphous thermoplastics are high molecular weight randomly entangled polymer chains. In cases where the chains are not chemically cross-linked, it is physical entanglement alone that gives the polymer strength. Materials such as these are characterized by a critical temperature known as the glass transition temperature. Below the glass transition temperature, polymer chains are fixed with respect to each other and the material is glassy. Above the glass transition temperature, short-range chain motion is possible [13]. Corresponding to this molecular description are changes in bulk mechanical properties, or material "softening" [14]. The modulus can drop several orders of magnitude between T_g-20°C and T_g+20°C (Figure 3.1). As the temperature is increased further, intermolecular forces are overcome and polymer chains begin to move freely with respect to each other, as in a fluid. This allows the thermoplastic to be reversibly heated, formed, and then re-solidified by cooling – theoretically, without a change in physical or chemical properties. The compression micromolding process described in Chapter 2 is an example of such forming.

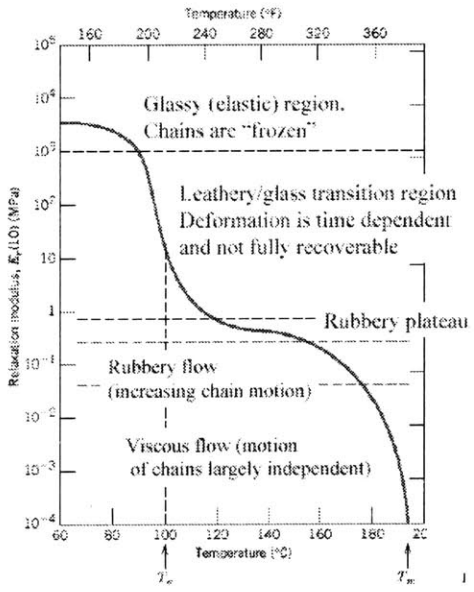

Figure 3.1 – Elastic modulus temperature dependence of a typical thermoplastic [15].

3.2.2 Determination of Glass Transition

Since the glass transition temperature governs both the success of bonding and the potential for microstructure deformation, it was determined experimentally using differential scanning calorimetry (DSC). DSC is a widely used technique for characterizing the glass transition of thermoplastics. Briefly, a sample of polymer is placed in one of two identical small chambers, each with a platinum-resistance thermistor for measuring the temperature in the chamber (Figure 3.2). The differential power needed to maintain the two chambers at identical temperatures during the heating cycle is measured and indicates the heat flow in or out of the calorimeter [13]. The glass transition temperature can be determined from the resulting thermogram by identifying the second-order transition [14]. The glass transition of PLGA 85:15 was determined to be 50.64°C. The thermogram for PLGA 85:15 is shown in Figure 3.3.

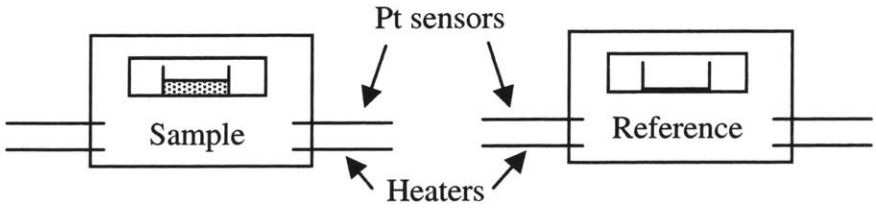

Figure 3.2 – Differential Scanning Calorimetry (DSC) schematic.

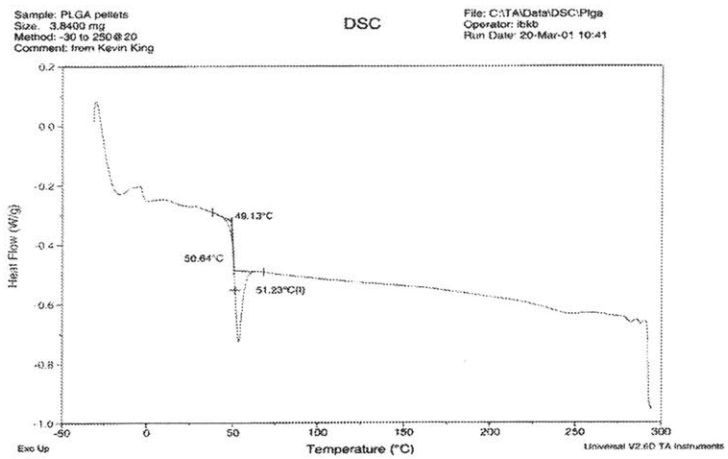

Figure 3.3 – Differential Scanning Calorimetry (DSC) of PLGA 85:15 at 10°C/min ramp rate. The glass transition temperature is estimated at 50.64°C.

3.2.3 Fusion Bonding Near the Glass Transition Temperature

When two pieces of similar polymer are brought into molecular contact at a temperature above their glass transition temperature, the macroscopic interface between the pieces progressively disappears and mechanical strength of the interface increases [16]. This phenomenon, known as polymer-polymer welding or healing, has been widely studied both experimentally and theoretically [17-19].

The healing is primarily due to the diffusion of polymer chains from both pieces of polymer across the interface, and has been described theoretically in 5 stages [20]: 1) surface rearrangement, 2) surface approach, 3) wetting, 4) diffusion, and 5) randomization. In this work, the process is regrouped into two steps, 1) intimate contact (rearrangement, approach, and wetting) and 2) interdiffusion (diffusion and randomization). The goal is to obtain, through experimental investigation of these two steps, an estimate of the total time required to achieve appreciable interfacial bond strength. In the next sections, qualitative observations of wetting and diffusion are described, each followed by a brief experiment to quantify the respective characteristic time scale.

A brief comment should be made about the role of pressure in fusion bonding. Application of mechanical force during bonding is not thought to increase the rate of polymer diffusion across the interface and therefore does not contribute to the development of interfacial bond strength. However, pressure can accelerate the process of bringing surfaces into intimate contact prior to interdiffusion [21]. In this work, no pressure was applied to avoid exerting localized forces that might cause deformation of the microstructures. Instead, samples come into intimate contact simply by falling under their own weight.

3.3 Fusion Bonding Model Overview

Initial experiments bonding simple PLGA channels suggested that microstructures could be successfully bonded while preserving channel patency. However, success was extremely sensitive to the bonding temperature, bonding time, and microstructure dimensions. For each design, it is important that the proper temperatures, times, and pressures be chosen so as to achieve rapid bonding without suffering channel deformation. Therefore a simple model was developed to describe the time course of bonding as a function of temperature.

The process is modeled as two competing parallel processes 1) bonding and 2) deformation, as shown schematically in Figure 3.4. The bonding step consists of two sequential stages, 1a) intimate contact, and 1b) interdiffusion. Intimate contact refers to the elimination of potential barriers associated with inhomogeneities at the surface and the achieving of molecular contact between the two polymer films. Interdiffusion refers to the diffusion of entangled polymer chains across the interface, as well as the disappearance of the polymer interface and the development of associated interfacial bond strength. The competing process, deformation, is an undesirable and parasitic process that describes temperature-induced plastic deformation of microstructures under their own weight, causing potential collapse and occlusion of PLGA microchannels. For purposes of the model, the deformation stage is considered to occur in parallel with both intimate contact and interdiffusion.

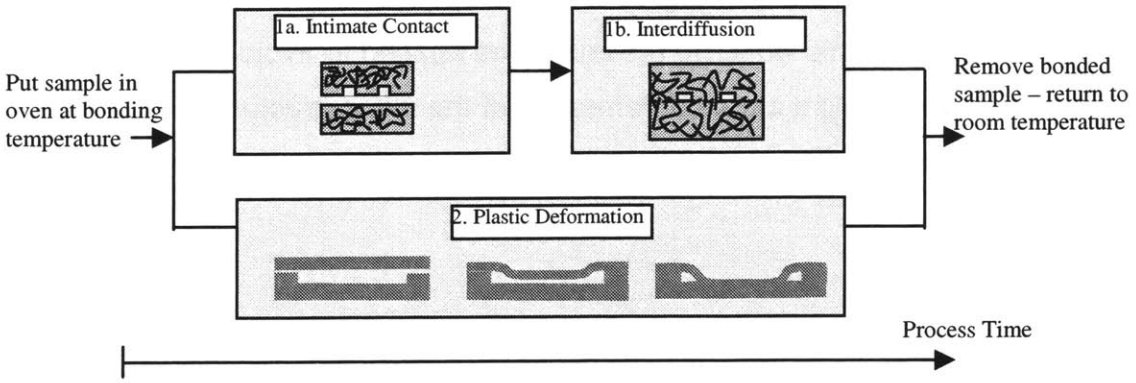

Figure 3.4 – Bonding (top) and deformation (bottom) occur simultaneously during temperature treatment. The goal of the model is to identify conditions that allow completion of bonding before appreciable deformation occurs.

Using this framework, the modeling goal is to identify temperatures and times for which the characteristic time to deformation is sufficiently greater than the characteristic time to reliably complete bonding. A secondary goal is to identify conditions that minimize total bonding time in order to achieve short device fabrication times.

A "bonding process window," Δ, is defined to be the difference between the characteristic time to suffer deformation $\tau_{deformation}$, and the characteristic time to achieve bonding $\tau_{bonding}$ as in Equation 3.1.

$$\Delta = \tau_{deformation} - \tau_{bonding} \tag{3.1}$$

The bonding process window, Δ, will be shown to depend on device dimensions and temperature, and it will be used to guide selection of appropriate bonding times and temperatures in a device-dependent fashion. An upper temperature limit exists where the process window becomes so small Δ_{min} that achieving bonding without deformation is impractical. Similarly, a minimum temperature exists where the bonding process occurs so slowly that manufacturability is significantly compromised $t_{bonding\ max}$ (Figure 3.5). The following process model looks to make an estimate of Δ in terms of process control variables, polymer material properties, and device dimensions, and ultimately make predictions regarding acceptable bonding times for specific microchannels.

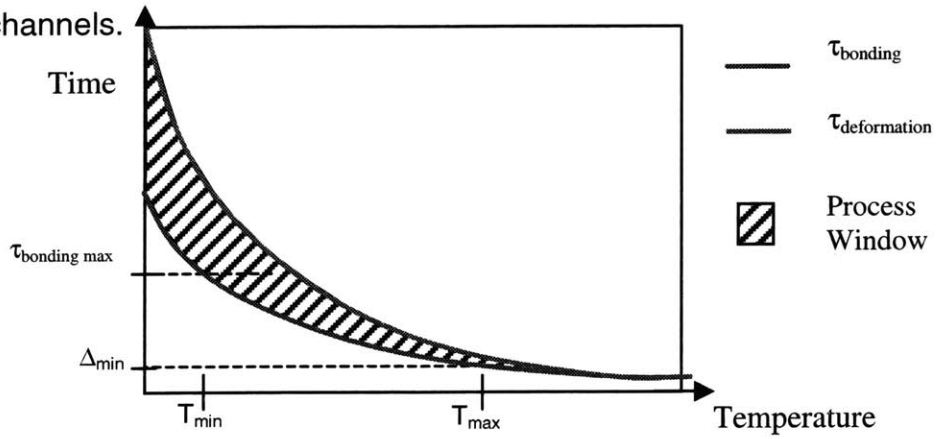

Figure 3.5 – Identification of appropriate bonding times and temperatures.

3.4 Intimate Contact – "Wetting"

3.4.1 Qualitative Observations

Initial observations revealed that when two flat pieces of PLGA 85:15 are placed in contact at temperatures above the glass transition temperature, the surfaces appear to stick or "wet" in random nucleation sites across the interface. The "wetting" is associated with a distinct color change that is observable both macroscopically and microscopically. If the samples are maintained at the elevated temperature, the "wetting" pools appear to grow radially accompanied by new nucleation sites, afterwhich the pools converge and coalesce (Figure 3.6). In addition to the observed color change, the interface develops mechanical strength. The time required for two films to wet is observed to depend on bonding temperature, film thickness, and sample area with temperature being the most important factor. Very slow wetting occurs for films with large areas, large thickness, and at low temperatures near the glass transition T_g+10°C. In contrast, rapid wetting was observed for thin small area samples bonded at temperatures exceeding T_g by 30°C. Despite the macroscopic appearance of bonding, the observed "wetting" does not itself signify the development of interfacial strength, as the films can be separated immediately after wetting. However, a short time after wetting, the interface becomes so strong that samples break in the bulk before breaking at the interface.

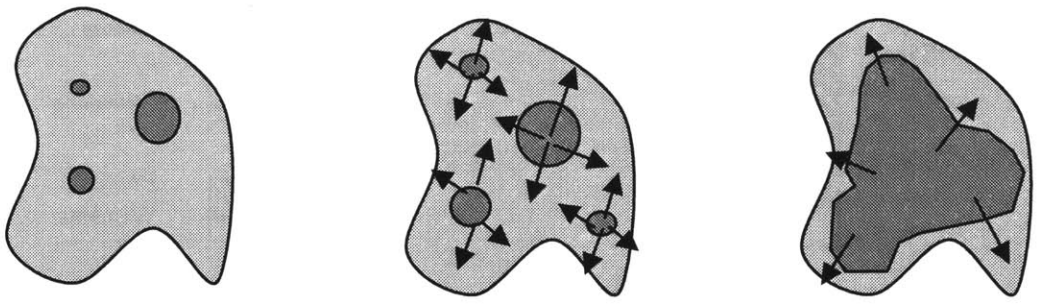

Figure 3.6 Partially wetted domain of a bond interface. Random nucleation sites grow from small pools, and coalesce to completely wet the surface.

3.4.2 Previous Models for Intimate Contact

The term intimate contact describes the development of molecular contact between the two polymer surfaces. Past studies on composites fusion bonding have modeled intimate contact as viscous flow of polymer into micron scale surface aspirites [5, 8, 9]. However, in those studies, the aspirites were the same size as the microstructures that this work is aimed at preserving. Therefore, for purposes of bonding microfabricated films, the surface aspirites or surface roughness is more likely on the nanometer scale, and a different intimate contact description is required.

3.4.3 Experimental Determination of Intimate Contact Time

The time required to achieve intimate contact was determined by a simple experiment. PLGA films of 500μm nominal thickness were patterned with 50μm deep channels varying from 1mm to 4mm wide channels using the compression molding process described in the previous chapter. The films were placed in contact in an oven at the desired temperature and visually inspected at several time points throughout the bonding process. Bonding temperatures ranged from 55°C to 85°C. At several time points, the amount of wetted area was recorded, and a fractional area was calculated by normalizing to the maximum wet area for the sample. The time required to achieve 90% wetting was taken to be the characteristic time, and termed the "time to intimate contact" or $\tau_{contact}$.

3.4.4 Results

Macroscopic images (Figure 3.7) reveal initial contact points, followed by new points of contact, likely due to the polymer falling under its own weight. From each nucleation site extends a traveling increase in wetted area. In the case of surfaces with microchannels, radial wetting is restricted to linear growth due to the channel structure. The wetting rate appears to be driven by capillarity, pulling the films into contact. Where particulates are present, wetting is impeded, creating an unusual wetting progression and delaying the total time to intimate contact.

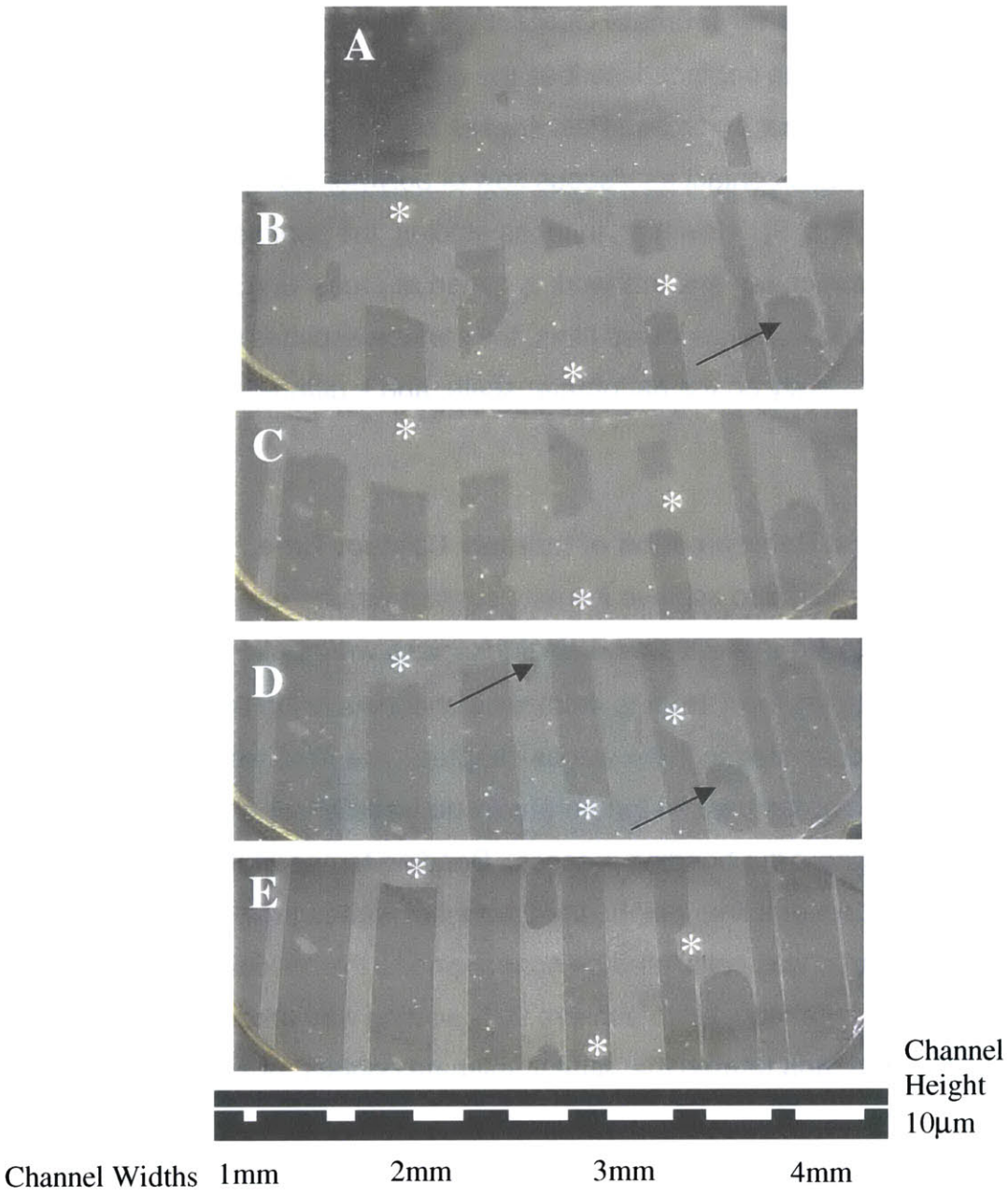

Figure 3.7 Example images showing the time course of intimate contact for a series of parallel channels bonded at 70°C. A) t=5 min, contact is made at point locations at the parimeter of the sample. B) t=10 min, new points of contact are formed and the 4mm channel collapses (arrow). C) t=15 min, nucleation sites grow linearly. D) t=20 min, wetting is nearly complete and several smaller width channels have collapsed (arrows). Particulates that interfere with normal bonding are labeled with asterisks.

The nominal time to achieve 90% wetting is plotted as a function of temperature in Figure 3.8. Wetting time versus inverse absolute temperature is fit with an exponential (R^2 =0.9883) to determine constants of an Arrhenius relation. Equation 3.2 is therefore taken to be an expression for the time to intimate contact in seconds.

$$\tau_{contact}(T) = 1.71\times10^{-19}\exp\left(\frac{15506}{T(K)}\right) \tag{3.2}$$

where $\tau_{contact}$ is the time (seconds) to achieve intimate contact, and T is the bonding temperature (Kelvin).

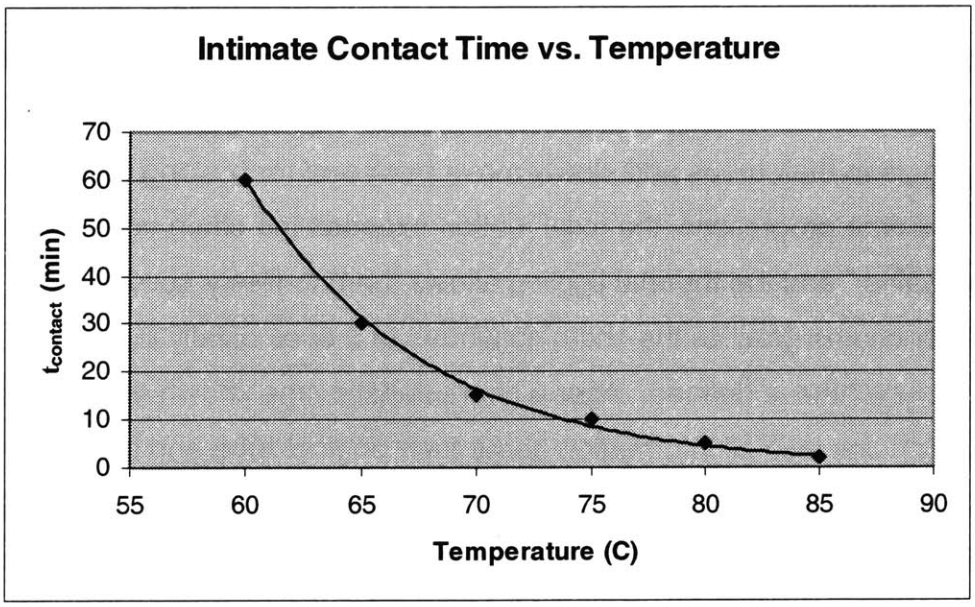

Figure 3.8 Temperature dependence of $\tau_{contact}$. Values represent nominal values for a 500μm thick film falling under its own weight with no additional applied pressure. Note, in contrast to equation 3.2 in the text, time data is plotted in minutes.

3.5 Interdiffusion – "Healing"

3.5.1 Qualitative Observations

During initial experiments, the bond interface was found to develop mechanical strength soon after the two polymer surfaces wet. When samples were cross-sectioned and viewed under light microscope, no interface was observed. This process of fusion bonding two like polymer surfaces is known as "autohesion." In this section, autohesion is described in terms of high molecular weight interdiffusion. This interdiffusion is not simple Fickian diffusion, but is instead due to the high molecular weight linear nature of the polymer chains, and is better described by de Genne's theory of reptation [17, 22, 23].

3.5.2 Reptation and Interdiffusion

Self-diffusion of large chain molecules occurs by a motion termed "reptation," where entangled molecules are conceptualized as existing in tortuous tubes (Figure 3.9A). De Gennes argued that thermal motions cause chains to rapidly jiggle in their tubes and slowly move back and forth along the axis of the tubes. As time progresses, the axial motion exposes the chain ends, termed "minor chains," and the thermal jiggling allows them to freely access other tubes. The minor chains grow as the chain continues to moves axially in the tube, and slowly, a new tube is defined. After a characteristic time known as the reptation time, the chains lose all information about their original tube and have fully interdiffused. When this occurs across an interface, the interface disappears and the strength of the interfacial bond approaches that of the bulk polymer cohesive strength (Figure 3.9B). The characteristic time to achieve the maximum bond strength is therefore on the order of the reptation time, a property of the material and a function of temperature. The reptation time can therefore serve as a measure of the time required to achieve maximal bond strength for the biodegradable microchannels, or τ_{bond}. Unfortunately, because the reptation time for PLGA has not been characterized, and is not easily determined quantitatively, a simple experiment is used to demonstrate that bond strength is achieved at times that are the same order of magnitude as the contact time.

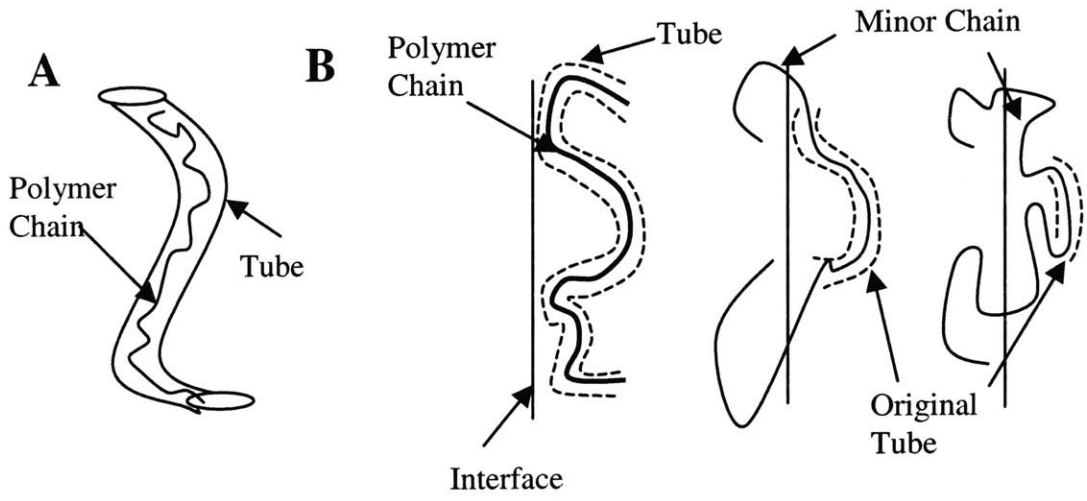

Figure 3.9 A) deGennes' high molecular weight polymer chain residing in a tube and B) Polymer chain self-diffusion leading to loss of original tube, growth of minor chains, and reptation across the interface, resulting in the development of bond strength.

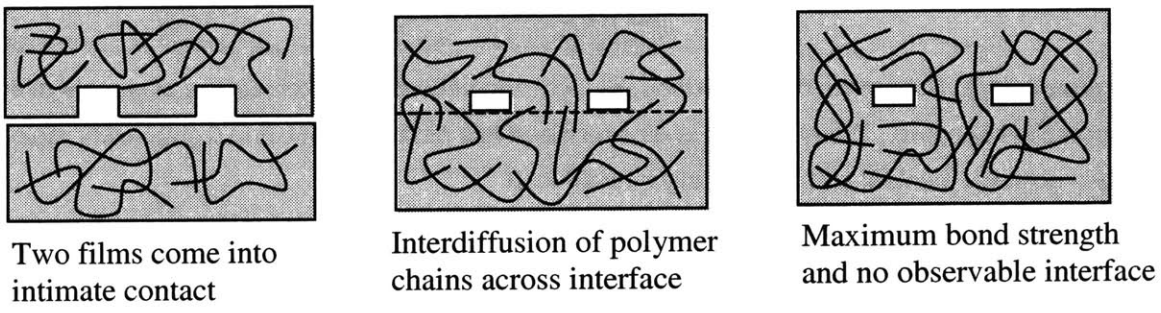

Figure 3.10 Cross-sections of the interdiffusion process for bonding microchannels is depicted schematically. The entanglement of polymer chains across the interface occurs after two polymer films are in intimate molecular contact.

3.5.3 Interdiffusion Time

Films of PLGA with simple patterns were compression molded and isothermally fusion bonded in an oven for various times at several temperatures. Samples were first prepared such that a razor blade could be used to pry the layers apart. A 5-10lbs weight was applied to the surface during bonding to insure that the time to achieve intimate contact was negligible. After bonding, samples were broken with the razor blade as in Figure 3.11A. Samples bonded at small times are easily separated. Bonded for intermediate times, samples can be separated with significant force, but the surfaces show evidence of some interdiffusion (Figure 3.11B). However, for each temperature, there exists times after which the samples break in the bulk before breaking at the interface. This time is taken to be the characteristic time to achieve interfacial strength; although it is unlikely that interdiffusion is entirely complete at this time point. The results are shown in Table 3.1 below, with the important result being that bonding times are similar to the intimate contact time for each temperature.

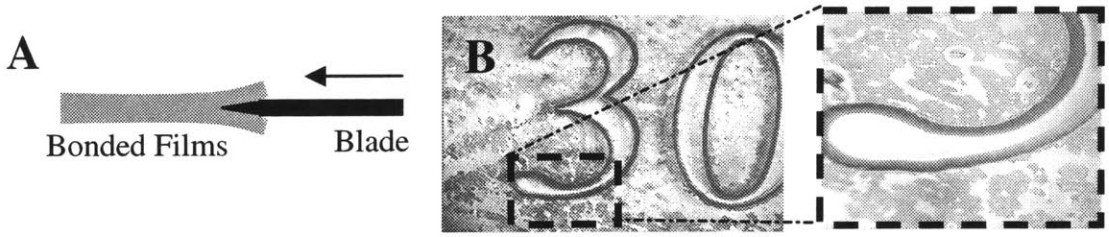

Figure 3.11 A) Schematic of test method. B) Light microscope image of surface of sample after incomplete bonding. The number 3 is recessed and has not begun bonding (light). Dark regions have achieved contact and are partially interdiffused.

Temperature (C)	Not Bonded (min)	Bonded (min)
60	40	60
65	15	35
70	3	20
75	2	10
80	--	5

Table 3.1 Results of bonding test. The largest time resulting in non-bonded samples, and the smallest time resulting in bonded samples are reported.

3.6 Bonding Time

The time required to achieve maximum bond strength is to a first estimate the sum of the time to achieve intimate contact and the time to complete interdiffusion.

$$\tau_{bonding} = \tau_{contact} + \tau_{diffusion} \tag{3.3}$$

The goal is to make a conservative estimate of the bonding time. Therefore, because the time to interdiffusion was found to be equal or smaller than the time required to achieve intimate contact, the two times are taken to be comparable, making the bonding time approximately twice the intimate contact time.

$$\tau_{bonding} \cong 2\tau_{contact} \tag{3.4}$$

Equation 3.2 and 3.4 can then be used to write the following expression for the total time to achieve bonding.

$$\tau_{bonding}(T) = 3.42\times10^{-17} \exp\left(\frac{15506}{T(K)}\right) \tag{3.5}$$

This is particularly appealing because of its simplicity and its practical implications. To the extent that this assumption is valid, the time to achieve bonding is experimentally accessible using inline optical monitoring of the sample surface to measure the time to intimate contact and estimate the time to bonding.

3.7 Plastic Deformation

When high aspect ratio microchannels (large width-to-height ratios) are bonded at temperatures well above the glass transition temperature they rapidly deform and collapse before bonding is complete. The most rapid deformation occurs at the channel center and the direction of channel collapse is always consistant with the force of gravity. Together, this suggests that the microchannel is falling under its own weight. As discussed in Section 3.2, amorphous thermoplastics lose considerable mechanical strength at temperatures above T_g. Since the rate of plastic deformation of PLGA microchannels can limit design flexibility by constraining permissible channel geometries and bonding temperatures, it is important to understand how the characteristic deformation time, $\tau_{deformation}$, depends on the microchannel dimensions and fusion bonding temperature. In this section, the plastic deformation of PLGA 85:15 is investigated by modeling the microchannel ceiling as a simple beam. The viscoelastic response of the PLGA material is determined from simple macroscale experiments, and using the results, predictions are made about the time scale of microscale channel deformation. For purposes of the model, the microchannel ceilings are treated as doubly clamped cantilever beams bending under their own weight. Assuming linear viscoelasticity, the viscoelastic deformation will have the same general shape as the elastic deformation. Therefore, the elastic case is treated first.

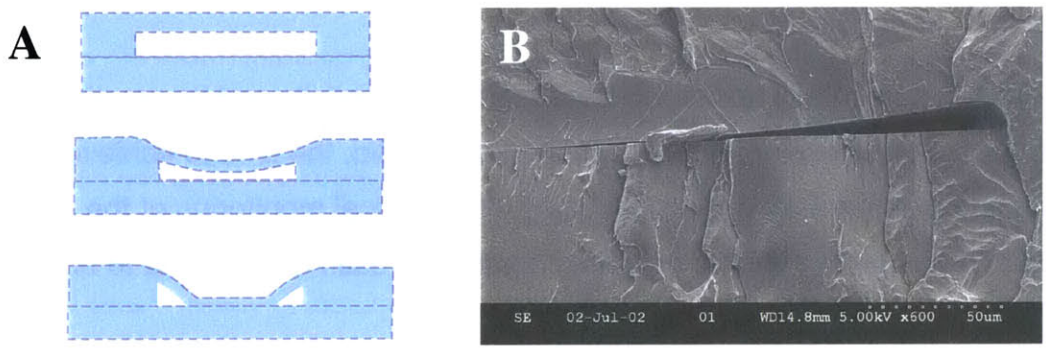

Figure 3.12 A) Schematic of plastic deformation and collapse during thermal fusion bonding of microchannels. B) Channel collapse during bonding at high temperatures (T>80°C) or long times ($t >> \tau_{contact}$).

3.7.1 Elastic Deformation

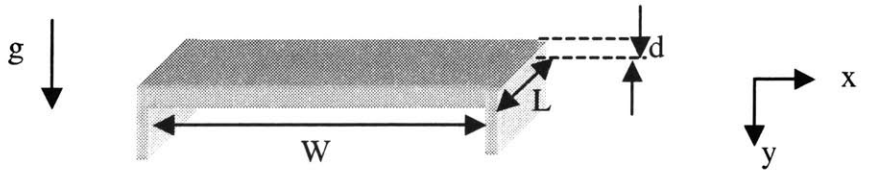

Figure 3.13 Schematic of microchannel ceiling treated as a simple beam.

The bending of a microchannel under its own weight is governed by plate mechanics [24]. For long straight microchannels without axial variation, a one-dimensional beam deflecting under a constant load is sufficient to describe the motion. At room temperature, the thermoplastic beam is almost completely elastic, and for small deflections, the bending of such a beam is governed by the following differential equation,

$$\frac{\partial^4 \delta}{\partial x^4} = \frac{q_0}{EI} \tag{3.6}$$

where q_0 is the constant load (force per length), δ is the deflection in the y direction, E is the elastic modulus, and I is the moment of inertia. Since the load is simply the weight of the beam, it is uniformly distributed across the beam and assumed to be independent of both time and temperature. The load is therefore given by the following expression,

$$q_0 = \rho d L g \tag{3.7}$$

and the moment of inertia by

$$I = \frac{d^3 L}{12} \tag{3.8}$$

where ρ is the material density, d is the beam thickness, g is the acceleration due to gravity, and W is the channel width as shown in Figure 3.13.

Two solutions to the beam equation are used in this chapter: 1) a cantilever, for macroscopic beam experiments (Figure 3.14A), and 2) a doubly clamped beam, as a model of microchannel deformation (Figure 3.14B).

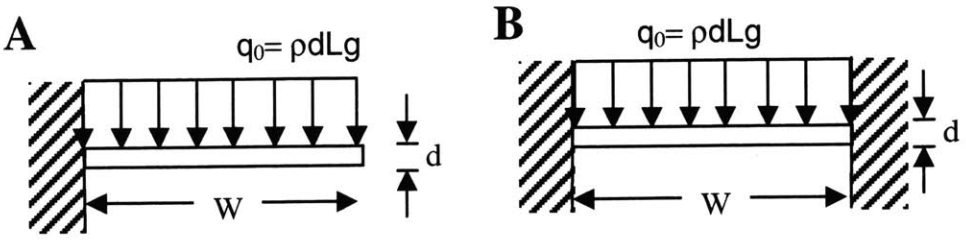

Figure 3.14 Uniformly loaded A) cantilever beam and B) doubly clamped beam.

The boundary conditions assumed for each solution are given below.

Cantilever Beam	Doubly Clamped Beam
δ_1 (0) = 0	δ_2 (0) = 0
δ_1' (0) = 0	δ_2'(0) = 0
δ_1" (W) = 0	δ_2 (W) = 0
δ_1"'(W) = 0	δ_2'(W) = 0

Table 3.2 Typical boundary conditions for cantilever and double clamped beams.

The solutions for the deflection of the cantilever beam $\delta_1(x)$ and the deflection of the doubly clamped beam $\delta_2(x)$ are then determined by solving the differential equation (Equation 3.6) subject to the appropriate boundary conditions (Table 3.2). Solutions are given as Equations 3.9A and 3.9B.

Cantilever Beam
$$\delta_1(x) = \frac{q_0 x^2}{24EI}\left(x^2 - 4Wx + 6W^2\right) \tag{3.9A}$$

Doubly Clamped Beam
$$\delta_2(x) = \frac{q_0 x^2}{24EI}\left(x^2 - 2Wx + W^2\right) \tag{3.9B}$$

3.7.2 Viscoelastic Deformation

Assuming linear viscolelasticity, the deflection of a viscoelastic beam can be expressed in terms of the corresponding elastic deflection [25]. Since the elastic beam deflection is known for the simple beam geometries considered here, the viscoelastic beam deflection can be determined directly, without resolving. This is known as the Correspondence Principle. Important implications of this principle are that the viscoelastic deflection has the same shape (x-dependence) as the elastic deflection, and that the shape is independent of time and temperature. Time and temperature dependencies are characterized by the creep response, or creep compliance, J(t,T), a function of the beam material. The creep response is the strain, here a function of time and temperature, divided by the constant stress of the weight of the beam.

$$J(t,T) = \frac{\varepsilon(t,T)}{\rho g d} \tag{3.10}$$

Therefore, the deflection of the thermoplastic cantilever beams $v_1(x,t,T)$ and the doubly clamped beams $v_2(x,t,T)$ considered here are given by

$$v_1(x,t,T) = \frac{q_0 x^2}{24I}\left(x^2 - 4Wx + 6W^2\right)J(t,T) \tag{3.11A}$$

$$v_2(x,t,T) = \frac{q_0 x^2}{24I}\left(x^2 - 2Wx + W^2\right)J(t,T) \tag{3.11B}$$

where q_0 is the load and J(t,T) is the creep relaxation, a function of the film thickness d, the time t, and the temperature T. The maximum deflection for the cantilever beam occurs at the tip (x=W) while the maximum deflection of the doubly clamped beam occurs at the center (x=W/2).

Cantilever Beam

$$v_1(W,t,T) = \frac{q_0 W^4}{8I} J(t,T) \tag{3.12A}$$

Doubly Clamped Beam

$$v_2\left(\frac{W}{2},t,T\right) = \frac{q_0 W^4}{384I} J(t,T) \tag{3.12B}$$

3.8 Creep Compliance Estimation

3.8.1 Macroscopic Beam Approach

Since the geometry dependence of the creep response is known but the time and temperature dependences are not, it can in theory be determined from a beam of any dimension. Experimentally, it is easier to observe macroscopic deflections than microscopic deflections. Therefore, the creep response is estimated by melt processing macroscopic PLGA 85:15 beams of known geometries, clamping them in an oven at various temperatures, and recording the tip deflection as a function of time. The recorded deflections $v_1(W,t,T)$ can then be used to determine J(t,T) using equation 3.12A.

This equation cannot be fit to experimental data until the form of the creep response is known. It has been observed qualitatively that around the glass transition temperature, plastic deformation is substantial, while the elastic component is comparatively less important, making pure viscous damping a reasonable approximation for the creep response at short times. Therefore, to obtain a conservative estimate of deformation, the creep relaxation is assumed to be linear in time. Viscosity is prescribed an Arrhenius relationship, so the temperature dependence of the creep response is assumed to be exponential in form. This assumption of pure viscous damping is a special case of a Maxwell model for a viscoelastic solid, where the elasticity is zero. Therefore, the beam is modeled as a simple dashpot, with a creep response of the form

$$J(t,T) = \frac{A}{\rho g d} \exp\left(\frac{B}{T(K)}\right)(t) \tag{3.13}$$

where A and B are empirical constants to be determined from macroscopic cantilever beam deformation experiments.

3.8.2 Experimental Method

PLGA 85:15 beams of 1-5 cm x 0.05 cm were compression molded as previously described, clamped at one end, held horizontally in an oven at various temperatures, and allowed to bend and deform under their own weight. The deformation was measured as a function of time using a vertically hanging ruler and a hanging mirror to ensure that the measurements were reproducibly taken normal to the direction of deflection. The experiment was performed at multiple temperatures and the measured times and deflections at each temperature were used to determine the constants in Equation 3.13, the assumed form of the creep response using Equation 3.12A, the deformation of a linearly viscoelastic cantilever beam. The experiment is shown schematically in Figure 3.15.

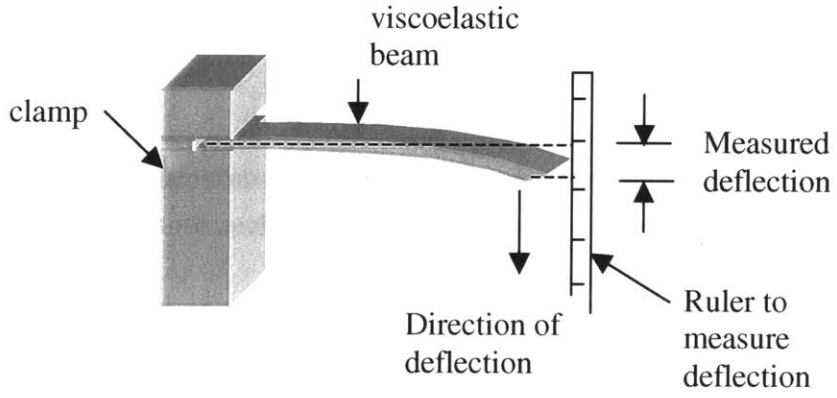

Figure 3.15 Schematic of macroscopic cantilever experimental setup.

3.8.3 Results

The deflection distances were found to be linear in time with a moderate decrease in deflection rate at long times. Therefore, a constant rate of deflection was considered an acceptable model for the beam. The time for each beam to deflect 4mm was recorded, plotted as a function of the assumed geometrical dependence (Figure 3.15), and fit with a straight line, demonstrating that the derived form fits the data. Using this slope, determination of the creep response parameters A and B is straightforward using Equation 3.14. This is shown in Figure 3.16 and Figure 3.17.

$$A\exp\left(\frac{B}{T(K)}\right)=\frac{2}{3}\nu_2\frac{\left(d^3/W^4\right)}{t} \tag{3.14}$$

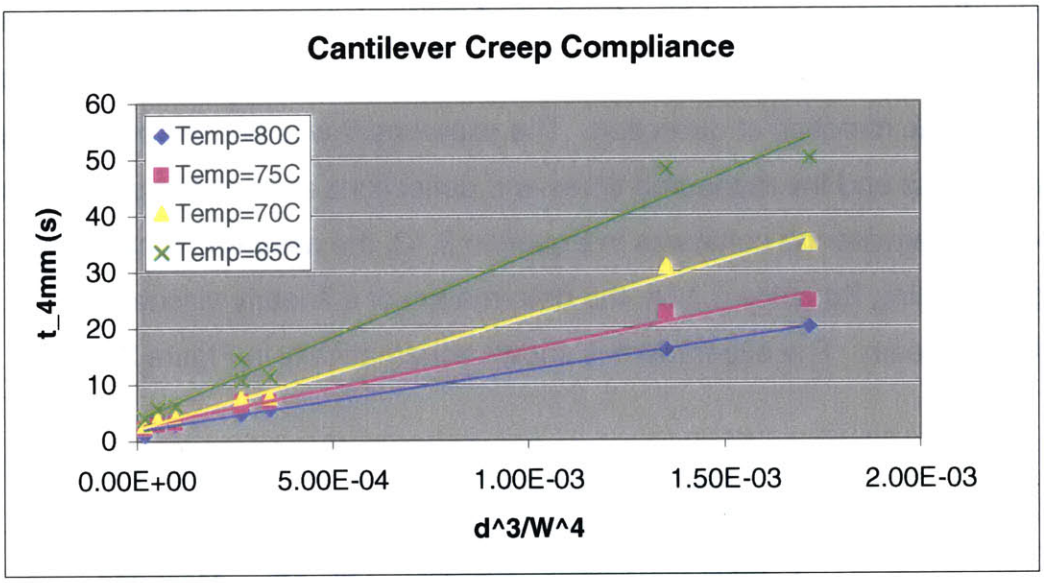

Figure 3.16 Experimental data for macroscopic cantilever tip deflection. Data represents time to 4mm deflection (t_4mm) of beams of several beams with various dimensions tested at several temperatures.

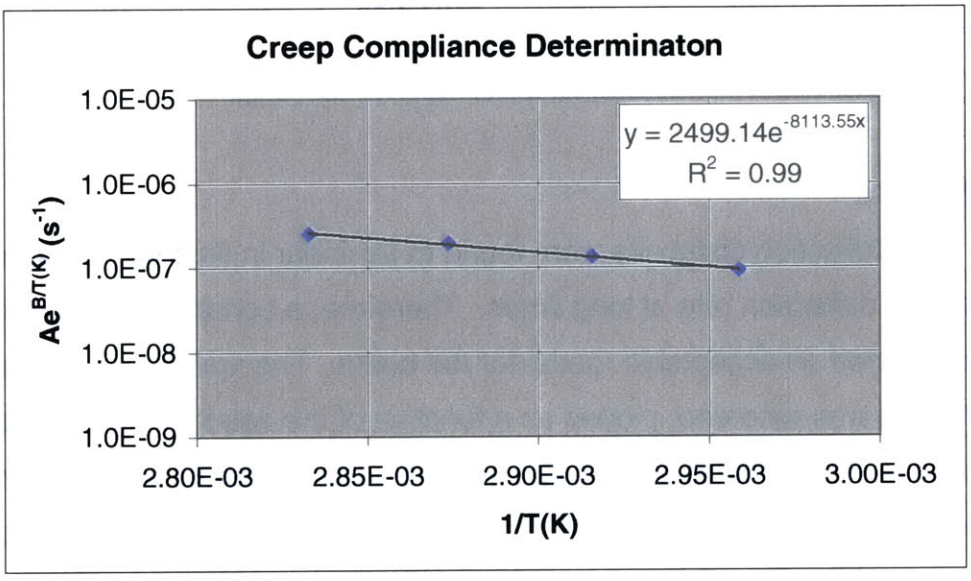

Figure 3.17 The constants in the assumed creep equation are determined from this semi-log plot. Data points represent slopes from Figure 3.16 used in Equation 3.14.

3.8.4 Empirical Estimation of Creep Compliance

The estimated values of the creep response constants are determined from the experimental data and are given in Table 3.3.

Constant	Estimated Value
A	2499 s^{-1}
B	-8113.55 K

Table 3.3 Estimated values of creep compliance constants from Figure 3.17.

The estimate of the viscous dominated creep compliance is therefore taken to be

$$J(t,T) = \frac{2499}{\rho g d}\left[\exp\left(\frac{-8113.55}{T(K)}\right)\right]t \qquad (3.15)$$

This empirical estimate of the creep response function is then used to make conservative predictions regarding deformation of microfabricated channels to determine permissible ranges of feature dimensions and film thicknesses.

3.9 Microchannel Deformation

3.9.1 Prediction of Microchannel Deformation Time

A PLGA biodegradable microchannel is a microscopic viscoelastic beam that can be modeled as a doubly clamped beam deforming plastically under the constant uniformly distributed load of its own weight. Since the center of a doubly clamped beam is the point of maximum deflection, it will be the first location to suffer complete channel collapse. Substituting the estimated creep response into 3.12B, the maximum deformation is given by Equation 3.16.

$$v(W/2,t,T) = \frac{A}{32}\frac{W^4}{d^3}\left[\exp\left(\frac{B}{T(K)}\right)\right]t \qquad (3.16)$$

A characteristic time to deformation τ_{def} can then be defined as the time required for the center of the beam to deflect the entire height of the channel h_0.

$$\tau_{def} = \frac{32h_0\frac{d^3}{W^4}}{A\exp\left(\frac{B}{T(K)}\right)} \qquad (3.17)$$

Key features of this prediction are that the deformation time is directly proportional to the height of the channel, the film thickness to the third power, the inverse of the channel width to the fourth power, and that it is exponential in temperature. This is consistent with experimental observations that the most difficult channels to bond without deformation are those with wide shallow channels made from very thin films. Such channels require low bonding temperatures near the glass transition temperature. Conversely, smaller width channels are less sensitive to process parameters and can be bonded rapidly at higher temperatures.

Photolithography and subsequent etching offer exceptional control over channel widths, W, and channel height, h. In addition, time and temperature are easily controlled. However, equation 3.17 highlights the need to also obtain good control over film thickness, d. Such control is not emphasized in this thesis, however straightforward improvements in thickness control and uniformity can be made by employing an alternative tooling material and/or longer compression times as described in Chapter 2.

3.9.2 Microchannel Bonding Experiments

Guided by the newly developed bonding model, long 10μm deep microchannels of various widths from 30μm to 3000μm were compression molded and bonded at several times and temperatures. Since the thickness uniformity is not well controlled due to the flexibility of the PDMS mold, the thickness was measured after molding, using a digital micrometer. The local thickness was measured at three locations along the length of each channel, providing a spatial map of local film thickness. Throughout the bonding process, samples were cooled and inspected macroscopically for evidence of collapse. Samples were bonded until deformation occurred to determine the time as a function of temperature, channel width, and local film thickness. The time and location of channel collapse were noted, and the corresponding channel width and local film thickness were used to generate a prediction. A figure of merit, t^*, is defined as the ratio of the predicted to the experimental deformation time.

$$t^* = \frac{\tau_{theory}}{\tau_{\exp}} \tag{3.18}$$

The experimental microchannel deformation times are plotted versus the assumed geometric ratio (d^3/w^4) and the data is found to be fairly linear as predicted (Figure 3.18) with the slopes exhibiting an exponential temperature dependence, demonstrating the qualitative predictive power of the model. In Figure 3.19 the figure of merit t^* is used to compare theory with experiment quantitatively. The model is shown to predict deformation time to within a factor of two. This is approximately the uncertainty in the predicted value due to the experimental error in creep response estimation combined with the experimental error in microchannel deformation time as described in the next section.

3.9.3 Results

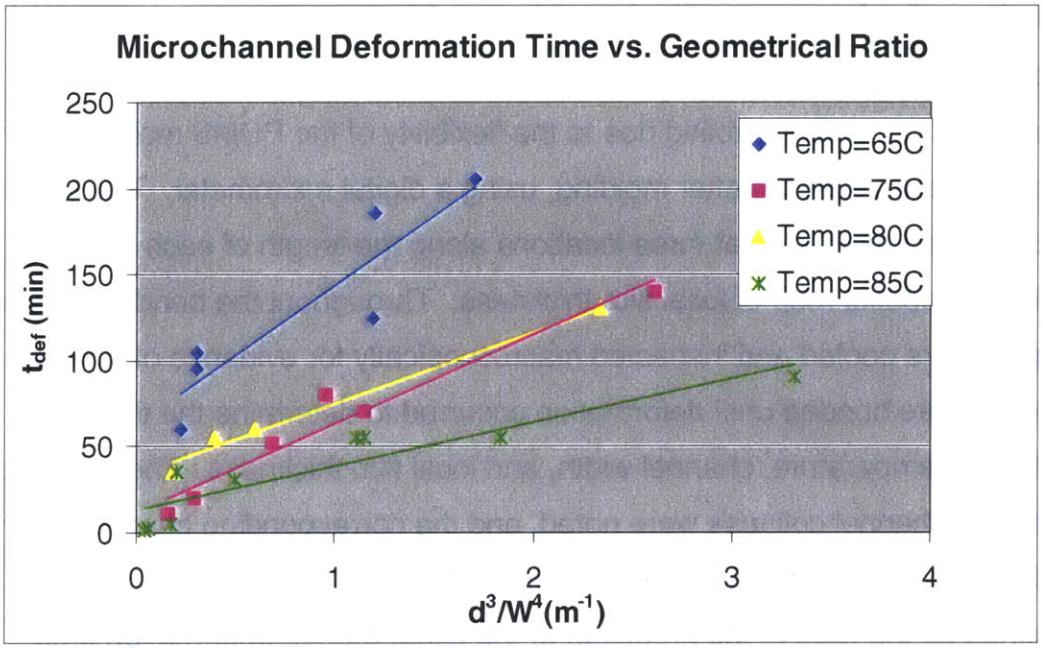

Figure 3.18 Deformation time versus channel dimensions. Model predicts a linear relationship, and data shows reasonable agreement. All R^2 values (>0.8).

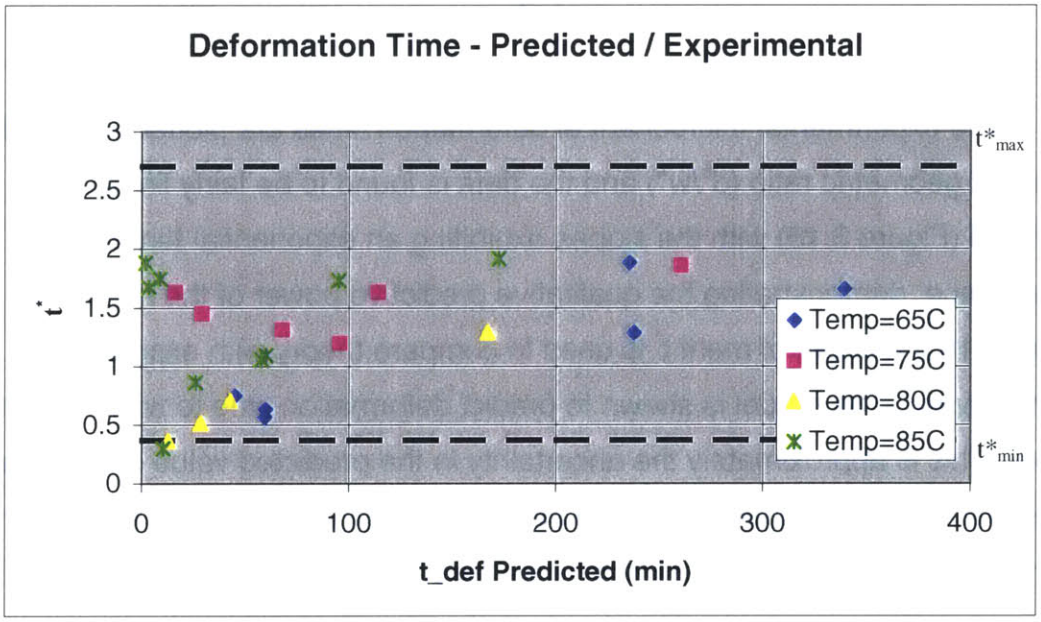

Figure 3.19 Ratios of predicted and experimental deformation times versus predicted deformation time. A perfectg prediction would yield t*=1.

3.9.4 Model Limitations and Uncertainty

Assuming that the form of the equations is correct, there are several experimental sources of uncertainty and error that contribute to discrepancies between predicted and observed deformation times.

First, the predicted times depend on correct determination of creep response parameters A and B. This experiment was performed on a beam with a thickness that varies by up to 15%, ($\Delta d\%=0.15$). In addition, the visual determination of cantilever tip deflection distance is estimated to have an error of 10% ($\Delta v_1\%=0.10$). Because these are related to the creep response by a simple power law relationship, the percent uncertainty in the predicted deformation time t_{pred} can be calculated using Equation 3.19 and is found to be approximately 46% ($\Delta t_{pred}\%=0.46$).

$$\Delta t_{pred}\% = \sqrt{(3\Delta d\%)^2 + (\Delta v_1\%)^2} \tag{3.19}$$

Next, the experimentally determined microchannel deformation times have associated uncertainties. Since samples were only inspected at discrete time points, there is an uncertainty of 10% associated with the microchannel deflection time. Since this time is ascribed to a film of a certain thickness, the 15% film thickness uncertainty must also be included. These variables exhibit a power law relationship as before, so the total uncertainty in experimental deformation time t_{exp} is calculated using equation 3.20, and is found to be approximately 46% ($\Delta t_{exp}\%=0.46$).

$$\Delta t_{exp}\% = \sqrt{(3\Delta d\%)^2 + (\Delta t_{def}\%)^2} \tag{3.20}$$

These errors can be combined to set bounds on the quality factor t*. An upper bound t^*_{max} and a lower bound t^*_{min} are calculated using Equation 3.21.

$$t^*_{\substack{max \\ min}} = \frac{1 \pm \Delta t_{pred}\%}{1 \mp \Delta t_{exp}\%} \tag{3.21}$$

The result predicts that due to experimental uncertainty (dotted lines in Figure 3.19) alone, t* is expected to range from 0.37 and 2.7. All but two data points from microchannel deformation experiments were found to fall within this range (Figure 3.19), suggesting that the model provides a good description of the plastic deformation failure mechanism.

In addition to the experimental sources of error, it is possible that several of the model assumptions might also contribute to error. First, the sample was assumed to wet uniformly across the sample in a time that was only temperature dependent while the time to intimate contact was actually observed to have some film thickness dependence. Another possible source of error is related to the assumption that deformation occurs by purely viscous deformation. This neglects the small elastic components of the viscoelastic solid and ultimately leads to overestimation of the deformation rate (or underestimation of the deformation time). This is potentially responsible for the points that reside just outside the experimental error line in Figure 3.19.

3.10 Process Window Determination

In this section, the time to deformation is combined with the time to bonding to calculate a process window as defined in Equation 3.1. Once determined, this process window can be used in several ways. For a given design, a window of times and temperatures can be determined. Alternatively, if throughput is to be maximized while preserving reliability, one might specify a maximum time to bonding, and a minimum process window. This can be used to aid device design by constraining permissible channel geometries.

The process window, as defined previously, is the difference between characteristic times of deformation and bonding, and is therefore dependent on temperature, and device dimensions according to Equation 3.22. In order to provide a conservative estimate for the process window, the predicted time to deformation has been replaced by ($0.37t_{def}$) to account for experimental errors in

determining the creep compliance parameters A and B as discussed in the previous section. A plot of bonding and deformation time are shown in Figure 3.20 to show the predicted process window versus time. One can construct a similar figure given for the specific height, width, and film thickness of any specific design to select appropriate bonding process parameters. To determine the optimal process, the maximum temperature that yields an acceptable process window should be selected, and the samples should be bonded for a time greater than the bonding time and less than the deformation time.

$$\Delta = 3.42E-19\exp\left(\frac{15506}{T(K)}\right)\left[1.39E16\left(\frac{hd^3}{W^4}\right)\exp\left(\frac{0.161}{T(K)}\right)-1\right] \qquad (3.21)$$

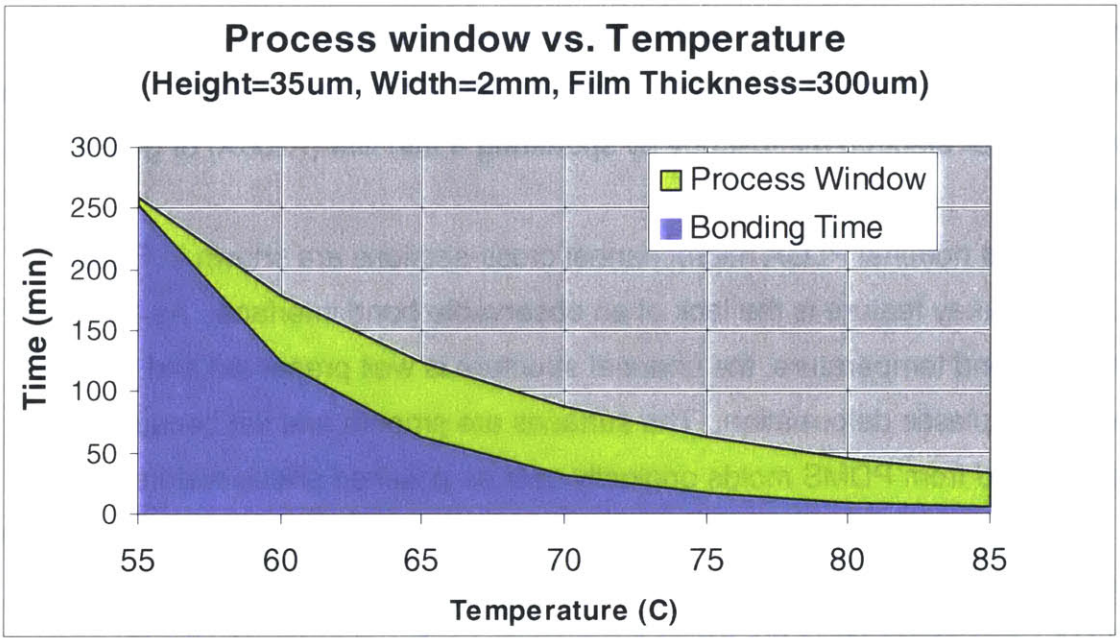

Figure 3.20 Thermal dependence of bonding and deformation times for selection of an optimal process as introduced in Section 3.3 (plot is for fixed dimensions).

Additional insight can be gained by defining a dimensionless parameter γ as the ratio of the deformation time to the bonding time. Only when this parameter is sufficiently greater than unity is reliable bonding possible.

$$\gamma = \frac{\tau_{def}}{\tau_{bond}} = 1.39E16\left(\frac{hd^3}{W^4}\right)\exp\left(\frac{0.161}{T(K)}\right) \tag{3.22}$$

As one looks to reduce the total amount of polymer in biodegradable microdevices, significant reductions in film thickness will be required. Having a model of the bonding process that offers intuition about dimensional and process control dependencies is an invaluable tool when faced with the challenge of designing more delicate biodegradable microchannels. In the next section, the bonding model is used to guide the fabrication of a wide range of microchannels.

3.11 Bond Morphological Characterization

This section presents morphological results of microchannel bonding. After fabrication, samples were cleaved by beginning a crack at the desired location with a razor blade, freezing the sample in liquid nitrogen for 1 minute, and cleaving over a sharp edge to guide the line of fracture. Samples were then prepared for electron microscopy by sputtering a thin film (~200Å) of gold on the surface.

Two nominal PLGA microchannel cross-sections are shown in Figure 3.21. The key feature is the lack of an observable bond interface. As a result of the low bond temperature, the channel structure is well preserved and there is negligible plastic deformation. The surfaces are smooth and flat because they are molded from PDMS molds originally cast on polished silicon wafers.

Figure 3.22 shows an example of high-resolution microchannels fabricated by bonding the micron scale features from Section 3.2 to unpatterned films of PLGA. The channels in the figure have cross-sectional areas of ~5μm^2.

The robust nature of the bonding process is demonstrated by fabricating high width-to-height ratio microchannels as pictured in Figure 3.23. The channel shown has a height of only 10μm and a 2mm width, yielding an aspect ratio of 200. At low bonding temperatures ~60°C, near the glass transition temperature, the bonding is performed reliably and without channel deformation or collapse.

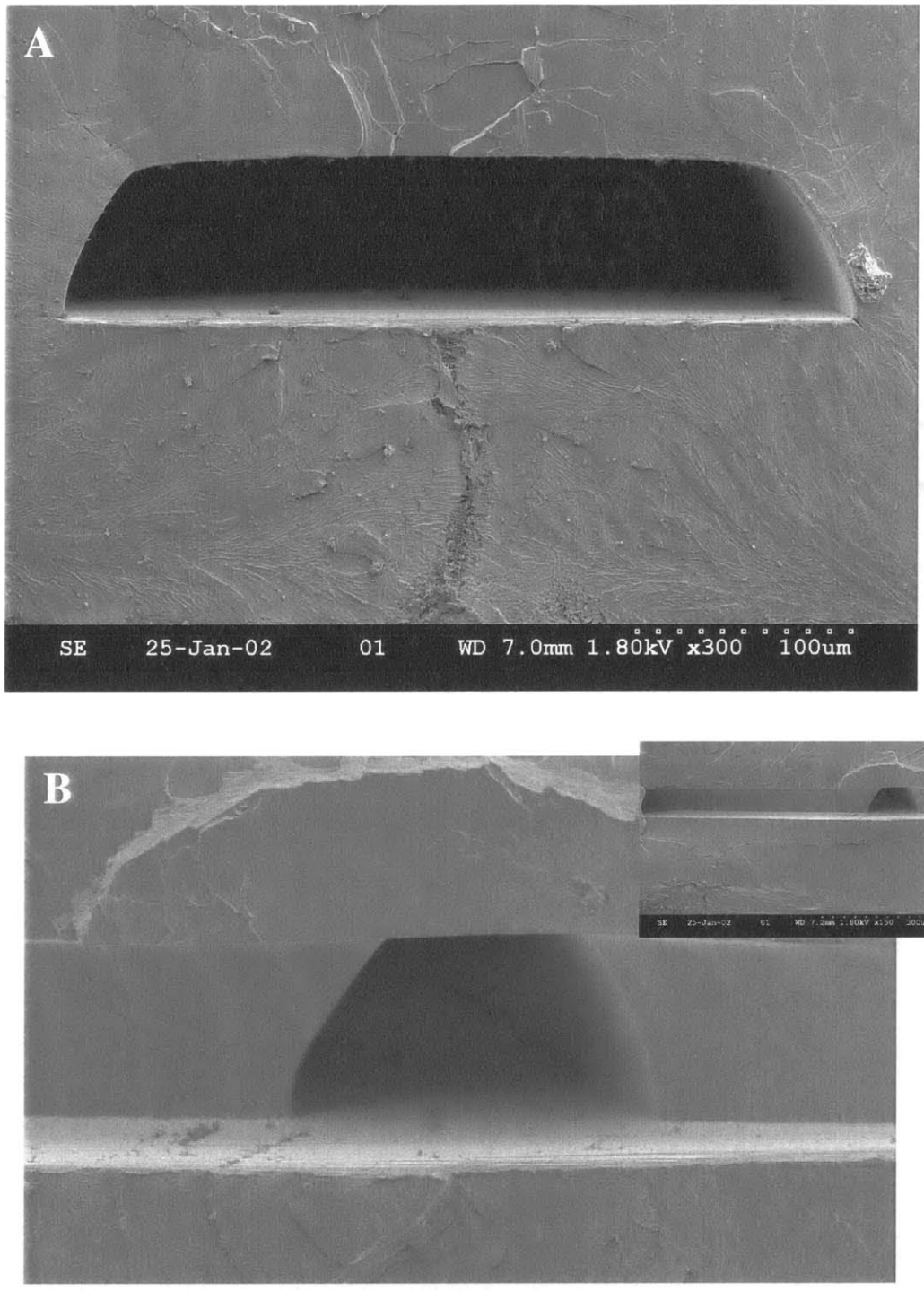

Figure 3.21 A) 50μm deep, 350μm wide bonded microchannel with no observable bond interface, and B) A view of a branching channel network cut along the axis of one channel, revealing the cross-section of the branching channel.

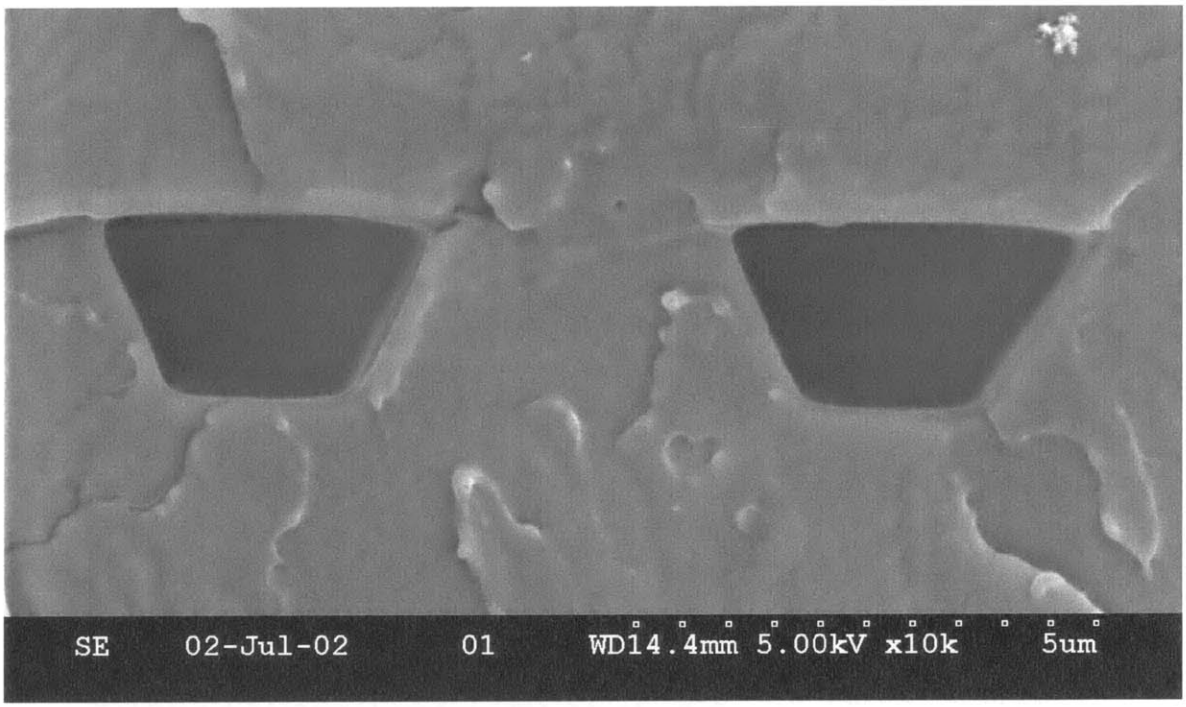

Figure 3.22 2μm deep, 3μm wide bonded high-resolution microchannels.

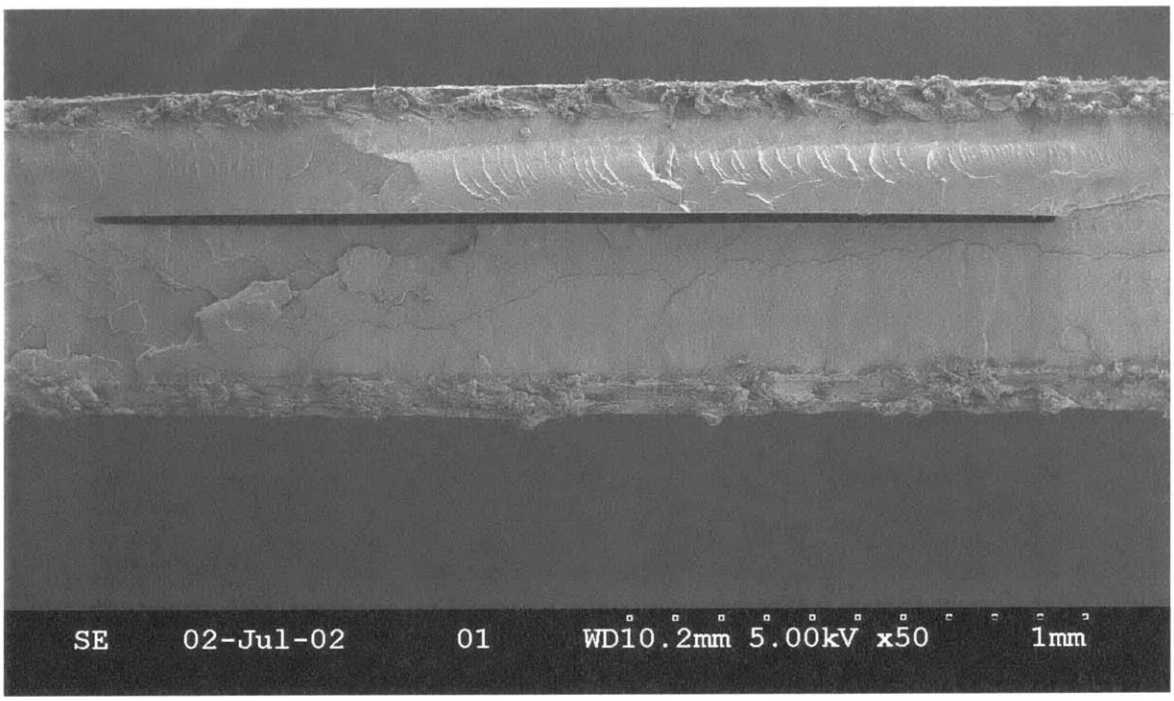

Figure 3.23 10μm deep and 2mm wide high aspect ratio (~200) bonded microchannel.

3.12 Discussion

In this chapter, a thermal fusion bonding process is used to bond the PLGA 85:15 amorphous thermoplastic as an alternative to previously used intermediate adhesion layers and solvents that can distort microstructures or introduce nonresorbable materials. The bonding process enables three-dimensionality and fabrication of a wide range of monolithic microchannels ranging from microns to millimeters in a rapid, reproducible fashion.

Diverse channel geometries are required to build microfluidic networks with flexible fluidic resistances. Planar processing typically lends itself to creating at most a few different feature thicknesses per layer. Therefore when building microfluidic networks, resistances must be designed by selecting appropriate channel lengths and widths. This is the motivation for exploring the range of channel dimensions that can be reliably bonded. In addition to typical microfluidic channels geometries, high-resolution conduits are demonstrated, offering the unique opportunity to design and fabricate controlled permeability and size exclusion regions of a device. This could potentially be used to deliver potent soluble factors by controlling channel-to-channel permeability or to spatially segregate two cell populations while allowing chemical communication via soluble products. High aspect ratio features (width-to-height ratio) were also created that might allow the equivalent of flat plate bioreactors to be integrated into the microdevices. Because these systems have been studied extensively for use in extracorporeal liver assist devices, biodegradable flat plate fluidic structures offer an opportunity to combine *in vivo* and *ex vivo* approaches in a fully implantable format.

The bonding process used to seal these channels has only two control variables, temperature and time, making process development straightforward. Increases in either time or temperature have the similar effect of accelerating bonding, and in extreme cases, causing plastic deformation and collapse of microchannels. To avoid collapse of channels during bonding, the process was modeled. Bonding was divided into two stages of intimate contact and interdiffusion, and it was compared to a competing process of plastic deformation

to define a process window for achieving robust bonding without suffering channel collapse.

In practice, bonding can be accelerated with moderate applied pressure, reducing the time to achieve intimate contact. However, this must be applied in a diffuse manner because localized forces will cause rapid deformation. This chapter has discussed the limiting case of no applied pressure and the resulting process windows are more than acceptable, yielding a reliable and robust process that is used in the next chapter to build function microfluidic networks.

Key conclusions from the modeling are 1) that deformation time is a function of device dimensions, roughly proportion to $h_0 d^3/W^4$, 2) that the creep compliance, a material property, can be conservatively estimated using a macroscopic cantilever beam, 3) that by treating the material as a purely viscoelastic solid doubly clamped beam, the cantilever results can be used to make conservative predictions about the microchannel deformation time, and 4) that when the predictions are compared to experiment, they predict the time to bonding and time to microchannel collapse within a factor of two, sufficient to guide device and process design without introducing unnecessary constraints.

This approach to predicting deformation is widely applicable to many plastic microfluidic platforms such as polycarbonate, polymethylmethacrylate, or polystyrene, all commonly used for fabricating a variety of biomedical microfluidic devices. However, the model is particularly important for biodegradable polymers such as PLGA that have low glass transition temperatures and are susceptible to deformation even at low temperatures.

The two notable features of this bonding approach are the monolithic nature of the resulting device, and the fact that multiple layers can be bonded in a single step. Parallel processing such as this makes stacking and bonding of microfabricated layers a realistic approach to building three-dimensional biodegradable constructs. The maximum thickness of a device is likely to be limited by the polymer thermal conductivity. For large numbers of films, there will be a significant difference between the time required to achieve thermal equilibrium for the outer films and the inner films. Therefore, the process window

must be sufficiently long to accomadate this thermal diffusion and allow the center to achieve the process temperature and bond before the outer channels collapse. The problem can be viewed as thermal diffusion into a solid with the boundaries maintained at a fixed temperature. The problem scales as the PLGA film stack squared. Therefore, if a 500μm film can achieve thermal equilibrium in approximately 10 seconds (approximated from cantilever experiment), a 5cm stack would require approximately one day. Fortunately, process windows for many microfluidic channels is ~36 hours, so it is reasonable to believe that very large constructs could be fabricated. A scaffold of several centimeters that does not suffer transport limitations would be a substantial improvement and might allow implantation of a therapeutically viable number of cells for engineering tissue of large vital organs.

3.13 Conclusion

This chapter has described the development of a fusion bonding process for stacking and bonding microfabricated layers of biodegradable polymer. A simple model was developed to describe the relationship between bonding parameters of time and temperature and microdevice parameters of dimensions and material-specific creep compliance. The model predictions are shown to provide a good estimate of the time-course of bonding as well as the primary mode of failure, plastic deformation. This is used to define a process window and guide selection of process parameters for fusion bonding. The result is a method for achieving a strong uniform bond across a wide range of geometries. In the next section, this process and the associated model are used to not only seal simple PLGA microchannels, but to build complex three-dimensional microfluidic networks that might be used in high performance microfabricated tissue engineering scaffolds.

3.14 References

[1] Widmer, M.S., P.K. Gupta, L. Lu, R.K. Meszlenyi, G.R.D. Evans, K. Brandt, T. Savel, A. Gurlek, C.W.J. Patrick, and A.G. Mikos, "Manufacture of Porous Biodegradable Polymer Conduits by an Extrusion Process for Guided Tissue Regeneration". Biomaterials. 19: p. 1945-1955, 1998.

[2] Armani, D.K. and C. Liu, "Microfabrication Technology for Polycaprolactone, a Biodegradable Polymer". Journal of Microelectromechanical Systems. 10(1): p. 80-84, 2000.

[3] Yang, F. and R. Pitchumani, "Healing of Thermoplastic Polymers at an Interface Under Nonisothermal Conditions". Macromolecules. 35: p. 3213-3224, 2002.

[4] Maguire, D.M., "Joining Thermoplastic Composites". SAMPE Journal. 35(1): p. 11-14, 1989.

[5] Butler, C.A., R.L. McCullough, R. Pitchumani, and J.W.J. Gillespie, "An Analysis of Mechanisms Governing Fusion Bonding of Thermoplastic Composites". Journal of Thermoplastic Composite Materials. 11: p. 338-363, 1998.

[6] Lee, W.I. and G.S. Springer, "A Model of the Manufacturing Process of Thermoplastic Matrix Composites". Journal of Composite Materials. 21: p. 1017-1053, 1987.

[7] Phillips, R., D.A. Akyuz, and J.-A.E. Manson, "Prediction of the consolidation of woven fibre-reinforced thermoplastic composites. Part I. Isothermal Case". Composites Part A. 29A: p. 395-402, 1998.

[8] Mantell, S.C. and G.S. Springer, "Manufacturing Process Models for Thermoplastic Composites". Journal of Composite Materials. 26(16): p. 2348-2377, 1992.

[9] Ageorges, C., L. Ye, and M. Hou, "Advances in Fusion bonding Techniques for Joining Thermoplastic Matrix Composites: A Review". Composites Part A. 32: p. 839-857, 2001.

[10] Becker, H. and C. Gartner, "Polymer Microfabrication Methods for Microfluidic Analytical Applications". Electrophoresis. 21: p. 12-26, 2000.

[11] Becker, H. and L.E. Locascio, "Polymer Microfluidic Devices". Talanta, 2001.

[12] Reyes, D.R., D. Iossifidis, P.-A. Auroux, and A. Manz, "Micro Total Analysis Systems. 1. Introduction, Theory, and Technology". Analytical Chemistry. 74: p. 2623-2636, 2002.

[13] Fried, J.R., *Polymer Science and Technology.* Upper Saddle River, NJ: Prentice Hall, 1995.

[14] Turi, E.A., *Thermal Characterization of Polymeric Materials.* San Diego: Academic Press, 1997.

[15] http://www.people.virginia.edu/~lz2n/mse209/Chapter16c.pdf, *Temperature Dependence of Thermoplastic Mechanical Properties.*

[16] Wool, R.P., *Polymer Interfaces: Structure and Strength*. New York: Hanser Publishers, 1995.
[17] Kim, Y.H. and R.P. Wool, "A Theory of Healing at a Polymer-Polymer Interface". macromolecules. 16: p. 1115-1120, 1983.
[18] Wool, R.P., "Molecular Aspects of Tack". Rubber Chemistry and Technology. 57: p. 307-319, 1983.
[19] Bourban, P.E., N. Bernet, J.E. Zanetto, and J.-A.E. Manson, "Material Phenomena Controlling Rapid Processing of Thermoplastic Composites". Composites Part A. 32: p. 1045-1057, 2001.
[20] Wool, R.P. and K.M. O'Conner, "A Theory of Crack Healing in Polymers". Journal of Applied Physics. 52(10): p. 5953-5963, 1981.
[21] Veselovskii, R.A., *Adhesion of Polymers*. New York: McGraw-Hill, 2002.
[22] de Gennes, P.-G., *Soft Interfaces: the 1994 Dirac Memorial Lecture*. New York: Cambridge University Press, 1997.
[23] Aradian, A., E. Raphael, and P.-G. de Gennes, "Strengthening of a Polymer Interface: Interdiffusion and Cross-linking". Macromolecules. 33: p. 9444-9451, 2000.
[24] Kovacs, T.A., *Micromachined Transducers Sourcebook*. Boston: McGraw-Hill, 1998.
[25] Wineman, A.S. and K.R. Rajagopal, *Mechanical Response of Polymers An Introduction*. Cambridge: University Press, 2000.

[This page intentionally left blank]

Chapter 4

Biodegradable Microfluidics

This chapter describes the fabrication and characterization of fully biodegradable microfluidic networks. In the previous chapters, two key processes, PLGA surface micropatterning and thermoplastic fusion bonding were developed. In this chapter, those processes are called on to build functional biodegradable microdevices. First an inlet/outlet scheme is integrated with the patterning and bonding processes to build biodegradable ports that are readily connected to standard tubing for perfusion and testing. Once fully fabricated, the microfluidic networks are perfused without leaking, and are demonstrated to be patent and well bonded, supporting pressures well above those that might be experienced in a physiologic setting. Pressure driven flow is used to characterize the hydraulic resistance of two different networks, and suspensions of fluorescent beads are perfused to simulate seeding a cell suspension. Extending the devices to three dimensions, multi-layer microfluidic networks are assembled by stacking and bonding interconnected layers in a single bonding step, demonstrating the ability to fabricate complex networks with vertical conduits. Finally, to demonstrate the power of design flexibility and fabrication reproducibility, the biodegradable microfluidic networks are used to build well defined interconnections between microfabricated pores by fabricating the device proposed in the Section 1.2 of this thesis, "Organ Fabrication Concept". A multi-layer scaffold with arrays of interconnected pores is efficiently and methodically seeded with fluorescent microspheres via the microfluidic channels, demonstrating just one of the many ways biodegradable microfluidics can be used to augment and improve existing tissue engineering scaffold performance.

4.1 Design

4.1.1 Layout Specification

The two microfluidic designs used in this chapter were designed and drawn by Eli Weinberg at Draper Laboratories. Briefly, the designs were both intended to achieve equal flow in each of the smallest channels. This was accomplished in two distinct topologies, termed NET1 and NET2.

The first design, NET1, is a network of similarly sized (~30μm wide) grossly interconnected channels, much like a tissue capillary bed. The second design, NET2, is a hierarchical network comprised of arrays of branched diverging and converging channels. Such a branched design has properties similar to the vascular topology of a large organ in that branched arteries diverge to arterioles and capillaries, and then reconverge to venules and veins. These networks are well suited for development of the PLGA microfluidics fabrication process, as they present a wide range of channel geometries and flows.

The networks are massively parallel, and therefore are reasonably low resistance, making them suitable for testing. They also have large footprints of several centimeters that enable inlets and outlets to be formed vertically without compromising visualization of the channels. Both designs in this chapter were developed considering straight microfluidic channels to be discrete resistors of known lengths. These resistors were connected end-to-end in the desired topology such that the lengths were explicitly defined. The height was assumed to be a constant 35μm, and the channel widths were calculated to achieve the desired flows by solving the linear pressure-flow relation of Equation 4.1 for each branch of the network in MATLAB subject to conservation of mass constraints.

$$\Delta P = RQ \tag{4.1}$$

where ΔP is the pressure drop across a channel length, Q is the bulk flow in a channel, and R is the channel hydraulic resistance. A skeleton topology and the calculated widths are shown in Figure 1.

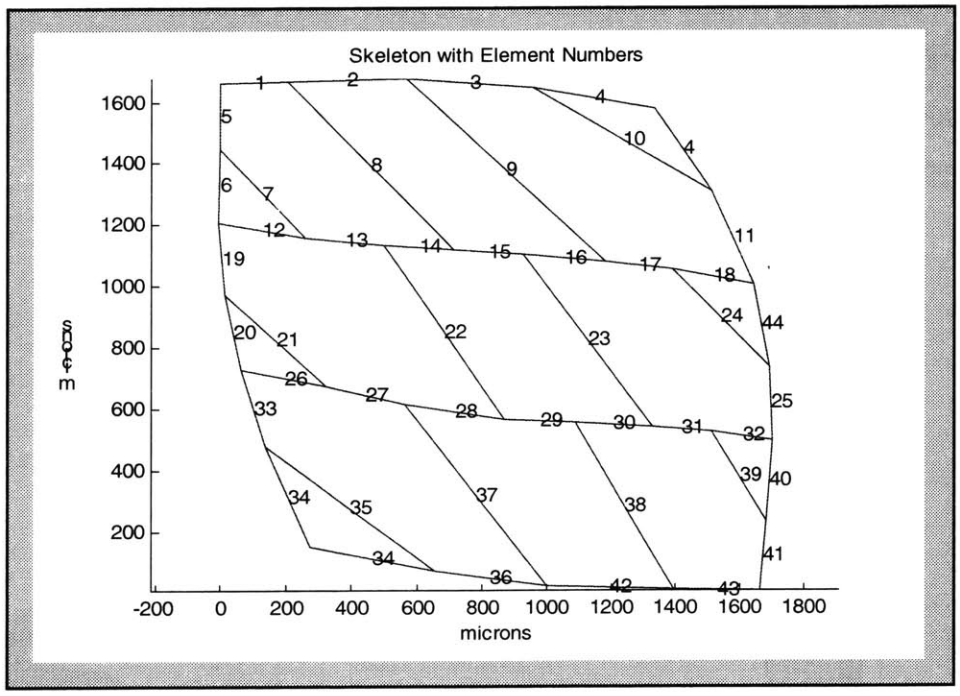

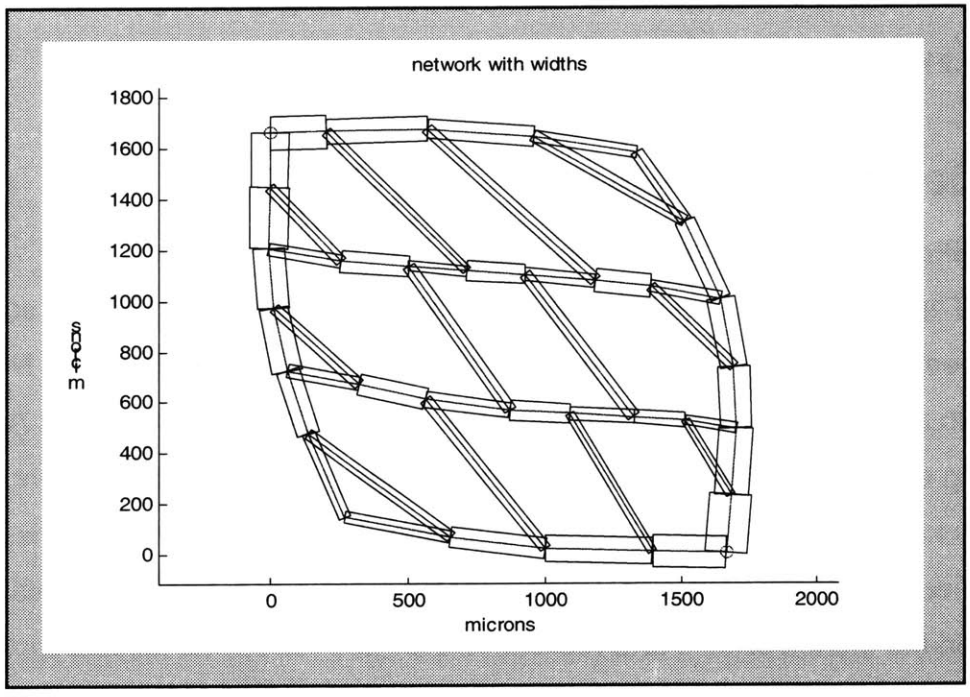

Figure 4.1 Example layout – A) Skeleton topology and B) Network with calculated widths (courtesy of Eli Weinberg).

4.1.2 Mask Layout and Fabrication

Channel dimensions calculated in MATLAB were directly used to generate a CIF (.cif) file, which was converted to postscript (.ps) and used to generate high-resolution transparency films for use as photolithography masks, as described in Chapter 2. The resulting designs are shown in Figure 4.2.

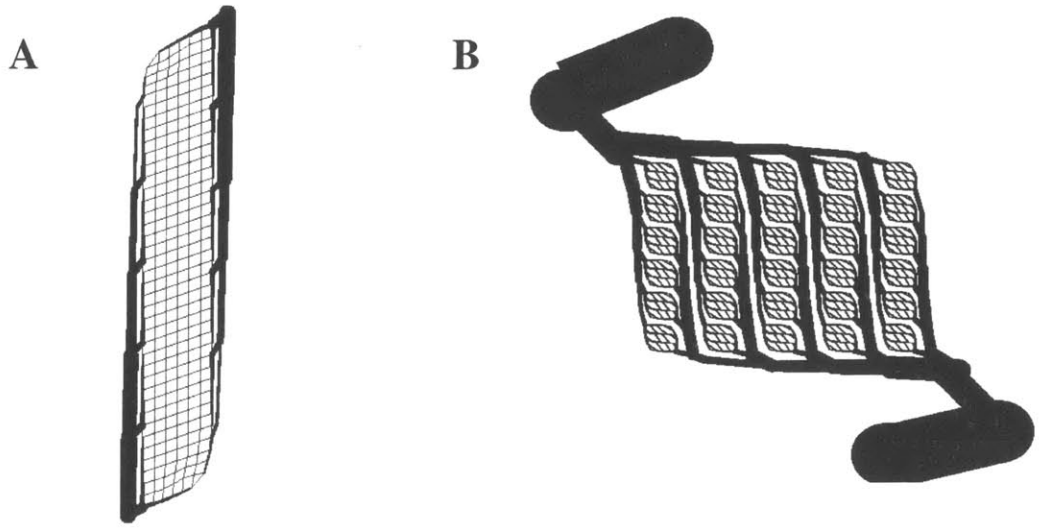

Figure 4.2 Mask layouts for A) NET1 and B) NET2.

4.2 Device Fabrication

4.2.1 Silicon and PDMS Mold Fabrication

The silicon master mold for NET1 is fabricated using a dry silicon etch described in Appendix A, resulting in a "D-shaped" profile. However, for NET2, the mold is fabricated using a DRIE process, also described in Appendix A, resulting in vertical side-walls. Each process has target channel depths of 35μm. After etching, the resist is stripped and a fluoropolymer passivation step is performed to aid release during polymer molding. PDMS prepolymer is cast and cured on the etched silicon, and replicas are formed for use as flexible tooling during compression molding as described in Chapter 2.

4.2.2 Inlets and Outlets – Modification of PDMS

In order to connect to standard flexible tubing, the PLGA compression molding process is modified. First, the PDMS tooling is augmented by bonding a ~1cm tall, ~1mm diameter PDMS posts to the mold at the locations of the inlet and outlet. The posts are cored from a thick (~1cm) unpatterned PDMS layer using a blunted and beveled 16 gauge syringe needle. The posts are bonded to the patterned PDMS mold at the location of the inlet and outlet with a small drop of PDMS prepolymer. After curing for 1 hour at 80°C, the post is secure and a permanent part of the PDMS mold. Next, a ~1cm thick unpatterned film of PDMS is cast cured and peeled from unpatterned silicon surface, and ~3mm diameter holes are punched, spaced to overlay the inlet and outlet posts. When the two films of PDMS are mated, they define an annular structure that forms biodegradable ports during PLGA compression molding. Parallel fabrication of the inlets and outlets during the molding process is particularly advantageous, as it results in connectors that are both self-aligned and require no assembly. The PDMS modifications and the inlet/outlet strategy are shown in Figure 4.3.

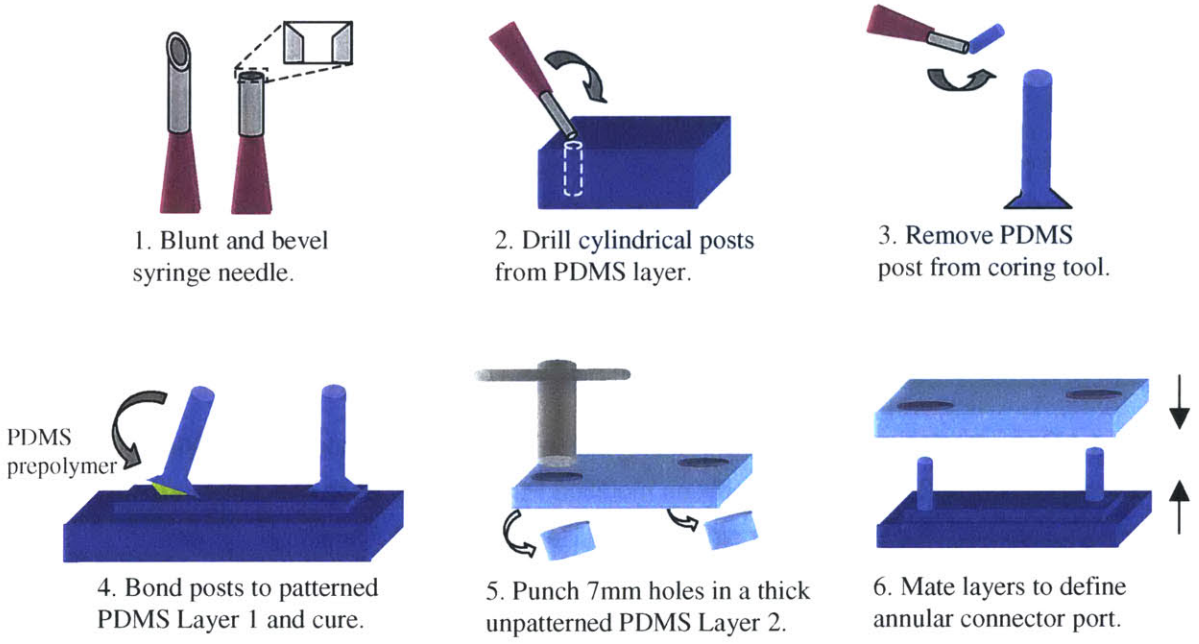

Figure 4.3 Modification of PDMS tooling for inlet and outlet fabrication.

4.2.3 Compression Molding of PLGA with Connectors

The modified PDMS is placed on a hotplate and covered with PLGA pellets, taking special care to surround the inlet and outlet posts with a generous number. The top PDMS layer is placed over the bottom piece and lowered onto the pellets such that the inlets and outlets align. A rigid plate is added to the stack to insure that uniform force is applied across the entire pattern, and the stack is heated for two minutes to allow the pellets to reflow. Next, 100-300lbs of force is applied for 2 minutes to compress the PLGA melt. While still at the melt temperature, the rigid plate is removed and the inlets and outlets are inspected. If they are not completely filled, or if the PDMS inlet and outlet posts are not well centered, additional pellets can be added in the annular structure from above using tweezers. The rigid plate is then returned to the stack and the compression molding is continued until completion (approximately 5-10 minutes.) This manual step is only required during process development stages, and can be eliminated by optimizing the amount and arrangement of pellets. The process schematic is shown in Figure 4.4.

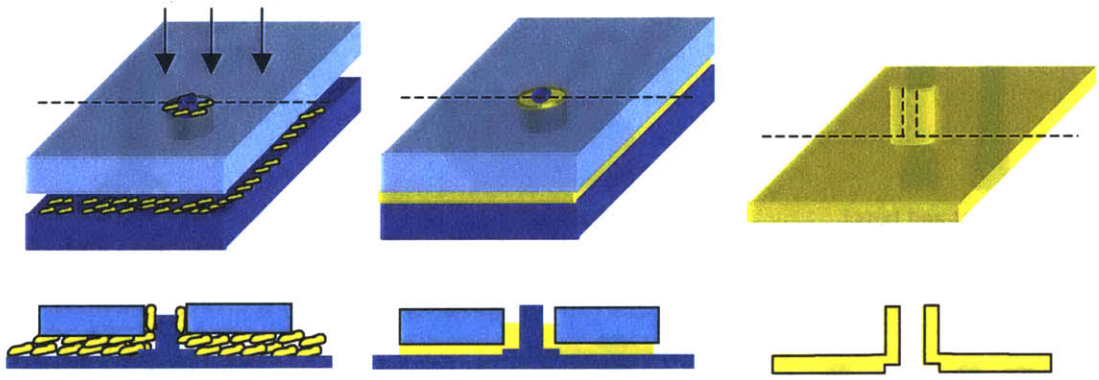

Figure 4.4 Compression molding of microfluidic inlets and outlets with cross-section views through fluidic port. A) PLGA pellets between modified PDMS mold. B) PLGA pellets are heated and compression molded into annular structure. C) Resulting PLGA film with fluidic port.

4.2.4 Thermal Fusion Bonding

The microstructured surfaces with vertical inlets and outlets are bonded to patterned or unpatterned layers using the fusion bonding process developed in Chapter 3. The bonding and deformation model is used to identify appropriate

temperatures and times. An example of the modeling results are shown in Figure 4.5 for NET-2 (maximum channel width ~3mm). In practice, samples are inspected periodically, and diffuse finger pressure is applied to areas that are slow to achieve contact. If localized force is applied, such as with tweezers, it is found to cause rapid channel deformation. Once in contact, interdiffusion proceeds and interfacial strength develops according to model predictions.

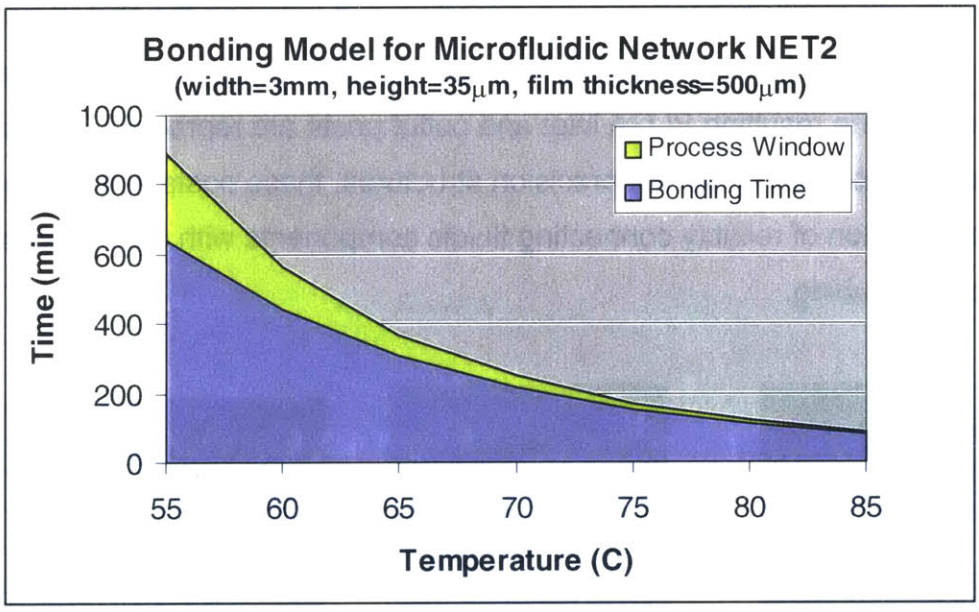

Figure 4.5 Bonding and deformation model predictions for maximum channel width of 3mm.

4.2.5 Device connectors

Silastic tubing (Dow Corning) with 1/8" inner diameter is fit over the PLGA posts at the inlet and outlet and secured with 5-minute epoxy. The tubing is then used as a sleeve into which 1/16" inner diameter silastic tubing with 1/8" outer diameter is fit. This smaller tubing is readily connected to plastic luer lock connectors, adaptors, and syringes for perfusion and testing. The flexible silastic tubing is particularly desirable because it shields the brittle PLGA ports from potentially destructive forces inadvertently applied during use.

4.3 Morphological Characterization

4.3.1 PLGA Molded Films

The PDMS posts have a slightly increased radius at the top and bottom. This is due to the beveled nature of the modified syringe needle. The widened base facilitates bonding and is desirable while the top widening can cause unnecessary stress on the post during PLGA device removal. The annular structures are nicely defined and the generous gap between the PDMS post and the outside of the annular structure make for a forgiving process with respect to alignment. The resulting PLGA inlet and outlet posts are reproducibly aligned, patent, and secure. While not precision structures, these posts achieve the desired function of reliably connecting fluidic components with conventional macroscale tubing.

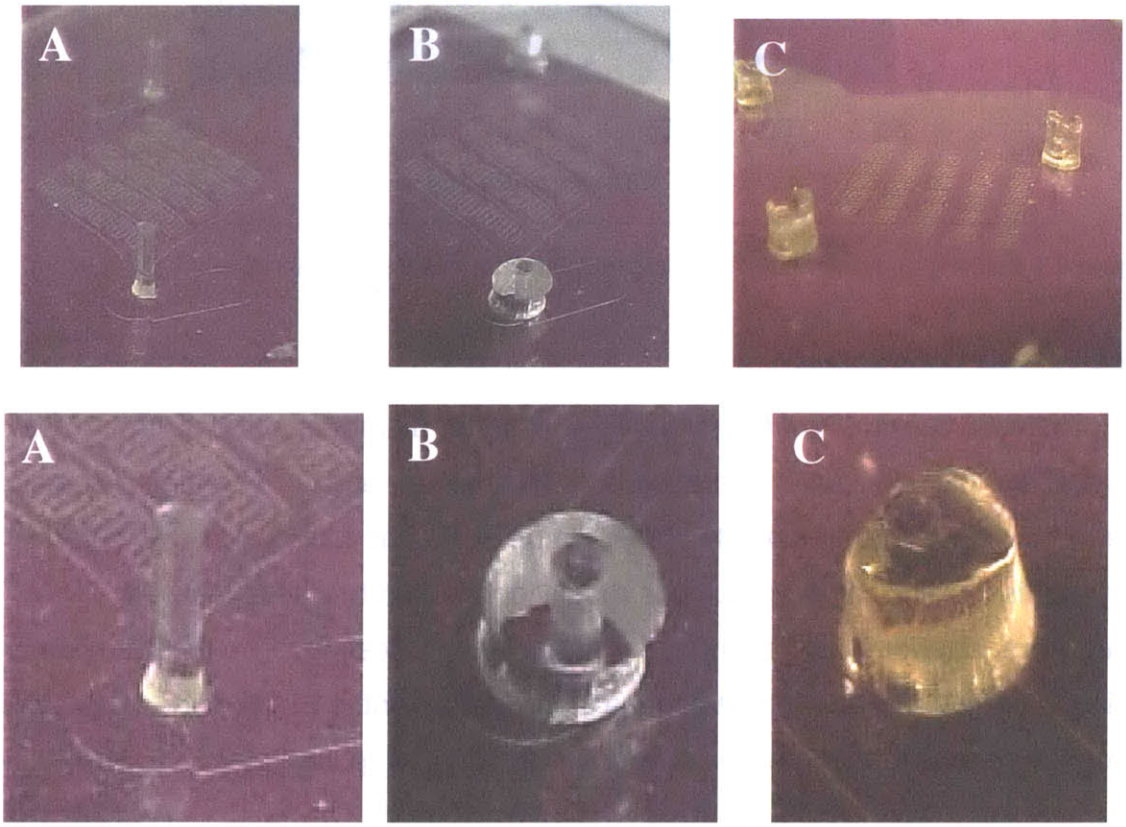

Figure 4.6 PLGA inlet/outlet fabrication. A) PDMS mold with vertical posts. B) PLGA layers mated, with top PDMS layer and bottom layer posts defining annular connector. C) PLGA microfluidics and connectors after molding.

4.3.2 Microchannel Patterns

As mentioned previously, pattern transfer is nearly perfect, with channel dimensions matching drawn features with ~0.1μm precision. As is common in soft lithographic processes, resolution is limited by the photolithography and etch processes used to fabricate the silicon master mold [1]. The corners are sharp and the surfaces are locally flat, both of which are critical for high performance bonding. There are a small number of defects in the surface, likely the result of processing outside of a cleanroom. However, these are much smaller than the surface microstructures and do not seem to impact bonding. Macroscopically, the films appear flat, however a small amount of film bowing might be present.

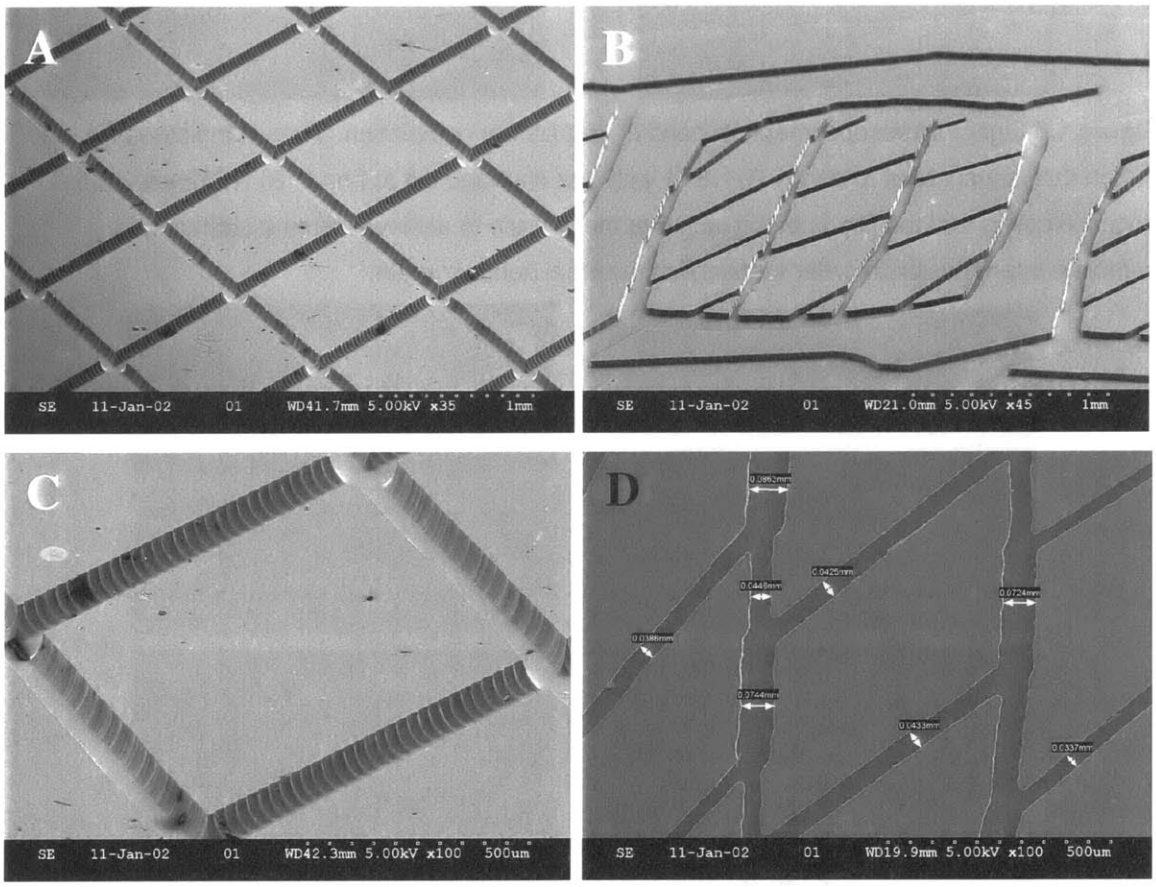

Figure 4.7 Scanning Electron Microscopy of unbonded biodegradable PLGA NET1 and NET2.

4.3.3 Bonding

Fusion bonding resulted in fully patent microchannels as seen under light microscope. The bonding process is inspected at several time points to monitor the development of surface intimate contact. Microscopic evaluation allows determination of regions that remained unbonded. Figure 4.8 shows microscopic inspection of NET1 and NET2 just before bonding is complete.

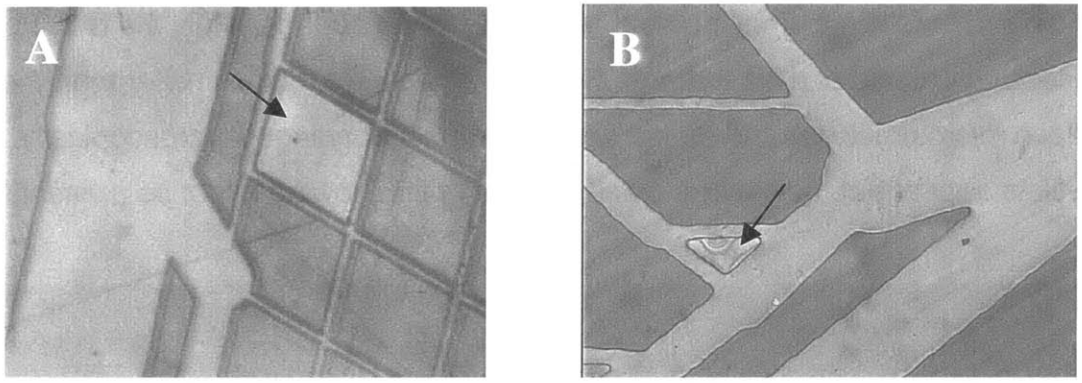

Figure 4.8 Light microscope image of bonding just before completion. Arrows indicates the last region that is just about to bond. A) NET1 with one diamond left to bond. B) NET2 with stress rings indicating that the film is being pulled to the surface to achieve intimate contact and complete interdiffusion in order to establish maximal bond strength.

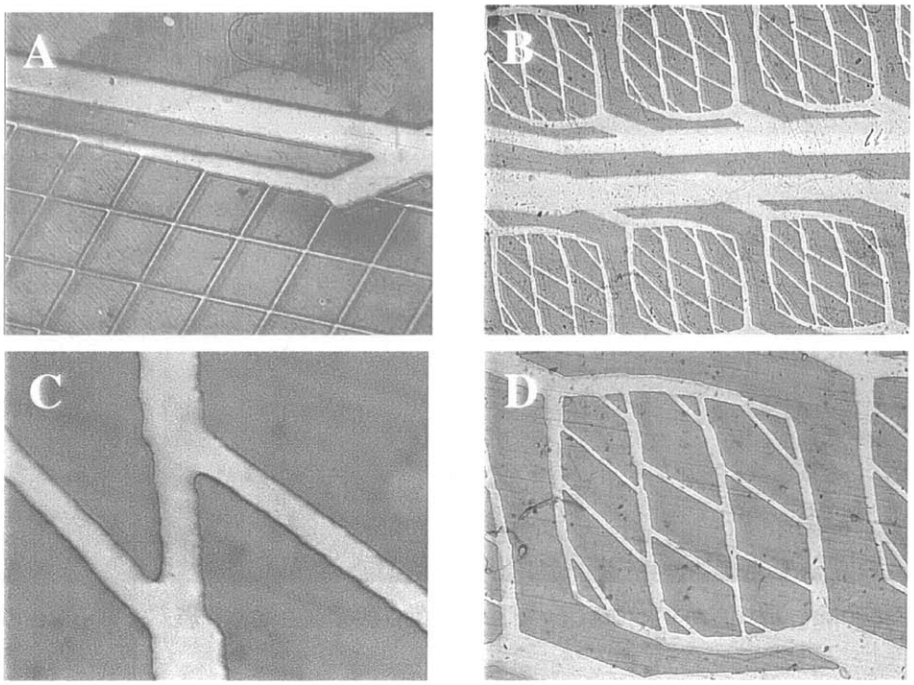

Figure 4.9 Light microscope images of completely bonded A) NET1 and B-D) NET2.

Fusion bonding is found to proceed without significant deformation. Slight downward bowing can be observed for the >1mm wide channel in Figure 4.10A, but all smaller channels are well preserved. Electron microscopy reveals no observable interface, suggesting that significant interfacial bond strength is achieved, and that a monolithic microchannel structure is present.

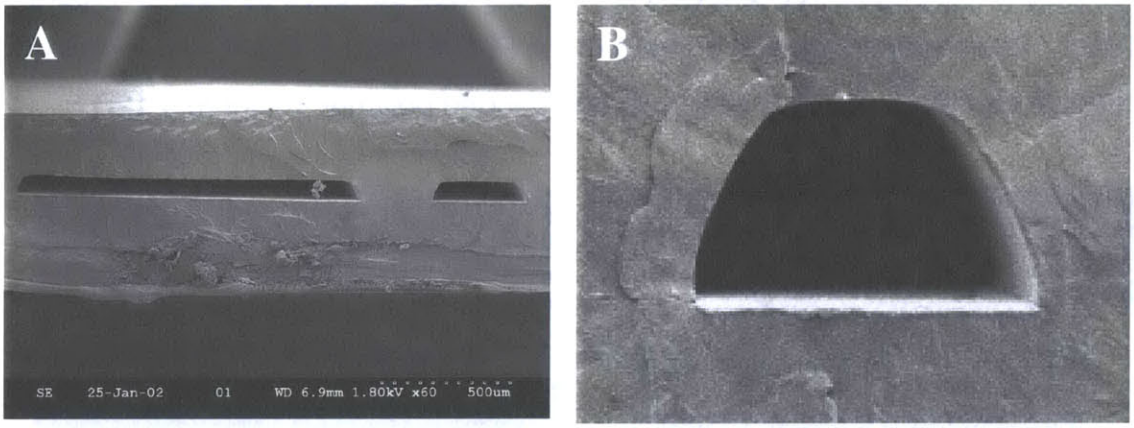

Figure 4.10 Cross-section of completely bonded NET1 network channels. A) Two wide microchannels ~1mm and ~150μm widths and B) a smaller channel of ~35μm width.

4.3.4 Completed Microfluidic Devices

Completed devices are connected to flexible tubing, which is optionally secured with epoxy in preparation for liquid perfusion.

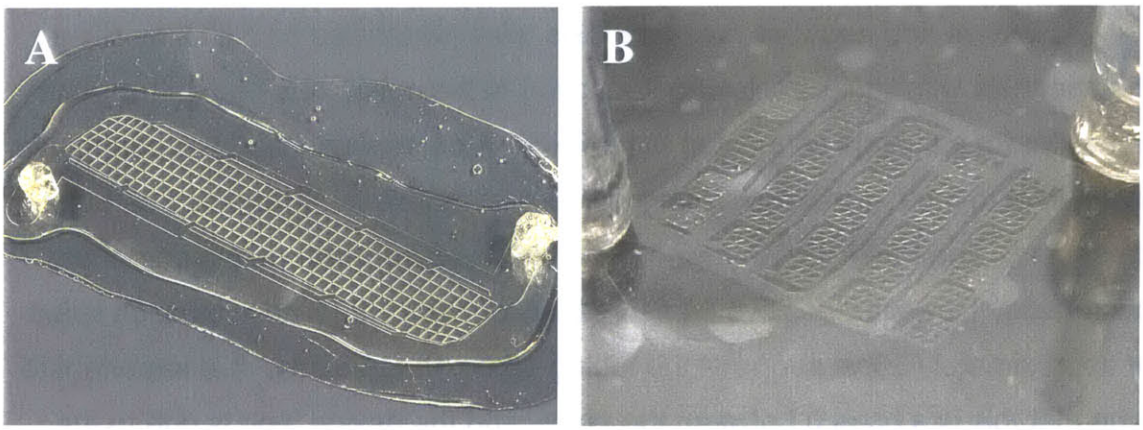

Figure 4.11 Completed microfluidic devices A) NET1, approximately 6cm x 2cm device area, and B) NET2, approximately 3cm x 3cm device area with flexible tubing connected to molded biodegradable fluidic ports.

4.4 Functional Microfluidics Characterization

4.4.1 Patency, Perfusion, and Leak Testing

The microfluidic networks were perfused with a solution of filtered deionized water, fluorescien dye (Sigma), and 0.1% Triton 100X surfactant (Sigma) and examined both macroscopically and microscopically. No leaks or occlusions were observed and all channels are well perfused as seen in Figure 4.12A. The sharp edges and corners of the PLGA microchannels result in clear distinctions between patent channels and bonded polymer in Figure 4.12B.

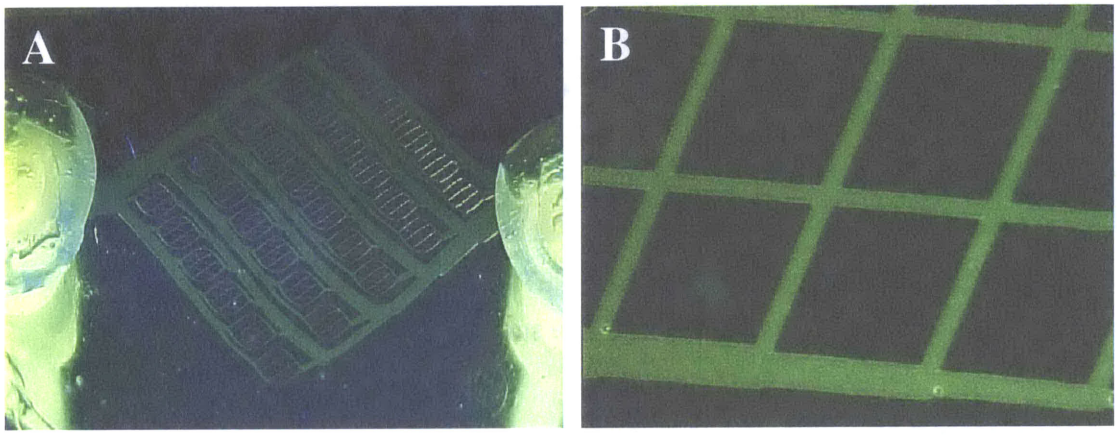

Figure 4.12 A) NET2 fully perfused with aqueous fluorescein dye solution. B) Microscopic image of NET1 ~30μm wide, 35μm deep channels.

4.4.2 Pressure Burst Tests

Positive and negative pressure tests were performed on NET2 by filling the channels with liquid, occluding the tubing at the outlet, and pressurizing the network with a syringe connected to the inlet. A pressure sensor was connected at the inlet to measure abrupt changes in pressure that were recorded as burst pressures. The PLGA-PLGA fusion bond did not delaminate during any of the burst tests. However, positive pressure tests of three NET2 devices each failed at approximately 50psi at one of the tubing-epoxy-PLGA joints. It is important to note that this is a breach between the epoxy and the device, and is due to the use of a nonideal adhesive for tubing attachment. This result does not represent a fracture of the PLGA device itself. None of the negative pressure tests caused

channel collapse or fluid leaks for pressures up to –50psi. For comparison, the maximum pressure experienced physiologically is approximately 200mmHg (<4psi) in the femoral artery during the peak of the systolic pressure wave [2]. The PLGA device is demonstrated to withstand tenfold greater pressures than are found in the vasculature, making it potentially suitable as an implantable device.

4.4.3 Microfluidic Resistance Characterization

The hydraulic resistance of each network fabricated in this chapter was determined by forcing a known volumetric flow with a precision syringe pump and measuring the inlet pressure. The outlet was left to drain into an open container and was assumed to be at atmospheric pressure. A 0.1% Triton 100X surfactant solution in phosphate buffered saline was infused at several flow rates using the Harvard PHD2000 Syringe Pump (Harvard Apparatus), and the steady state inlet pressure was measured with a digital pressure sensor (Merigauge). The fluidic resistance measurement setup is shown in Figure 4.13. The ratio of measured pressure to applied flow was used to calculate the hydraulic resistance in NET1 and NET2.

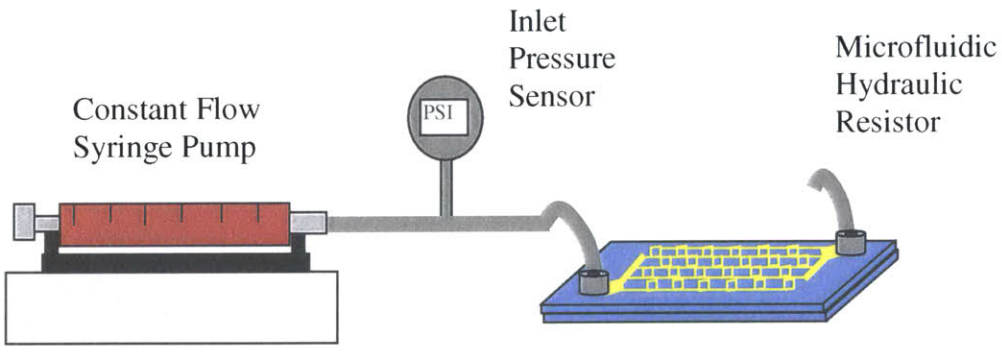

Figure 4.13 Microfluidic network hydraulic resistance measurement system.

All air was eliminated from the system before testing to improve the response time of the measurement system. The surfactant solution improved wetting and reduced bubble formation in the hydrophobic PLGA microchannels. Despite the low surface tension fluid, networks trap bubbles during initial channel filling. The networks are massively interconnected, and therefore have several parallel paths of different lengths, each filling at a different rate. Air is consistently trapped in all but the first paths to completely fill. This is aggravated by the fact that once formed, bubbles are difficult to dislodge from the massively parallel networks because the occlusions do not cause a significant enough increase in network resistance. Insufficient pressure differentials are generated across the bubbles and they are not easily mobilized.

Theoretical prediction of the network resistance was made using the rectangular solution to the viscous-dominated Navier-Stokes Equation for each straight microfluidic branch. Each branch was taken to be a discrete fluidic resistor, the resistive network was solved using SPICE circuit analysis software as described in Appendix C. The predictions are compared with experiment for NET2 as shown in Figure 4.14. For the NET2 design, the measured resistance was found to be 0.0092 psi/μL/min compared to the predicted value of 0.0089 psi/μL/min. The prediction is in excellent agreement with experiment given that the theoretical calculation neglected pressure head losses due to turns and branching, inlets and outlets, and external tubing resistances.

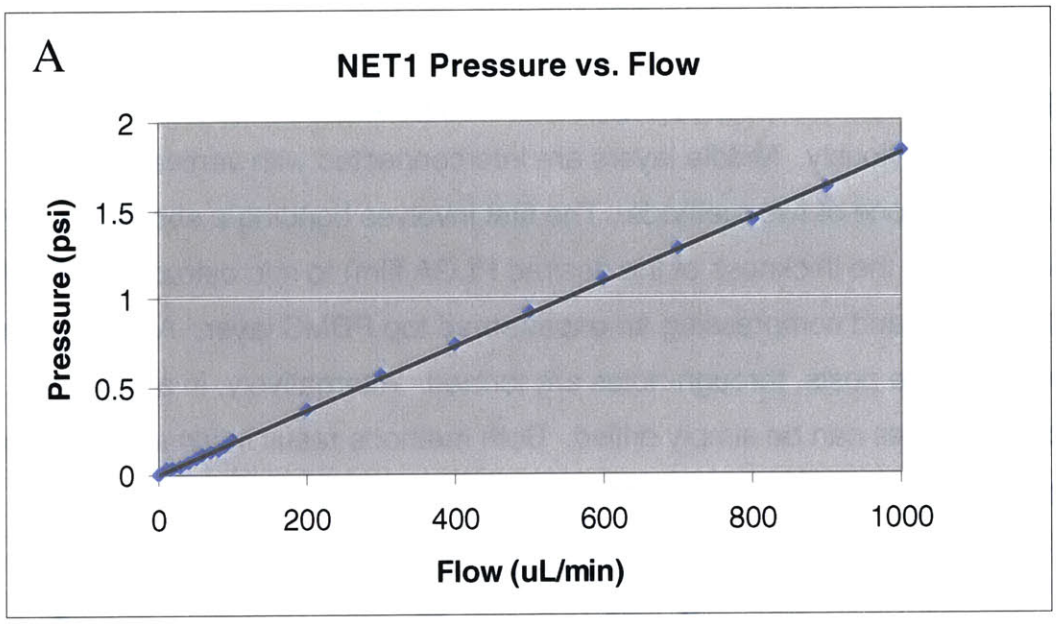

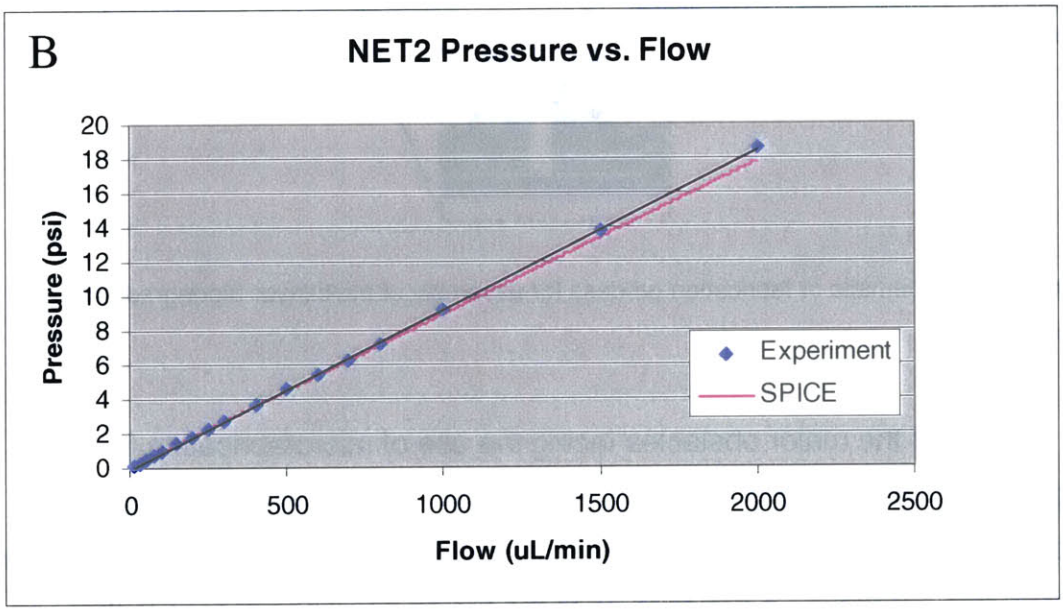

Figure 4.14 Pressure flow relationships for A) NET1 and B) NET2 with corresponding theoretical curve calculated from SPICE network analysis.

4.5 Three-dimensional Microfluidics

4.5.1 Multi-layer Fabrication Approach

Fabrication of multi-layer microfluidics is a straightforward extension of single layer networks. The top layer is fabricated with inlets and outlets as described previously. Middle layers are interconnected with vertical vias fabricated by one of two methods. The first involves bonding a shortened PDMS post (equal to the thickness of the desired PLGA film) to microstructured PDMS bottom layer, and compressing an unpatterned top PDMS layer. As the top layer presses on the posts, through-holes are formed. Alternatively, in a second approach, holes can be simply drilled. Both methods result in films that can be aligned by hand and bonded to form multi-layer interconnected networks.

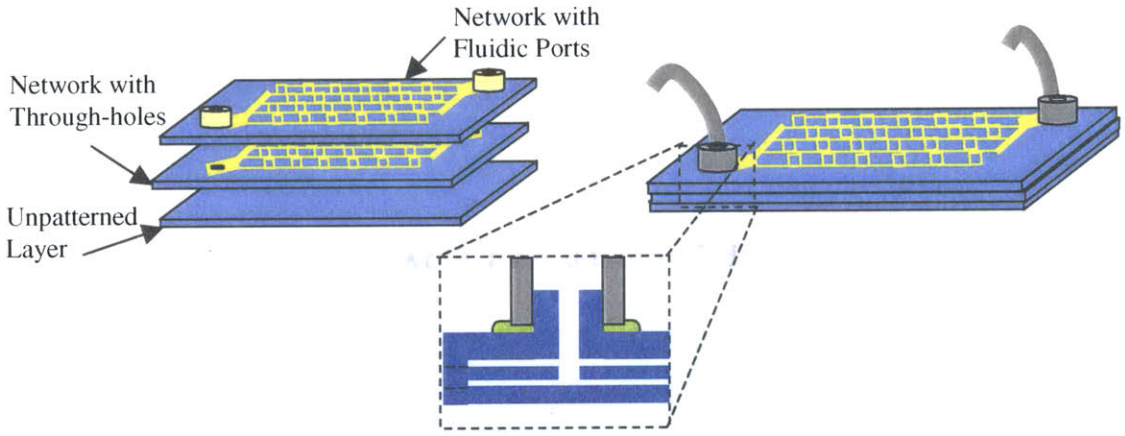

Figure 4.15 Schematic of fabrication process for assembly of multi-layer biodegradable microfluidics.

One of the major obstacles facing the use of microfabrication for tissue engineering scaffolding is three-dimensionality. The stacking and bonding approach described here allows rapid fabrication of monolithic three dimensional microfluidic networks. A key feature of the fusion bonding process is that once aligned, many layers can be bonded in a single step. Although alignment might present challenges to scaling, if ~25μm tolerance is sufficient, one can use traditional machining to design an alignment fixture or use vertical alignment posts and guide alignment mechanically.

Multi-layer Device Characterization

The device cross-section in Figure 4.16 reveals multiple stacked layers. The three-dimensional networks are easily perfused and multiple perfused layers can be viewed simultaneously using a fluorescent dye, as in Figure 4.17.

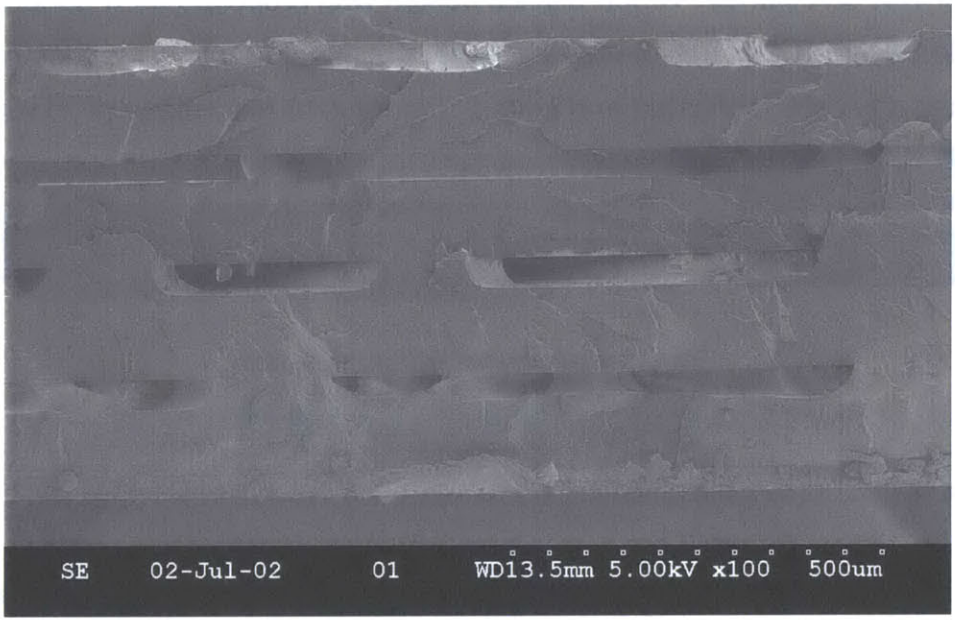

Figure 4.16 Three-dimensional microfluidic network cross-section – a monolithic interconnected network with three bonded layers, each ~180μm thick with 35μm channels, and one open-ended layer of microchannels.

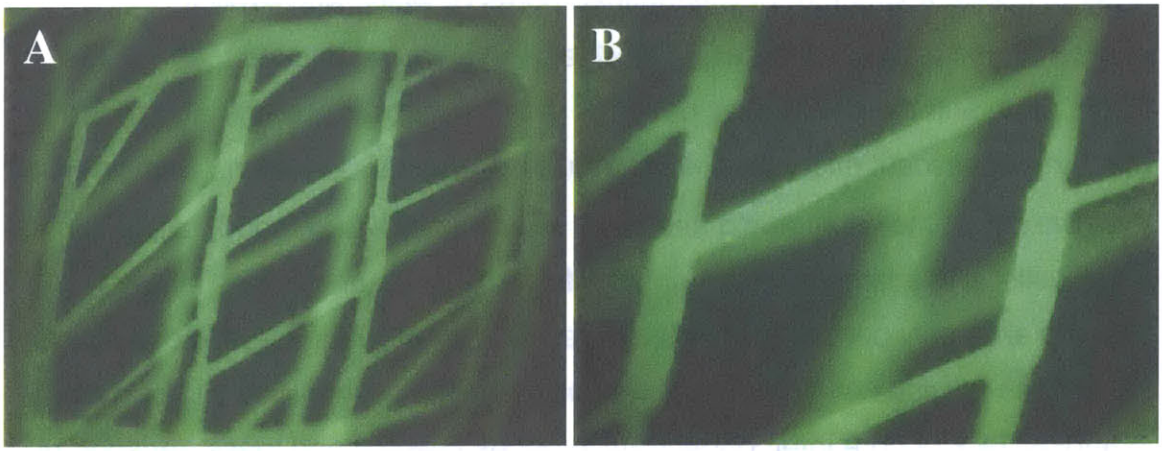

Figure 4.17 Multi-layer networks are perfused with a fluorescein solution through a single inlet and outlet as evidence of fluidic interconnection between stacked layers. A two-layer device is shown with one layer in focus and the other out of focus. Each layer is approximately 300μm thick.

4.6 Microfluidics-enabled Scaffolds

4.6.1 Fabrication Approach

The goal of this work, as described in Chapter 1, is to enable design and fabrication of complex scaffolds for large-scale tissue engineering of bulk organs such as liver and kidney. A non-explicit design was proposed for a generic bulk organ in Section 1.2 of this thesis, and here, the major functional unit of that proposed device is fabricated and tested. Figure 4.18 reiterates the concept.

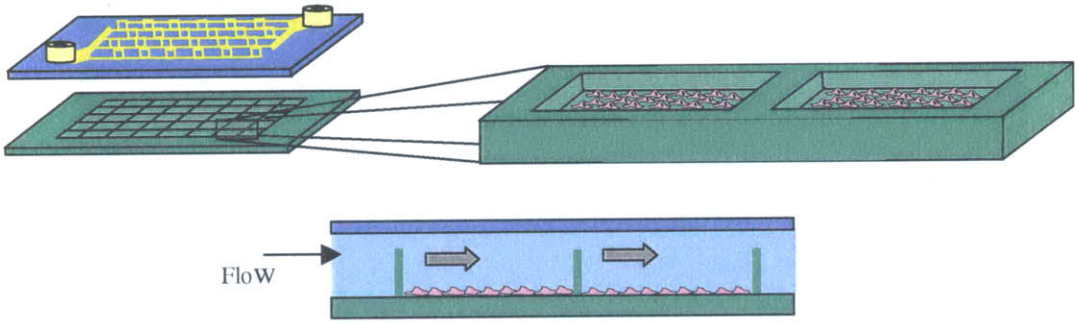

Figure 4.18 Concept for generic bulk organ assembly using microfabricated pores and microfluidic interconnections.

A silicon master mold with arrays of 800μm x 800μm x 300μm wells was fabricated using the vertical sidewall DRIE silicon etch process. This was translated into a PLGA film using the melt micromolding processes developed in Chapter 2. A top layer of NET2 microfluidics was fusion bonded to the microwell array to create a structure of well-defined pores or wells, with explicit interconnections or microfluidics. Flexible tubing was connected to the PLGA fluidic ports and the device was perfused with fluorescein dye and a suspension of 10μm fluorescent microspheres to simulate living cell perfusion. Being denser than the liquid, the microbeads sediment when the flow is stopped, falling into the microwells, and a large number remain after flow is resumed. Historically, seeding arbitrarily porous scaffolds densely and evenly has presented significant challenges to tissue engineers and typically requires several hours [3]. In many scaffolds, lack of pore interconnectivity impedes seeding and mass transport [4]. Seeding microwells with cells via microfluidic channels would offer an efficient and methodical means of rapidly (in seconds) populating rationally designed biodegradable scaffolds with an even and well-controlled distribution of cells.

4.6.2 Device Characterization

The light microscopic image of Figure 4.19 A provides a top-down view of the the microfluidic interconnections between adjacent microwells. In Figure 4.19 C, devices are perfused with fluorescein dye to demonstrate fluidic continuity between wells and channels, and they are rapidly seeded with microbeads in a simple seeding process. A microwell full of fluorescent microspheres is shown after 30 seconds of seeding in Figure 4.19 D. Microspheres are predominantly restricted to the microwells, demonstrating that heterogenous cell distributions can be designed and obtained.

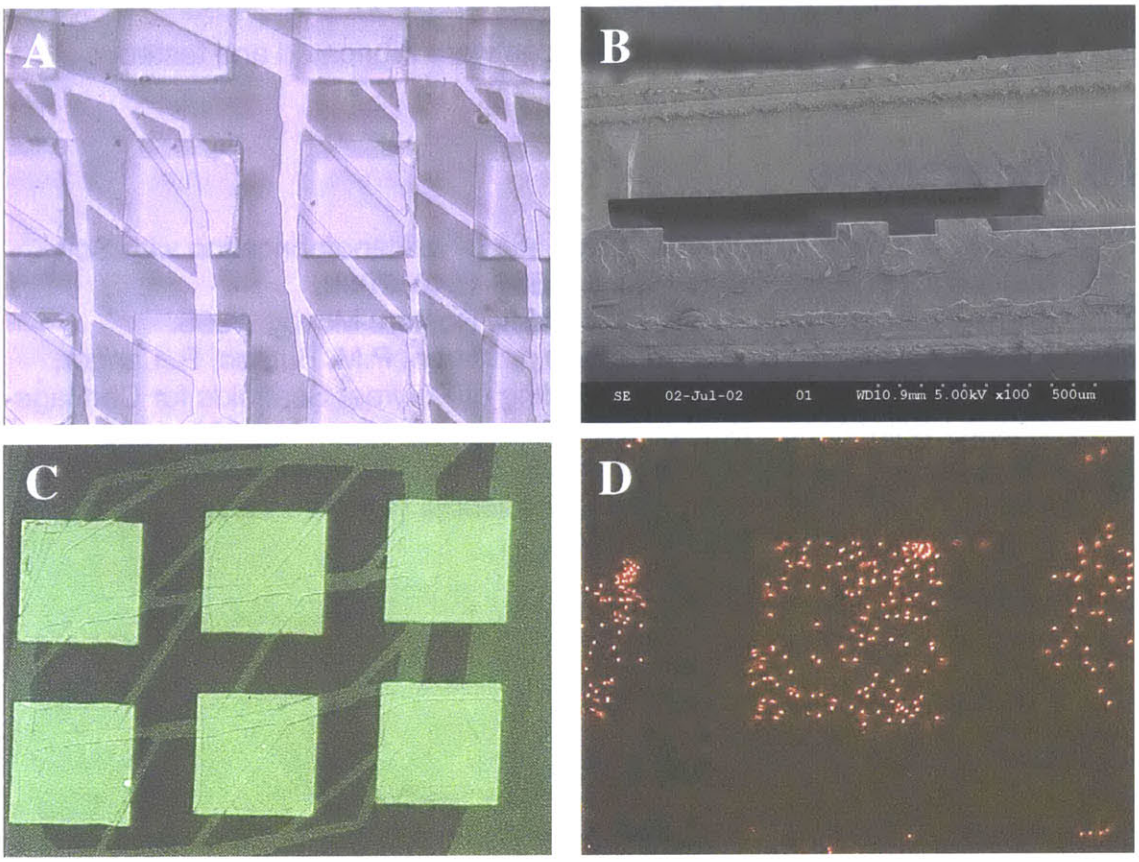

Figure 4.19 A) Light microscope image of microfluidics-enabled scaffold unit. B) SEM cross-section of device showing several microfluidic channels (bottom layer) intersecting a single well (top layer). C) Fluorescein dye perfusion demonstrating fluidic interconnection between microchannels and microwells. D) Result of seeing fluorescent microspheres for 30 seconds. Notice microspheres are localized in the wells.

4.7 Conclusion

This chapter presented methods for fabricating fully biodegradable microfluidic networks. An integrated fluidic connection scheme was implemented to realize monolithic inlets and outlets by extruding vertical ports from the microfluidic network surface, offering a robust point of contact for conventional flexible tubing. The networks were shown to be leak-free, withstanding substantial pressures, and exhibiting predictable pressure-flow relationships. Finally, the three-dimensional potential of the technology was realized as several multi-layer biodegradable microfluidic devices were fabricated and tested.

4.8 References

[1] Quake, S.R. and A. Scherer, "From Micro- to Nanofabrication with Soft Materials". Science. 290(5496): p. 1536-1540, 2000.

[2] Berne, R.M. and M.N. Levy, *Physiology*. Boston: Mosby, 1998.

[3] Vunjak-Novakovic, G., B. Obradovic, I. Martin, P.M. Bursac, R. Langer, and L.E. Freed, "Dynamic Cell Seeding of Polymer Scaffolds for Cartilage Tissue Engineering". Biotechnology Progress. 14: p. 193-202, 1998.

[4] Yang, S., K.-f. Leong, Z. Du, and C.-k. Chua, "The Design of Scaffolds for Use in Tissue Engineering. Part I. Traditional Factors". Tissue Engineering. 7(6): p. 679-689, 2001.

Chapter 5

Microfluidic Cell Culture

The biodegradable microfluidic networks described in the previous chapter are ultimately intended to support cell attachment and growth. However, to date, cell culture has not been demonstrated in such confined geometries. Cells have previously been introduced into microchannels for sorting or analysis purposes, but they are not typically cultured long term in microfluidic devices. Recently, investigators seeded insect cells in large straight microchannels and cultured them without flow or medium changes. They found the growth kinetics to be much slower in microchannels than in a petri dish during the initial days in culture, and after several days, total cell number decreased [1]. In this chapter, long-term (two weeks) microfluidic cell culture is successfully performed using continuous flow in prototype microfluidic networks to demonstrate the feasibility of seeding and culturing biodegradable microfluidics for tissue engineering applications. In contrast to previous demonstration of short-term living cell microdevices, the desire for long-term microfluidic culture requires maintenance of culture sterility and either frequent medium changes or continuous perfusion.

Cell culture in polystyrene petri dishes and flasks is routine. However, in order to successfully culture cells in the newly developed biodegradable devices, standard cell culture techniques must be adapted to the microfluidic culture space. This chapter describes techniques that allow successful sterilization, seeding, and culture of endothelial cells in microchannel geometries similar to those fabricated in Chapter 4. This feasibility study is performed in standard PDMS microfluidic networks because commonly used PLGA sterilization techniques result in loss of optical transparency shortly after seeding, making culture monitoring difficult. In this demonstration, endothelial cells were seeded in the microscale culture system and continuous-flow cultured until confluence

was achieved, demonstrating that the microscale geometries do not challenge the ability to culture. This result, combined with a long history of culturing on PLGA surfaces suggests that culture in the newly developed PLGA microfluidics is feasible, being limited neither by small geometries nor by the material.

5.1 Cell Culture

5.1.1 Cell Culture

Primary harvest endothelial cells were obtained from sheep coratid arteries provided by Dr. Pomerantseva at Massachusetts General Hospital (MGH). Briefly, endothelial cells were obtained from a freshly harvested segment of sheep carotid artery (installation) with 0.2% Collagenase type A (Boehringer-Mannheim) for 20 minutes in 37°C. Cells were cultured in gelatin-coated polystyrene culture vessels (0.1%, Sigma) using DMEM high glucose medium (GIBCO) supplemented with 10% Fetal Bovine Serum (HyClone), 1% penicillin-Streptomycin-Glutamine (GIBCO). Endothelial cells were characterized by typical cobblestone morphology and the presence of CD 31 (PECAM1) using goat polyclonal Antibody (Santa Cruz Biotechnology) and Von Willebrand Factor using rabbit antibody (DAKO).

Cells were cultured in T-75 or T-150 culture flasks in a 37°C humidified incubator with 5% CO_2. Flasks were treated with a 0.1% collagen solution for 10 minutes prior to seeding. Cells were passaged by trypsinizing, centrifuging and seeding the resuspended cell pellet every few days.

5.1.2 Imaging

Early stages of the microscale culture were visualized using a reflectance microscope at Draper Laboratory and final stages of culture were performed at MGH and were visualized under phase contrast microscopy.

5.2 PDMS Prototype Microfluidic Device

5.2.1 Design

The microfluidic network used in the microfluidic culture demonstration consists of a parallel arrangement of three NET2 designs described in Chapter 4. As before, the networks are arranged to yield equal flow in the smallest channels. The result is a network of 90 capillary beds where each capillary bed is the network of smallest channels shown at the far right of Figure 5.1.

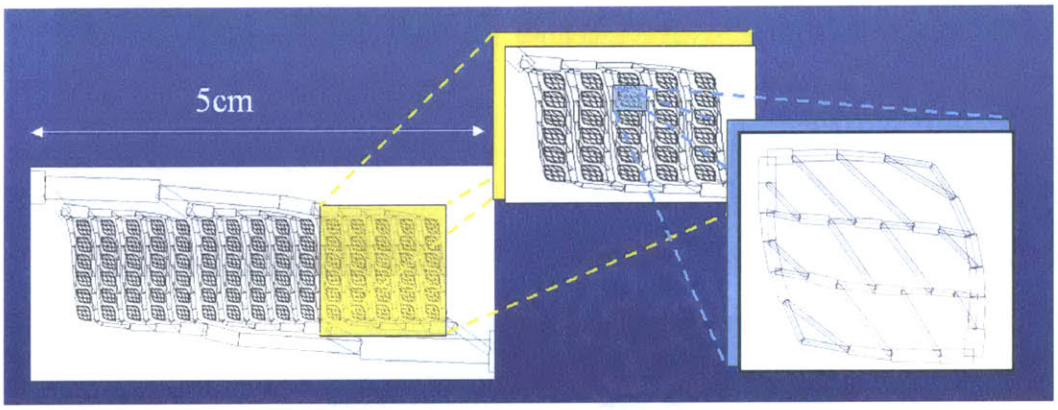

Figure 5.1 Microfluidic culture network layout.

5.2.2 Fabrication

The fabrication process is based on the soft lithography microfluidics described in Section 1.4. Briefly, SU-8 50 was photopolymerized through a mylar rapid prototyping mask to yield a 35μm thick raised channel network. PDMS prepolymer was cast, cured, and peeled, resulting flexible microchannels. However, instead of fabricating *channels* in the silicon mold (which results in raised lines in PDMS and channels in PLGA), *raised lines* were patterned in silicon and used to create recessed channels in the PDMS. Holes were drilled in the PDMS layer at the location of the inlet and outlet using a blunted and beveled 16 gauge syringe needle, and the PDMS microchannels were bonded to an unpatterned PDMS layer or a pyrex wafer after treating both surfaces with a 180 Watt / 180 mtorr oxygen plasma (Technics) for 20 seconds. The oxygen plasma increases the surface oxygen content of the surfaces, such that when the two films are brought into contact, dehydration results in the formation of siloxane

bonds across the interface. Since these silicon-oxygen bonds are similar to those found in the bulk of the elastomer, the pieces bond irreversibly with no observable interface. Plastic pipette tips are cut and used as adapters to connect the device inlet and outlet to standard tubing. This assembly is permanently bonded by applying a small amount of PDMS prepolymer at each joint, and curing for 1 hour at 70°C. The process is shown schematically in Figure 1.8 and the fabricated device is shown below in Figure 5.2.

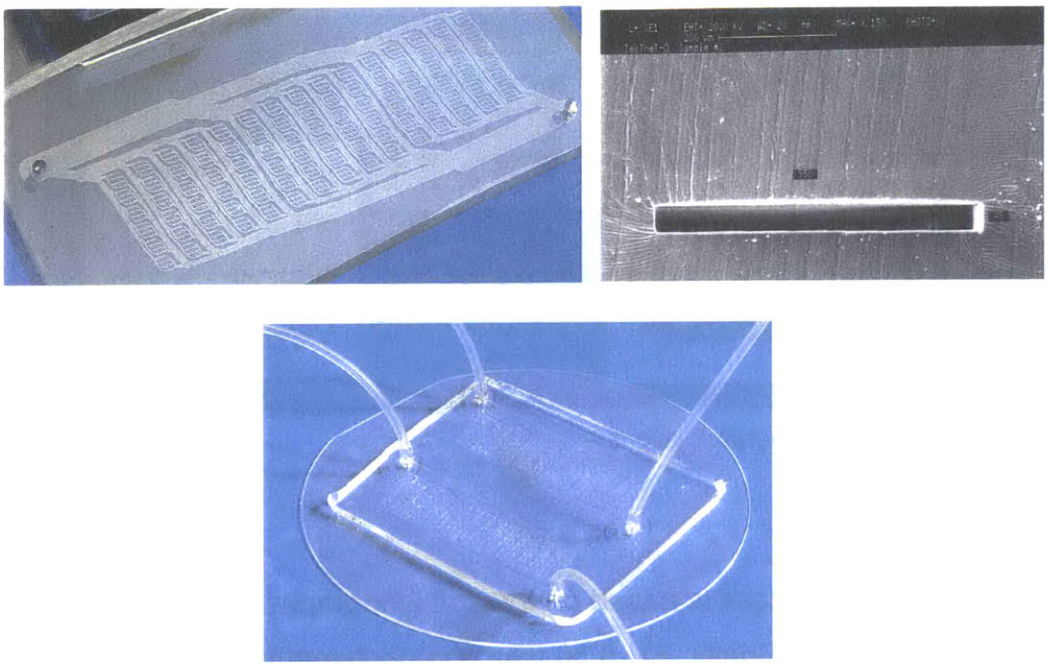

Figure 5.2 PDMS microfluidic network A) top-down, unbonded with drilled inlet and outlet, B) cross-section of PDMS microchannel of 45μm height and 550μm width, and C) completed device of 2 side-by-side PDMS networks bonded to a single pyrex wafer.

5.3 Microfluidic Bioreactor

5.3.1 Design

The surface area to volume ratio in microdevices is considerable. Therefore, surface-attached cells can rapidly deplete the associated volume of medium of oxygen and metabolites while filling it with metabolic waste. This necessitates frequent medium exchange or continuous medium perfusion to avoid hypoxia and metabolic toxicity. A bioreactor was designed to allow continuous-flow culture of cells in the microfluidic networks. The bioreactor

consists of a syringe pump, gas permeable tubing, the microfluidic network, and a waste container. Optionally, a bubble trap [2] is included just before the microdevice to capture bubbles before they enter the microfluidic device and cause damage to the culture. The bioreactor setup is shown in Figure 5.3.

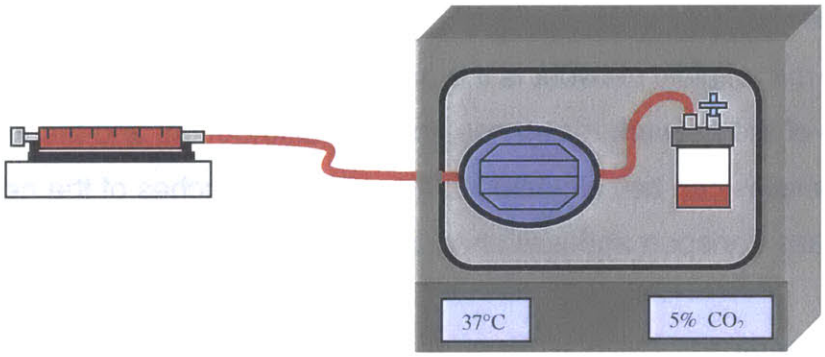

Figure 5.3 Bioreactor for continuous-flow microfluidic cell culture.

Syringe Pump

A Harvard PHD2000 displacement syringe pump (Harvard Apparatus) was used with Becton Dickson plastic syringes (10mL-60mL) and programmed to deliver the desired flow rate. Flow rates were determined by balancing the need for low shear stress and high mass transport as described in the next section.

Oxygenator

Flexible silastic tubing (1.57mm ID x 3.18 mm OD) was used to connect the various components of the bioreactor. Tubing was routed from the syringe pump, located outside the incubator, through the incubator front door, and to the device. This involves no modification of the incubator, and does not impair the maintenance of appropriate humidity or gas mixtures. For a PLGA microdevice, which is relatively impermeable to gas, the tubing also serves as an oxygenator. As medium travels through the tubing inside the incubator, it equilibrates with the temperature and ambient gas mixture inside the incubator before entering the device so that optimal culture pH and temperature are maintained. In the case of the PDMS prototype device, which is exceptionally permeable to both oxygen ($D = 4.1 \times 10^{-5}\ cm^2/s$) and carbon dioxide ($D = 2.6 \times 10^{-5}\ cm^2/s$) [1], the tubing

oxygenator is redundant. PDMS microfluidic cultures are oxygenated through the devices walls. However, the flow criterion is preserved to better simulate the biodegradable microfluidic setup.

Microdevice

The microfluidic network is the primary resistor in the fluidic circuit. Using knowledge of the network resistance, the flow distribution, and the wall shear stress, flow rates can be calculated in the various branches of the network to balance mass transport and wall shear stress.

Waste Container

The plastic screw-cap of a glass bottle was drilled and tapped to fit two barbed luer lock connectors. The first port was used to collect culture medium waste by connecting to tubing exiting the microdevice. Pressure equilibration within the waste container was achieved by attaching a sterile gas permeable filter (Millipore 0.1μm pore size) to the second connector.

5.3.2 Dynamics

Continuous Flow Culture

The bioreactor is designed to provide necessary oxygen and metabolites while efficiently removing wastes. At the same time, excess shear stress must be avoided as it can dramatically alter gene expression patterns [3, 4]. Therefore, the flow rate is constrained.

In PLGA devices, oxygen will be the limiting nutrient. Therefore, an oxygen convective mass transport criterion is used to determine a minimum flow rate. The constraints on the PDMS device are less restrictive because device walls are oxygen permeable. In such cases, mass transport is probably dominated by the removal of toxic metabolic waste. For simplicity, a lumped model is used. The microfluidic network is treated as a single conduit with one inlet and one outlet. Mass balance is performed for both fluid volume and oxygen gas.

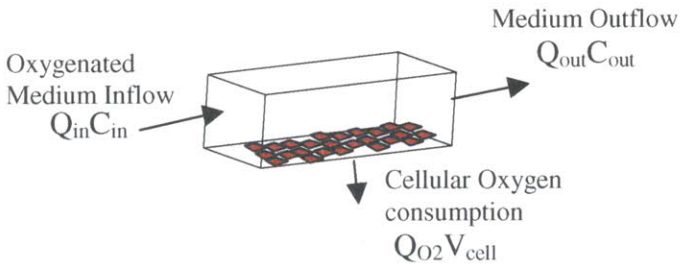

Figure 5.4 Schematic of continuous flow culture material balance.

Oxygen enters the device dissolved in the culture medium. The concentration of oxygen in 5% CO_2/humidified air-saturated culture medium at 37°C is 0.16×10^{-3} mmol/mL [5]. This is either consumed by the cells in the network or exits the device dissolved in the medium effluent. The volumetric oxygen consumption rate Q_{O2} is estimated to be $2\text{-}6 \times 10^{-5}$ mmol/(s-cm^3 of cell mass) assuming a proliferating endothelial cell to be a highly metabolic cell. V_{cell} is the volume of cell mass.

It is important to insure that the medium is not excessively depleted before exiting the device. Therefore, a minimum ratio of C_{out} to C_{in}, the outlet and inlet oxygen tensions, is set as a criterion to limit the use of low flow rates. The minimum ratio used in this study was set at a conservative 0.9 or 90%. This ratio can be written as a function of volumetric flow rate of medium Q_{fluid}.

$$\frac{C_{out}}{C_{in}} = 1 - \frac{Q_{O2}V_{cell}}{Q_{fluid}C_{in}}$$

Shear induced responses are known to effect endothelial cells at shear stresses near 30 dynes/cm^2. The wall stress is calculated at the inlet to the entire device as it is the region of highest shear. This inlet has a high width to height ratio so the shear stress is idealized as viscous flow between parallel plates to simplify the calculation. The shear stress at the cell-covered floor of this rectangular cross-section is approximately

$$\tau_{wall} \cong \frac{\mu Q_{fluid}}{h^2 w}$$

μ is the viscosity (0.7cP), h is the channel height (35μm), and w is the channel width (3mm). Selection of a maximum wall shear stress sets an upper limit on the flow rate, and this is taken to be a conservative 0.02 dynes/cm^2 in order to avoid dislodging loosely attached cells and cell aggregates during initial stages of the culture. The maximum shear stress and minimum outlet oxygen saturation can be used to determine an appropriate range of flow rates as shown in the following schematic. Using these parameter values, the medium oxygenation ratio and normalized shear stress (normalized to 0.02 dynes/cm^2) are shown as a function of flow rate in Figure 5.5. To achieve $C_{out}/C_{in} > 0.9$ and $t_{wall\_normalized} < 1$, the flow rate is maintained between 1-6μL/min.

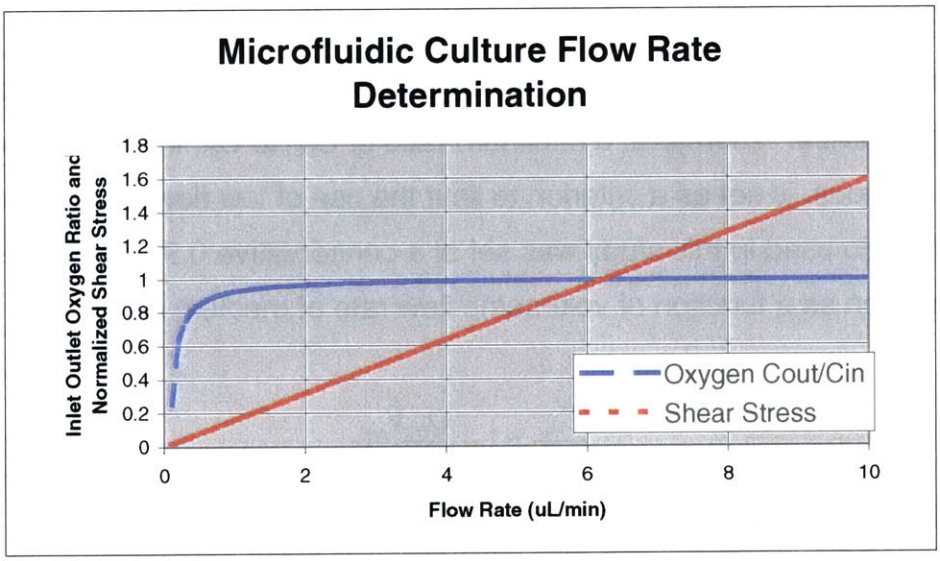

Figure 5.5 Flow rate was determined such that the medium oxygen tension did not fall more than 10% from inlet and outlet, and normalized shear stress (normalized to 0.02 dynes/cm^2) did not exceed 1.

In actuality this flow selection need not be as tightly constrained as described here. However, since this is the first demonstration of continuous flow culture in such constrained geometries it is important to make conservative estimates of both maximum shear and minimum transport. More realistically,

wall shear stress can be as large as ~1 dyne/cm^2 without causing significant alterations in cell function [6]. As mentioned before, oxygen does not limit the culture due to the large gas permeability of the PDMS device material.

5.4 Seeding

5.4.1 Sterilization and Assembly

All bioreactor components are autoclave sterilized and assembled using sterile technique (sterile surgical gloves and sterile field) in a laminar flow hood. Unlike PDMS devices, which can tolerate autoclave temperatures and pressures without microchannel distortion [7], PLGA devices cannot be treated much above the glass transition temperature of 50°C without causing reflow and microchannel collapse. Other sterilization alternatives for PLGA are ethylene oxide cold gas, ethanol, ultraviolet radiation, and gamma irradiation [8]. PLGA was found to be slightly soluble in both ethylene oxide and ethanol, turning opaque when the sterilization was followed by perfusion with aqueous medium. Ultraviolet radiation can be successfully used on unbonded surfaces, but this requires that the bonding process be performed sterile. Gamma irradiation was not attempted. So, while PLGA devices can be sterilized by several methods, it is more challenging than for PDMS, and can lead to a rapid loss in optical transparency, which impairs visualization of subsequent cultures. Therefore, PDMS, being a transparent autoclavable elastomer, provides a good prototyping vehicle.

5.4.2 Cell Seeding

Seeding cells is not considered challenging in a standard culture flask. Typically, one chooses a desired number of cells per culture surface area and delivers those cells in a volume that is sufficiently dilute that the suspension does not lead to aggregation of cells. This volume can be freely chosen and vertical depths of seeding suspensions typically approach 1cm. In a microchannel, the volume is constrained because the microchannel is completely filled, allowing no flexibility to select a seeding concentration. This can be formalized by

interpreting the channel height as a "cell seeding amplification factor". Cells are introduced as a concentrated cell suspension and all of the cells sediment due to gravity, settling on the bottom of the floor of the culture container. The number of cells per area can be calculated by dividing the cell concentration by the surface area to volume ratio. For most culture containers (microchannels, culture flasks, and petri dishes), the surface area to volume ratio is the inverse of the container height. Therefore, the number of cells per area is equivalent to the cell suspension concentration multiplied by the height or the "cell seeding amplification factor." Since flasks are typically filled with medium to a height of approximately 1 cm, and the microchannels used in this study are only 35μm, the cell suspension must be approximately 300 times more concentrated than the suspension used to seed a flask (~$1x10^7$ cells/mL). This concentration is consistent with those used by other investigators who have seeded cells using temporary microfluidic channels [7]. This presents significant challenges because in extremely concentrated suspensions, cells have more cell-cell interactions than cell-surface interactions and rapidly form cell aggregates.

Prior to seeding, the PDMS microfluidic networks were perfused with a 0.1% collagen solution. The inlet and outlet were capped steriley and the device was placed in an incubator for 30 minutes to allow the collagen to adsorb. The channel was then perfused with culture medium for 30 minutes to rinse the collagen solution and purge any bubbles. Cells were trypsinized, pelleted in a centrifuge at 1500 rpm for 5 minutes, and resuspended. The cells were filtered (40μm pore size) to remove cell aggregates, counted in a hemocytometer, and the desired concentration was prepared, typically $5x10^6$-$5x10^7$cells/mL. In this demonstration, the seeding cell concentration was determined such that the smallest channels would have order one cells per channel. The selected concentration of $5x10^6$ cells/mL cell suspension theoretically yields an average of 2.14 cells in a 35μm x 35μm x 350μm channel. The cell suspension was injected by hand using a 3mL syringe, and the syringe was immediately replaced by a long length of primed tubing and a medium-filled syringe using sterile technique. The long tubing was primed with medium so that continuous-flow culture could

be initiated without disturbing the system once the cells had sedimented and attached.

After the cell suspension was injected, devices were left without flow in an incubator for 24 hours. In microchannels, a significant number of cells remained in suspension after several hours. In standard culture flasks, several hours is sufficient to observe cell sedimentation and attachment. There are several possible explanations for the delayed sedimentation and attachment. First, microchannels, in contrast to other culture vessels are confined fluids. In order for a cell to sediment, it must displace the fluid below it, presumably by upward viscous flow around the cell. However, the small geometries and the fact that the cell is of comparable size to the microchannel suggest that the fluid is being driven through a substantial fluidic resistance. A large fluidic resistance is important because the driving force for cell sedimentation is quite small, proportional to the difference in cell and culture medium densities [9]. Another factor that might impact cell sedimentation and/or attachment is axial pressure disturbances. It was found that very small pressure disturbances at the inlet or outlet give rise to significant axial displacement of cells. For example, simply breathing warm air on the inlet tubing can cause cells to move tens to hundreds of microns in the axial direction. This effect most noticeably disturbs the attachment process by shearing cells on the microchannel floor. In summary, seeding is nontrivial, and will require further investigation and optimization.

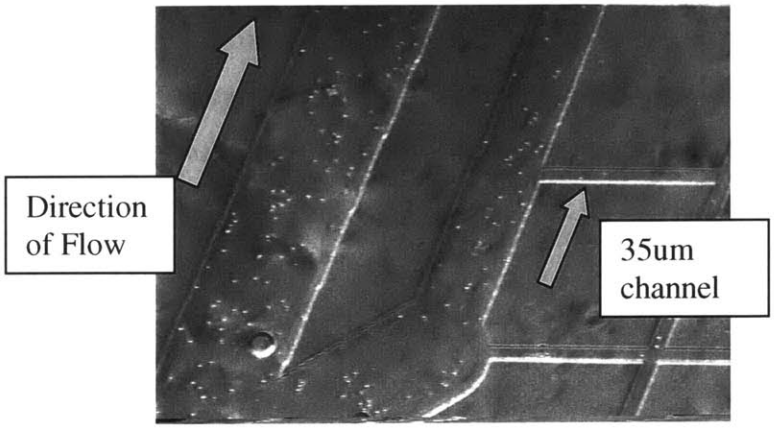

Figure 5.6 Light microscope image during seeding. Cells were seeded by hand at $5x10^6$ cells/mL from a 3mL sterile plastic syringe.

5.5 Continuous Flow Culture

5.5.1 Characterization of Culture in NET2

Early phases of culture were characterized by cell aggregates. Many individual cells were washed out as parasitic bubbles traversed the network and were removed from the system. Once stabilized, continuous flow was maintained between 1-6μL/min and the aggregates shown in Figure 5.6 A and B represented the majority of cells in the channels. Aggregates were found spaced by hundreds of microns to millimeters, and were approximately 50-100μm in diameter. At 36 hours post-seeding (12 hours after sedimentation), a crown of 5-10 individual cells, apparently migrating from the cluster, surrounded each aggregate.

At 56 hours, an increased number of cells were observed surrounding the aggregate, and most cells were beginning to exhibit a spread morphology as seen in Figure 5.6 C and D in contrast to the beaded morphology exhibited in Figures 5.6 A and B. By 90 hours, a mixture of morphologies was apparent and the total cell number and surface area covered had greatly increased, without a proportional decrease in aggregate size, suggesting that cells were proliferating.

Cells remained under continuous flow, and sterile exchange of medium-filled syringes was successfully performed several times without causing contamination or infection. After two weeks of culture, cells were found to cover 80-90% of the device area. The networks shown in Figure 5.7 are characteristic of all but a few (those not originally well seeded with aggregates) of the 90 identical branched subnetworks present on the large microfluidic culture device.

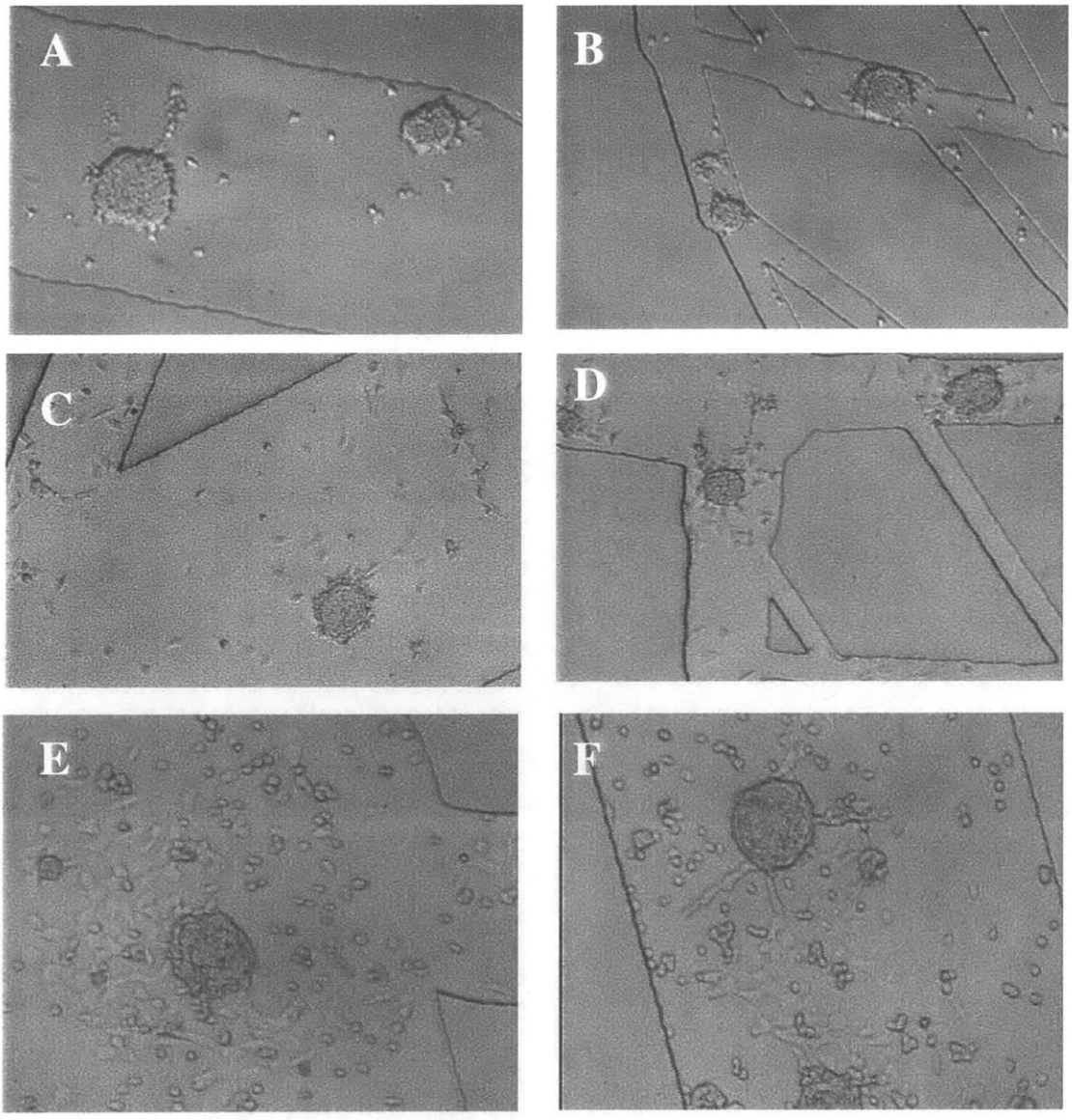

Figure 5.7 – Time course of microchannel cell growth. A) 24 hours and B) 36 hours after seeding, cells are in 40-50um diameter aggregates each with a crown of single cell. C) and D) After 56 hours, more individual cells are observed and they are spreading. E) and F) 90 hours post-seeding, cells are exhibit the characteristic cobblestone morphology.

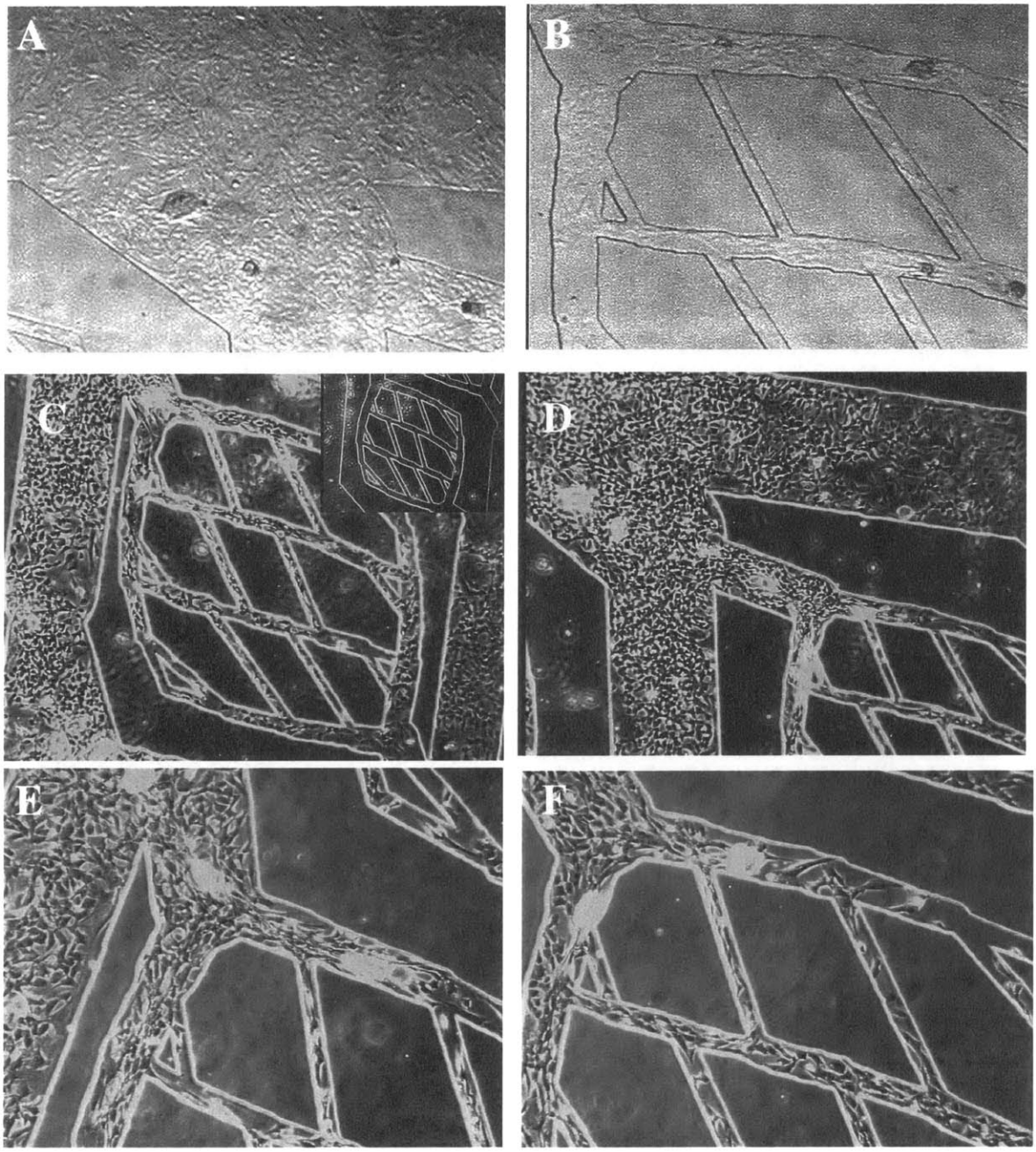

Figure 5.8 – Microchannels at two weeks. Most networks are ~80-90% confluent. The inset in C) shows a comparable network prior to seeding.

5.5.2 Characterization of Culture in NET1

A similar continuous flow culture was performed using NET1, also fabricated in a prototype PDMS material. Results were similar to NET2 cultures as shown in Figure 5.9 below.

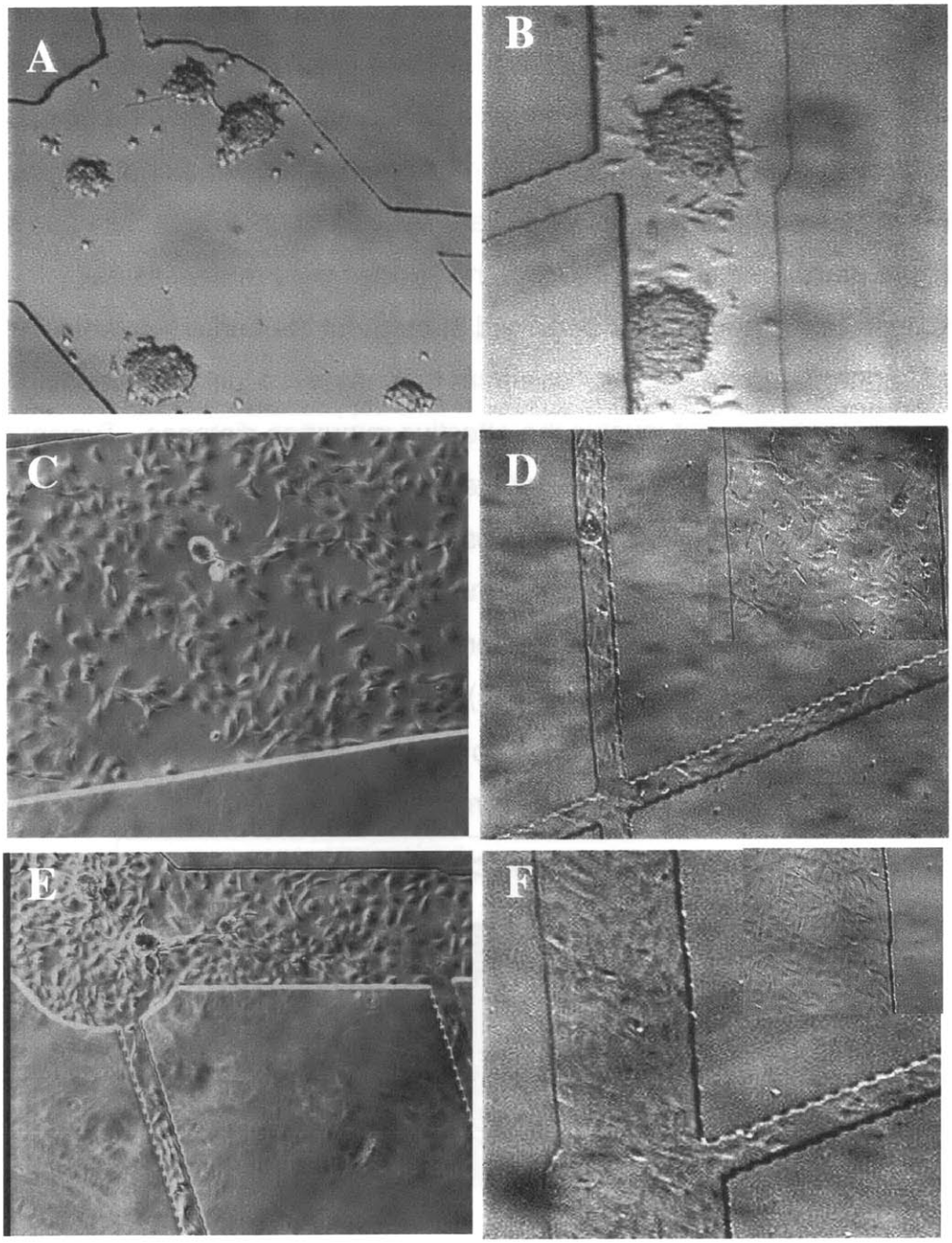

Figure 5.9 Continuous-flow microfluidic culture of sheep coratid endothelial cells in PDMS NET-1 A) 48 hours, B) 56 hours, C) 90 hours, D) 90 hours, E) 2 weeks, and F) 2 weeks. Insets show large channels on the same device.

5.5.3 Growth to Confluency

The extent of surface area coverage was approximated at several time points and is expressed as percent confluency for comparison with a conventional culture vessel. This is not meant to be a quantitative description, but rather describe the dramatic qualitative differences in the time course of culture area coverage. A key difference between macroscale and microscale cell culture is the long time required to achieve 90% confluency. Several possible explanations exist. First, microchannels might not be seeded as densely as in a typical culture flask because many cells are washed out during bubble purging and culture stabilization. Also, many of the seeded cells remain as cell aggregates. Some aggregates remained throughout the entire two-week culture, although aggregate size did decrease from that observed just after seeding. Another explanation might involve the effective migration distance. Typical flasks are seeded very evenly and well distributed, such that the distance between any two cells is small, only several cell lengths. This allows proliferation to efficiently lead to confluence. In contrast, cells in microchannels were spaced at substantial distances of several millimeters, the equivalent of hundreds of cell lengths (cell diameter taken to be ~10μm), requiring migration and considerably more proliferation to achieve complete coverage. Such a distribution might be responsible for the slower increase in percent confluency.

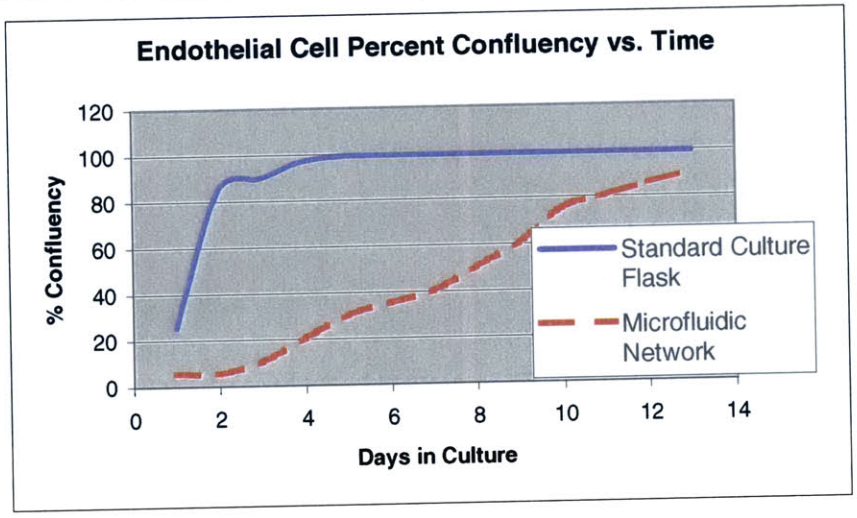

Figure 5.10 Estimation of endothelial cell percent confluency over time, comparing microfluidic networks with conventional culture flasks.

5.6 PLGA Microfluidic Culture

There are several key differences between prototype PDMS microfluidic networks and the PLGA networks developed in the previous chapter. These differences are related to 1) sterility, 2) surface energy, and 3) surface chemistry.

Sterility

Sterilization of PLGA microfluidics can successfully be performed by treating surfaces with ultraviolet light or with ethanol followed by thorough rinsing in sterile Phosphate Buffered Saline (PBS). Unbonded melt processed PLGA films were exposed to UV overnight and cultured for four days without contamination compared to unsterilized contaminated controls.

Surface Energy

Hydrophobicity is a significant obstacle for PLGA scaffolds. The hydrophobicity of the microfluidics material can have significant negative effects during continuous flow cell culture. First, it stabilizes nucleated bubbles, which occlude channels during seeding. Second, if bubbles are dislodged after cell seeding and attachment, they exert strong forces on cells, extracting them from the surfaces of all the channels they traverse. In Chapter 4, PLGA microfluidics were perfused using surfactants to lower fluid surface tension and avoid bubbles. However, cells cannot tolerate these surfactants in culture medium, as they lead to rapid cell detachment and lysis, so cultures must be performed without the additive. In order to seed cells in PLGA microfluidics without a surfactant, it was found that fluid must be perfused for approximately 24 hours before seeding. This removes most of the bubbles initially present after seeding. While there are several possible explanations, it is not yet clear why one day of perfusion appears to rid the PLGA networks of bubbles.

Surface Chemistry

The surface chemistry of the melt processed PLGA material is clearly different from that of the pyrex or PDMS surfaces exposed during prototype

cultures. However, there is a great deal of precedent for using PLGA as a cell attachment scaffold material [10], and it is reasonable to expect that it will perform comparably.

5.7 Discussion

Cells have previously been introduced into microfluidic devices for manipulation and analysis, however, they have not been cultured long term in such confined geometries. It is common to study cells under flow conditions in continuous flow bioreactors and flat plate reactors with hundred micron gaps, however cells are typically seeded prior to device assembly. Even microfluidic channels with hundred micron heights and widths that have been used to seed cells on polystyrene surfaces are removed shortly after seeding, and culture is performed in an open dish using conventional methods. Recently, insect cells were seeded in permanently bonded prefabricated microchannels and cultured, but no medium exchanges were performed so the culture was limited to seven days. In this work, fully fabricated microfluidic devices are seeded with cells and cultured under continuous flow to provide continuous medium exchange in hopes of sustaining microchannel cultures indefinitely.

Seeding a biodegradable microdevice once fully assembled and culturing the cell-polymer construct introduces many new complexities. This study demonstrates feasibility. Cells can be seeded in a fully fabricated device via microfluidic channels, they can be continuous flow cultured for weeks in order for proliferation and migration to take place, and they can achieve nearly confluent coverage of large microfluidic networks with diverse channel geometries.

In addition to the tissue engineering application with which this study was principally concerned, this demonstration also has relevance to the broader field of micro bioanalytical devices. Typical components of these "Lab on a Chip" devices involve sample preparation, assays, reactions, and detection elements. Cells have the unique ability to perform many of these functions in an efficient and elegant manner. The ability to culture cells in microfluidic devices long term

allows them to be integrated into microsystems and to be used as active components, detecting molecules via surface or intracellular receptors, amplifying the signals via efficient secondary messenger systems, undergoing corresponding changes in gene expression patterns and protein synthesis, and releasing products that can be detected by other cells or the end user, either on-chip or off-chip. While the large surface area to volume presents challenges to seeding, it is the hallmark of micro-bioanalytical systems because it requires only small amounts of expensive reagents, enables high efficiency reactions, and contains small dead volumes. Cell-seeded micro-bioanalytical devices would offer a wide range of high specificity sensors for biomolecules, and would enable concentrated solutions of secreted products to be acquired and detected without dilution. For these and many other reasons, it is important to understand how cells behave in microdevices. This work provides the first step.

5.8 Conclusion

In this chapter, long-term culture of endothelial cells was performed in continuous-flow microfluidic networks. A bioreactor was designed and appropriate operating conditions were identified to provide medium exchange and mass transfer without avoiding excessive shear stress on attached cells. The large surface area to volume ratios present in microfluidic networks presented challenges to cell seeding. However, they were overcome by populating the network with cell aggregates. These aggregates were shown to contain viable cells that migrate, proliferate, and attach to the surface, leading to nearly complete coverage of the large microfluidic network. The microfluidic cultures presented in this chapter demonstrate the potential for using the PLGA microfluidic networks developed in this thesis as cell-seeded scaffolds for use in tissue engineering applications.

5.9 References

[1] Walker, G.M., M.S. Ozers, and D.J. Beebe, "Insect Cell Culture in Microfluidic Channels". Biomedical Microdevices. 4(3): p. 161-166, 2002.

[2] King, K.R., H. Terai, C.C. Wang, J.P. Vacanti, and J.T. Borenstein. "Microfluidics for Tissue Engineering Vasculature: Endothelial Cell Culture". in *Micro Total Analysis Systems.* 2001. Monterey, CA.

[3] Malek, A.M., *Functional and molecular characterization of the vascular endothelial response to fluid shear stress*, in *HST.* MIT and Harvard: Cambridge, 1994.

[4] Nagel, T.E., *Differential regulation of genes and transcription factors in vascular endothelial cells exposed to uniform and disturbed laminar shear stress*, in *HST.* MIT and Harvard: Cambridge, 1997.

[5] Griffith, L.G., B.M. Wu, M.J. Cima, M.J. Powers, B. Chiagnaud, and J.P. Vacanti, "In Vitro Organogenesis of Liver Tissue". Annals of New York Academy of Sciences: p. 382-397, 1997.

[6] Tilles, A.W., H. Baskaran, P. Roy, M.L. Yarmush, and M. Toner, "Effects of Oxygenation and Flow on the Viability and Function of Rat Hepatocytes Cocultured in a Microchannel Flat-Plate Bioreactor". Biotechnology and Bioengineering. 73(5): p. 379-389, 2001.

[7] Chiu, D.T., N.L. Jeon, S. Huang, R. Kane, C.J. Wargo, I.S. Choi, D.E. Ingber, and G.M. Whitesides, "Patterned Deposition of Cells and Proteins onto Surfaces by Using Three-dimensional Microfluidic Systems". Proceedings of the National Academy of Sciences. 97(6): p. 2408-2413, 2000.

[8] Holy, C.E., C. Cheng, J.E. Davies, and M.S. Shoichet, "Optimizing the Sterilization of PLGA Scaffolds for Use in Tissue Engineering". Biomaterials. 22: p. 25-31, 2001.

[9] Deen, W.M., *Analysis of Transport Phenomena.* New York: Oxford University Press, 1998.

[10] Marler, J.J., J. Upton, R. Langer, and J.P. Vacanti, "Transplantation of Cells in Matrices for Tissue Engineering". Advanced Drug Delivery Reviews. 33: p. 165-182, 1998.

Chapter 6

Conclusion and Future Work

Microfabrication is an ideal tool for attacking problems in medicine and biology. Its ability to control features at the micron scale enables creation of devices that can organize and manipulate at the level of individual cells and macromolecules. While it has already made significant contributions in the areas of biochemical assays, medical diagnostics, and biological sensors, this powerful approach to biomedical investigation is just beginning to address problems in tissue engineering. Until recently, tissue engineers have focused on traditional polymer processing techniques to develop biodegradable support scaffolds for seeding and implanting cells. Unfortunately, conventional processes, and the scaffolds they produce, still suffer from poorly controlled geometries, lack of reproducibility, and severe transport limitations due to their inherent lack of vasculature. In this work, microfabrication provides both high-resolution precision geometries and reproducibility. In addition, it is used to fabricate microfluidic channels on the same size scale as biological capillaries, and might enable creative solutions to problems of achieving rapid vascularization and recapitulation of normal tissue architecture.

6.1 Summary of Contributions

The work described in this thesis makes several novel contributions in the general areas of biodegradable polymer microfabrication, fusion bonding modeling, and microfluidics cell culture.

Biodegradable Polymer Microfabrication

Two key processes, 1) melt micromolding of biodegradable polymer onto flexible microfabricated master molds and 2) thermal fusion bonding of microstructured thermoplastics were developed to form three-dimensional monolithic precision structures, including complex branching microchannel networks. In comparison to other biodegradable processing approaches that require days of drying and can only achieve spatial resolution of hundreds of microns, melt micromolding proves to be a rapid, reproducible, and high-resolution method for microstructuring biodegradable films. Microfabrication is however, commonly criticized for being fundamentally limited to two-dimensional devices. Therefore, fusion bonding was developed and found to be a straightforward approach to achieve three-dimensionality, preserving microstructures and offering a robust process window by avoiding temperature-induced plastic deformation. The power of these key processes was demonstrated by building fully biodegradable monolithic microfluidic networks. An inlet and outlet scheme consisting of extruded biodegradable ports that connect to standard flexible tubing was implemented and the devices were demonstrated to withstand physiologic pressures, and have predictable and therefore designable pressure-flow relationships.

Fusion Bonding Modeling

A model was developed to predict the time course of thermoplastic thermal fusion bonding as well as temperature-induced plastic deformation of microchannels, the dominant mode of failure. This model was used to define a conservative process window in terms of device geometry, process parameters, and material-specific creep response, which then successfully guided the bonding of a wide range of challenging structures including channels with width-to-height ratios as large as 200. At a time when plastic microfluidic devices are being developed for diverse biomedical applications, it is critical to have predictive models for process development. This conservative model successfully balances the need for model precision with the desire for simplicity and intuition to guide device design and process development.

Microchannel Cell Culture

Cells have been introduced into microdevices for manipulation and analysis, but they are not typically cultured long term. In this work, a critical demonstration of long-term continuous-flow microfluidic cell culture was performed. By seeding cells and culturing them to confluence across large footprint microdevices, this study establishes the feasibility of culturing cells for long periods in sterile microfabricated devices. In addition, the demonstration establishes the feasibility of the biodegradable microfabricated scaffold concept, and offers a new tool/technique to the area of bioanalytical microdevices. It also opens the door to a wide range of rich microfluidics-enabled experiments in which basic properties and dynamics of cells can be probed and even harnessed to act as living transducers, sensing the local microenvironment and giving rise to specific detectable outputs in response.

6.2 Future Work

Near-term Improvements

Solvent casting and melt processing each have distinct advantages. Melt processing has unmatched reproducibility, precision, and processing speed, while solvent casting offers flexibile thin films and the potential to produce reliable microfabrication of through-holes. Although the flexibility is due to residual solvent, it is possible that some level of solvent might be tolerable. Ultimately, it might be desirable to combine the approaches sequentially with initial solvent casting followed by subsequent melt processing to retain the speed and precision of melt processing while achieving very thin films, thus presenting the opportunity to tune microfabricated film thickness and flexibility. While this has been performed successfully over small areas ~1cm^2 in this work (data not shown), it remains challenging over larger areas.

Bubbles present a significant challenge to all microfluidics applications. The inherent size of the conduits elevates surface tension and capillarity to the status of a dominant force, making devices exquisitely sensitive to the surface

energy of the device material. In many cases, the material surface can be modified physically or chemically to improve wetting, but in this work additional complications are present. In addition to its hydrophobicity, the PLGA material has a very low temperature ceiling and the transparent nature of the film is very sensitive to even slight dissolution by solvents such as ethanol (commonly used to improve PLGA wetting). Bubbles often need to be removed after cell seeding, which excludes the use of non-sterile approaches for bubble removal. At this point, bubbles represent the most significant obstacle to PLGA microfluidic cell culture, and therefore, this issue requires further investigation.

Degradation is of critical importance in evaluating the long-term utility of PLGA microfabricated devices and scaffolds. While continuous flow through microfluidics might facilitate removal of acidic degradation products, thereby slowing the auto-catalytic degradation of PLGA, it is possible that polymer swelling during the early "water uptake" phases of degradation might cause premature occlusion of very small channels before hydrolytic degradation can proceed. In this work, such channel collapse was not observed despite several days of flow and culture. However, loss of transparency and slight distortion of channel walls was observed after one week of perfusion. This is another area that will also require further investigation.

Future Outlook

Because the biodegradable microfabrication techniques developed in this thesis are quite general, one can imagine using them in a wide range of applications in the general areas of drug delivery, and tissue engineering. However, since this work was specifically developed for tissue engineering applications, some speculation on future directions in this field are offered.

In comparison to conventional scaffolds, this technology offers the ability to systematically uncover the relationships between scaffold geometry, tissue development, and dynamic interactions with the host. This technology does not merely make incremental improvements in resolution and processing time, but offers the opportunity to introduce new functionality to tissue engineering

scaffolds. The vasculature-like microfluidic networks developed in this thesis are just one example.

The ability to preseed scaffolds with chemical-releasing elements such as degradable drug-encapsulated microspheres might allow one to deliver molecular cues and guide tissue development in a spatially controllable fashion. Alternatively, because of the low fusion bonding temperature, it might be possible to incorporate liquid drug into scaffold compartments. Because the bonding process involves no chemicals, surface treatments, or adhesive layers, specific chemical or physical surface modification might be used to guide complex arrangements of multiple cell types throughout the scaffold in hopes of recapitulating normal tissue microarchitecture and preserving differentiated function. Determining what role the scaffold should play in the development of complex bulk organs will require many careful experiments. This technology with its control and reproducibility is poised to see that such investigation is performed rationally and systematically. For example, the porosity, surface area, void volume, and pore interconnectedness can be designed precisely, prior to fabrication. In addition, these properties need not be homogeneously distributed across microfabricated scaffolds as they are in traditional scaffolds, but instead can be precisely varied locally, to encourage vascularization in certain regions and parenchymal development in others.

Conventional salt leached and phase inversion scaffolds have already been thermally fusion bonded to the microfabricated films presented in this thesis without any modification of the processes. Using this approach, biodegradable microfabrication might represent a more general platform for integrating and harnessing the many successes that tissue engineering has already achieved. Through the versatile fusion bonding process, one can conceive of complex devices that integrate the "best practices" of scaffold fabrication in hopes of building therapeutically viable solutions for patients suffering from loss of tissue and loss of function.

Delivering a therapeutic number of cells is the primary reason for developing large tissue engineering scaffolds. Unfortunately, existing scaffold

technologies scale poorly, either due to their fabrication process or their inability to provide mass transport throughout a large scaffold. Because of the large fusion bonding process windows, the methods developed in this thesis can readily achieve large constructs of several centimeters without compromising micron resolution or precision. In addition, microfluidic interconnections insure that they can be evenly and densely seeded as well as continuous-flow cultured *in vitro* until implantation. Since the size of the scaffold is not limited by cell seeding or oxygen and metabolite transport, these laminates provide an opportunity to deliver substantially larger quantities of cells than those achieved in commonly used porous scaffolds. Not only can the number of cells be dramatically increased, but the arrangements of multiple cell types can conceivably be controlled using these techniques, providing a unique opportunity to recapitulate normal tissue microarchitecture, encourage rapid vascularization, and ultimately restore organ-specific function.

It is interesting to consider how many 40μm hepatocytes can be theoretically delivered in a 1cm thick construct. If it is assumed that the construct is $5x5x5cm^3$, that each layer consists of arrays of 800um square wells (pores) separated by 50um walls, and that the floor of each square pore houses a confluent layer of hepatocytes (assumed to be 40um squares), there would be $>10^6$ cells/layer. If 125 layers (each 400um thick – to a total thickness of 5 cm) were stacked, that would allow implantation of $>10^8$ cells, a large number of cells. Because a single compression molded layer can be patterned on both sides, the microfluidic networks that provides convective mass transport can be molded into one side and the pores on the other so that the 400μm film thickness could include both pores and fluidics. If these cells proliferate and fill the bulk of each pore (6 doublings would $>10^{10}$ cells, and 10 doublings would give $>10^{11}$ cells), it might be possible to deliver a truly therapeutically viable number of cells.

6.3 Final Thoughts

Despite early successes engineering skin and other thin layers of tissue, major challenges prevent the straightforward extension of cell-seeded biodegradable scaffolds to larger and more complex tissues such as liver and kidney. Rapid vascularization, cellular organization, and well-differentiated function are critical if bulk organs are to be successfully engineered. It is likely that the support scaffold will play a significant role in this process. However, existing scaffold fabrication techniques lack the precision and design flexibility to fashion vasculature and organize cells at the level of tissue microarchitecture. This thesis describes an enabling technology for fabricating high precision biodegradable scaffolds to address these concerns and build high performance tissue engineering scaffolds.

Microfabrication is not new to tissue engineering, but until now it has only been effectively employed to create *two-dimensional in vitro* models of tissue. In this thesis, microfabrication is used to process implantable biodegradable polymers for *three-dimensional in vivo* applications. The platform offers two orders of magnitude improvement over existing techniques in fabrication time (minutes vs. days) and resolution (~1μm vs. ~100μm), while providing exceptional design flexibility, and unmatched precision and reproducibility. The approach requires no specialized equipment once a reusable microfabricated mold is fabricated, and therefore enables any laboratory to perform routine fabrication of high-resolution three-dimensional biodegradable microdevices and explore the promising potential of this new technology.

[This page intentionally left blank]

Appendix A

MASTER MOLD MICROFABRICATION

This appendix describes the four silicon microfabrication processes used to create the master mold for subsequent biodegradable polymer molding 1) additive thin Novolak photoresist, 2) additive thick SU-8 photosensitive epoxy, 3) deep reactive ion etching of bulk silicon, and 4) isotropic etching of bulk silicon. In each case, the process begins with cleaning of 4 inch, 500μm thick, single side polish silicon wafers in 3:1 H_2SO_4:H_2O_2. This removes organics from the bare silicon surface.

Novolak Photoresist

The thin additive photoresist process begins with dehydration of the clean silicon wafer in an oven at 200°C for 30 minutes. The wafer is then coated with Hexymethyldisilozane (HMDS) at 4000 rpm for 30 seconds to facilitate adhesion of the photoresist. AZ1822 positive photoresist is spin coated at 4000rpm for 30 seconds and soft baked at 92°C for 30 minutes to yield a film thickness of 2.2μm. It is exposed through the appropriate photomask using a Karl Suss MA-6 mask aligner at a lamp intensity of 20.5mW/cm^2 for 8 seconds (total energy of 164mJ/cm^2). The exposed film is then developed in MF319 developer for 30 seconds. Finally, to harden the film for subsequent PDMS casting, the photoresist features are baked at 110°C for 30 minutes. This final bake leads to smoothing of otherwise vertical sidewalls and results in a more rounded cross-section than without the hardbake step. It can also cause minor variations in critical dimensions. This can be seen in the high resolution molded PLGA in Figure 2.14.

High Aspect Ratio SU-8 Photoresist

The thick additive photosensitive epoxy SU-8 25 acts as a negative photoresist because it is polymerized where it is exposed. After cleaning the silicon, SU-8 is poured on the surface and spin coated in two steps, first at 500 rpm for 5 seconds to wet and cover the entire wafer, and then at 2500rpm for 10 seconds to achieve a nominal thickness of 35μm. The film is soft-baked by ramping to 95°C on a planarized hotplate, holding for 3 hours, and then ramping back to room temperature. In addition to promoting solvent evaporation and gelling of the epoxy, this temperature is above the glass transition of the photoresist and allows the resist to reflow and heal defects in the thick film. After softbake, the SU-8 is exposed through the appropriate photomask by a 20.5mW/cm^2 UV Hg arc lamp in a Karl Suss MA-6 aligner for 60 seconds to promote free-radical polymerization. The wafer is post-exposure baked on a hotplate by ramping from room temperature to 95°C, holding for 1 hour, and then returning to room temperature. Finally, the unexposed resist is dissolved in Propylene Glycol Methyl Ether Acetate (PGMEA) solvent until the unexposed regions are completely removed and the pattern is completely defined, as confirmed by microscopic inspection. Once developed, the wafer is cleaned using a standard three-step rinse – acetone, isopropyl alcohol, and deionized water, and is ready for use as a mold for casting PDMS prepolymer.

Deep Reactive Ion Etching (DRIE)

Subtractive bulk silicon etches are masked by one or two layers of photoresist depending on the depth of the etch. Cleaned wafers are dehydrated in an oven at 200°C for 30 minutes and spin coated with HMDS at 4000rpm for 30 seconds. Then, AZ4620 positive photoresist is spin coated at 6000 rpm for 30 seconds, baked at 92°C for 1 hour, cooled for 5 minutes, and repeated to achieve two layers with a total thickness of 5.6μm. The resist is exposed in a MA-6 mask aligner for 13.5 seconds, developed in MF999 for 30 seconds, and the resist residue is removed in an oxygen plasma at 80 W, 200 mtorr for 3 seconds. The silicon is then etched in the STS Inductively Coupled Plasma

(ICP) etcher using a BOSCH process, alternating between side-wall protecting fluoropolymer deposition and plasma bulk silicon etching. This process results in a rectangular cross-section with vertical side walls and is capable of defining high aspect ratio structures. Once the etch is complete, the photoresist etchmask is stripped in acetone and plasma cleaned in a low power oxygen plasma. Finally, the wafer is returned to the STS ICP Machine for a 12 second polymer passivation step to aid release of cured PDMS elastomers.

Mesa Silicon Etching

Mesa etching of silicon is performed using a similar process to the DRIE process described above. However, the etch is performed using an STS RIE Machine resulting in either an mesa or "D-shaped" cross-section profiles. Similar to the DRIE process, the etch is followed by photoresist stripping and fluoropolymer passivation to aid release of cured PDMS elastomers.

These generic processes allow for fabrication of a wide range of silicon cross-sections that can be transferred to biodegradable thermoplastics with high fidelity as described in Chapter 2.

[This page intentionally left blank]

Appendix B

PLGA Material Details

PLGA 85:15 DL High IV (Inherent Viscosity) polymer pellets were purchased from Alkeremes (http://www.alkermes.com - product name Medisorb). The polymer is stored in an amber bottle in a refrigerator to avoid degradation prior to processing. PLGA 85:15 copolymer is amorphous with a glass transition temperature of 50-55°C. The recommended process temperature is 140-160°C.

Inherent Viscosity = 0.66 – 0.80 (dL/g)
Degradation = 5 - 6 months

Soluble in ethyl acetate, methylene chloride, chloroform, acetone, dimethyl formamide (DMF), tetrahydrofuran (THF), and Hexafluoro Isopropanol (HFIP). Not soluble in water, ethanol, methanol, silicon oil, ethyl ether and petroleum ether (heptane, hexane, etc.)

GENERAL MECHANICAL PROPERTIES

Polymers	5050 DL	100 DL	100 L (Custom)	9010 L/DL (Custom)
Formulation	50% poly d,l-lactide / 50% glycolide	100% poly d,l-lactide	100% poly l-lactide	90% poly-l-lactide / 10% d,l-lactide
Break stress, psi	8296	6108	7323	7614
% strain at break	5.2	5.0	5.5	5.2
Yield stress, psi	8371	6666	7678	8414
% strain at yield	5.1	3.7	4.9	4.5
Modulus, psi	189,340	207,617	182,762	210,680

Table B.1 PLGA general mechanical properties provided by Alkeremes.

[This page intentionally left blank]

Appendix C

MICROFLUIDIC RESISTANCE PREDICTIONS

The motion of an incompressible fluid in a microchannel is governed by the Navier-Stokes equation:

$$\rho \frac{D\vec{V}}{Dt} = -\nabla P + \mu \nabla^2 \vec{V} \tag{C.1}$$

where the substantial derivative is defined as

$$\frac{D\vec{V}}{Dt} = \frac{\partial \vec{V}}{\partial t} + \left(\vec{V} \bullet \nabla\right)\vec{V} \tag{C.2}$$

and where P is the pressure, ρ is the fluid density, μ is the dynamic viscosity, and V is the velocity. The Reynolds number, a dimensionless number representing the relative importance of inertial and viscous forces is defined as

$$\mathrm{Re} = \frac{\rho U L}{\mu} \tag{C.3}$$

where U is the characteristic velocity and L is the characteristic length. In microchannels, the Reynolds number is typically less than one, allowing the inertial term to be neglected.

$$\nabla P = \mu \nabla^2 \vec{V} \tag{C.4}$$

This viscous-dominated flow is referred to as "Low Reynold's Number Flow".

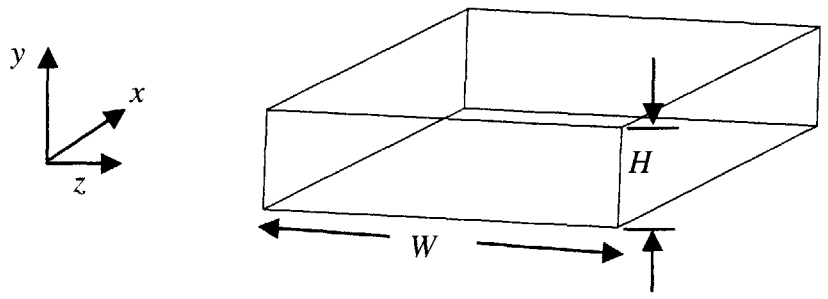

Figure C.1 Schematic of rectangular channel.

This viscous dominated flow through a rectangular channel can be solved in terms of an infinite series using the method of Finite Fourier Transforms or an equivalent method. The analytical solution for the axial velocity profile in a rectangular duct is given below, where c = H/2 and b = W/2.

$$u_x(y,z) = -\frac{1}{2\mu}\frac{\partial P}{\partial x}c^2\left[1-\left(\frac{z}{c}\right)^2+4\sum_{k=1}^{\infty}\frac{(-1)^k}{\alpha_k^3}\frac{\cosh\left(\frac{\alpha_k y}{c}\right)}{\cosh\left(\frac{\alpha_k b}{c}\right)}\cos\left(\frac{\alpha_k z}{c}\right)\right]$$

$$\alpha_k = (2k-1)\frac{\pi}{2}, k = 1,2,... \qquad \text{(C.5)}$$

This equation can be manipulated to give an expression for the fluidic resistance (ratio of pressure and volumetric flow), of a finite length rectangular duct.

$$R = -\frac{3\mu}{4}\frac{L}{bc^3}\left[1-\frac{6c}{b}\sum_{k=1}^{\infty}\frac{\tanh\left(\frac{\alpha_k b}{c}\right)}{\alpha_k^5}\right]^{-1} \qquad \text{(C.6)}$$

The hydraulic resistance, a property of the fluid and the channel geometry, relates pressure and flow just as an electronic resistor relates voltage and current. This formalism allows pressures and flows in complex fluidic networks to be calculated by resistor networks using linear circuit analysis. A circuit simulation tool (SPICE) is used to predict the total network resistance. A subnet of NET2 with labeled resistances is shown below as an example. The predicted resistance for NET2 is 0.0092 psi/μL/min as compared to the experimentally determined 0.0089 psi/μL/min.

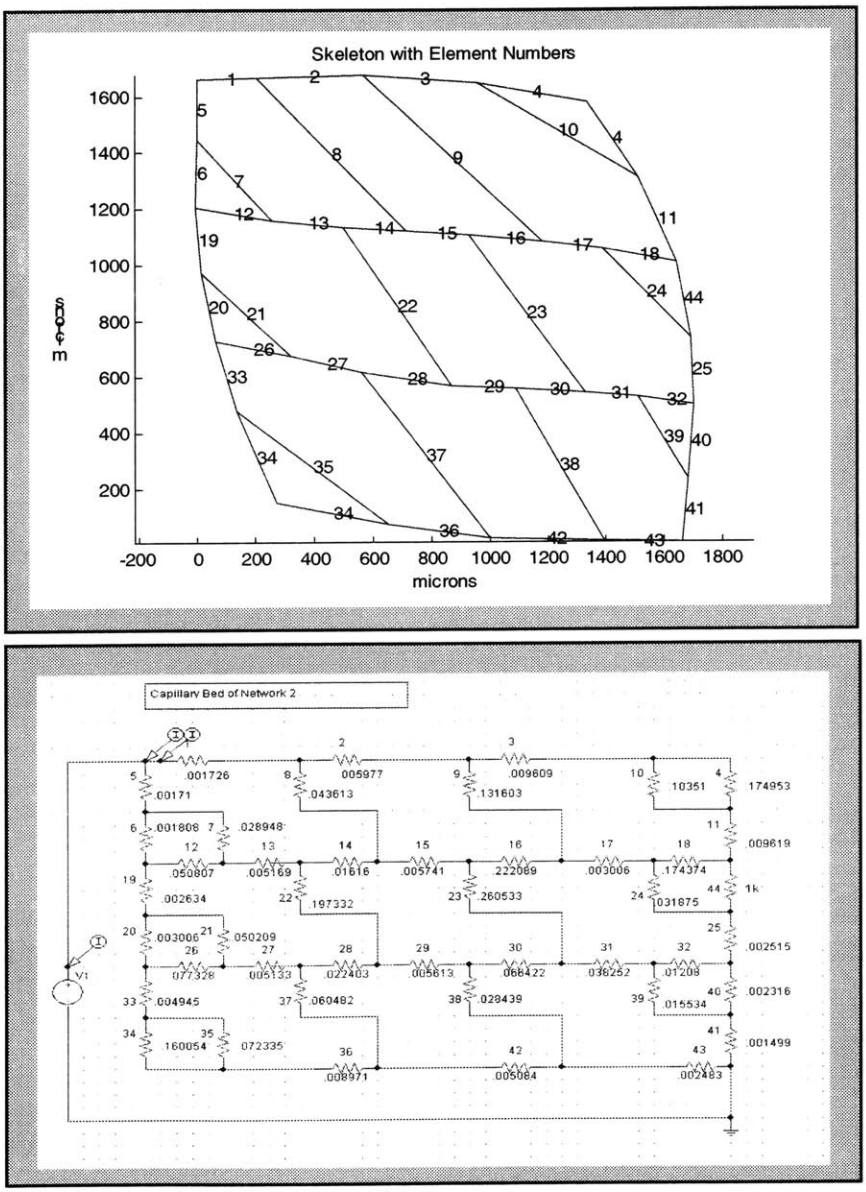

Figure C.2 SPICE Network analysis for prediction of total network hydraulic resistance.